



University of Nairobi

School of Engineering

**"A Study on the Effects of Iron on Microstructure and
Mechanical Properties of Aluminum-Silicon alloys"**

By

KOECH KIBET PIUS

F56/7339/2004

(B.Sc. Mechanical Engineering, University of Nairobi)

A Thesis Submitted in Partial Fulfillment of the Requirements for the

Degree of Master of Science in

Mechanical and Manufacturing Engineering.

University of Nairobi.

November 2012.

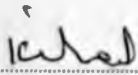
University of NAIROBI Library



0385664 8

Declaration

This thesis is my original work, except where acknowledgements and references are made to previous work, and has not been presented for a degree in any other university.

Signature:  Date: 21/11/2012

Pius Kibet Koech

(B.Sc. Mechanical Engineering, University of Nairobi)

Approval

This thesis has been submitted for examination with our approval as university supervisors.

1. Signature:  Date: 21st NOV 2012

Dr. Kamau Gachigi

(Department of Mechanical and Manufacturing Engineering, University of Nairobi)

2. Signature:  Date: 21-11-2012

Prof. George Rading

(Department of Mechanical and Manufacturing Engineering, University of Nairobi)

Dedication

I dedicate this work to my supervisors for their unending support and to my lovely daughter Presley Chemutai.

During the study, iron in the form of iron filings was added into the molten aluminum in a granular crucible to achieve the levels of iron content namely; 0.1wt%, 1.1wt%, 1.9wt%, 2.9wt% Fe and 3.9wt% Fe. Strontium modification and magnesium addition was done for some alloys in order to study their microstructural changes. The melt treatment, such as de-gassing, skimming, filtering and casting was carried out prior to casting the specimens into a preheated casting mold.

After the complete solidification, cooling rates were recorded for various samples using K-type thermocouples. Some cast specimens were heat treated before carrying out mechanical tests and metallographic analysis. Metallographic analysis was carried out using a metallograph and samples prepared to hardness testing cruciate and the micro-structure characterized before. Mechanical analysis was conducted using tensile, fatigue and hardness testing machines at the University of Nairobi in the department of mechanical and manufacturing engineering workshop.

Cooling rate analysis indicated that altering the chemical composition slightly influences the solidification behavior and type of phases formed. Change in iron and manganese was found to cause a variation in the reaction temperature while strontium addition tends to lower the solidification temperature.

From the microstructural analysis, it was observed that intermetallic compounds are formed at high iron contents as well as high concentrations of manganese. Both grain size and volume fraction of intermetallic compounds were found to increase from 0.1 μm to 2.3 μm and from 0.07% to 0.09%

Abstract

The objective of this study was to investigate the effects of iron content on the microstructure and mechanical properties of scrap locomotive engine aluminium pistons. Cast aluminum alloys mainly A356 and 319 find widespread applications in general engineering for automotive, aerospace and in domestic applications due to their high quality and lightness combined with excellent castability.

During this study, iron in the form of iron filings was added into the molten aluminum in a graphite crucible to achieve four levels of iron content namely; - 0.84wt.% Fe, 1.2wt.% Fe, 1.5wt.% Fe and 1.8wt.% Fe. Strontium modification and manganese addition was done for some alloys so as to study their neutralizing effects on β - phases. The melt treatment, such as degassing, skimming, fluxing and refining was carried out prior to casting the specimens into a permanent cast-iron mold.

Prior to complete solidification, cooling rates were recorded for thermal analysis using K-type thermocouples. Some cast specimens were heat-treated before carrying out mechanical tests and metallographic analysis. Microstructural analysis was carried out using a microscope and camera connected to hardness testing machine and the microstructure characterizer software. Mechanical analyses were conducted using tensile, fatigue and hardness testing machines at the University of Nairobi in the department of mechanical and manufacturing engineering workshop.

Cooling rate analysis indicated that altering the chemical composition strongly influences the solidification behavior and types of phases formed. Change in iron and manganese was found to cause a variation in the reaction temperature while strontium addition tends to lower the nucleation temperature.

From the microstructural analysis, it was observed that intermetallic compounds are formed at high iron contents or at high concentrations of manganese. Both grain size and volume fraction of intermetallic compounds were found to increase from 5.3 μm to 7.3 μm and from 4.2% to 8.6%

respectively as the iron content increases from 0.84wt.% Fe to 1.8wt.% Fe. With addition of 0.6wt.% Mn to an alloy of 1.2wt.% Fe, grain size was found to increase further from 6.3 μm to 7.1 μm , while volume fraction increased from 4.9% to 5.8%. The formation of intermetallic phases mainly β - phase with iron addition were found to adversely reduce tensile strength from 207 MNm^{-2} with 0.84wt.% of iron to 168 MNm^{-2} when iron content increased to 1.8wt.%. Increase on iron content was also found to reduce ductility but increases hardness from 85 HVN with 0.84wt.% Fe to 97 HVN with 1.8wt.% of iron. Both percentage elongation and area reduction were found to drop from 2.5% and 3.6% with 0.84wt.% Fe to 1.5% and 2.2% respectively when iron content was increased to 1.8wt.% Fe. It was also found that increasing iron content from 0.84wt.% to 1.8wt.% decreases fatigue life from about 1.745×10^6 cycles to about 1.404×10^6 cycles at an applied constant load of 2894 newtons.

The above detrimental effects on microstructure and mechanical properties were as a result of increased β -phases with increase in iron content. Addition of manganese, strontium modification and heat-treatment was found to reduce such harmful effects of β -phases by converting and defragmenting the brittle and needle like beta phases to less harmful Chinese script α -phases. Such improvement of mechanical properties with strontium modification and heat-treatment is also as a result of coarsening and spheroidization of silicon particles.

Acknowledgements

I am deeply indebted to my supervisor Dr. K. Gachigi and also to Prof. G. Rading for giving me an opportunity to work with them on this project. I am so grateful for your enormous help, your guidance, and your patience.

I would also like to thank Dr. T. O. Mbuya and Eng. B. O. Odera for introducing me to this area of materials science and giving me the topic of my research. You taught me and gave me everything I needed to know.

The author also wishes to thank all those involved in one way or the other in carrying out this research work. To Eng. David Mwadali and Eng. K. Chirchir of Kenya Railways Corporation who provided aluminium pistons for this study, Mr. Njue and Mr. Rono for their assistance in casting process and also Mr. Macharia who assisted in tensile testing.

The many contributors should also be thanked for taking time to assist me in testing among other needed processes. First is Mr. Githome whose tireless effort and assistance allowed me to machine all specimens required for mechanical testing and microstructural analysis. Also to my colleague Mr. A. Niva for his assistance in data collection and processing, not forgetting Eng. Aduol, Mr. Kahiro and Mr. Ndulu of the Department of Mechanical and Manufacturing Engineering Workshops.

A heartfelt thank you is also extended to Mr. Antipas Tirop of Kenya Pipeline Cooperation, Sophie Chero of Royal media and Ms Nancy Chepkorir of Kenya Airways who assisted in typing and printing part of this report.

I also thank my brother Simon, my sisters Veronica of USA, Phanila of Germany and my entire family. You have always been there to support me spiritually and financially. I thank you for everything and I love you all.

Lastly I extend my thanks to AMSEN for permitting me to use their equipments and other support including training and workshops.

Pius Koech.

Table of Contents

Declaration	i
Approval.....	i
Dedication	ii
Abstract.....	iii
Acknowledgements.....	v
Table of Contents.....	vi
List of Tables.....	ix
List of Figures.....	x
Nomenclature	xii
Chapter 1: Introduction	1
1.1 Overview of Aluminium-Silicon alloys	2
1.2 Statement of Research Problem	3
1.3 Objectives	4
1.3.1 Broad Objective	4
1.3.2 Specific Objectives	4
Chapter 2: Literature Review	5
2.1 Introduction.....	6
2.2 Typical Microstructure of Aluminum-Silicon alloys.....	6
2.3 Effects of Iron on Microstructure of Al-Silicon alloys	8
2.4 Effect of Iron on Mechanical Properties of Al-Silicon alloys	10
2.4.1 Tensile Properties	10
2.4.2 Hardness Properties	12
2.4.3 Fatigue Properties	12
2.4.4 Creep Properties.....	13
2.5 Effects of Iron on Chemical and Physical Properties.....	13
2.6 Effects of Iron on Castability of Aluminium-Silicon alloys	14
2.6.1 Sludge Formation Tendency.....	14
2.6.2 Die-Soldering Tendency	16
2.6.3 Hot Tearing.....	19
2.6.4 Fluidity	19
2.6.5 Porosity Formation	21
2.7 Control of Iron Intermetallic Compounds in Al-Si Castings.....	24
2.7.1 Effects of Solution Heat Treatment	24
2.7.2 Cooling Rate Effects	26
2.7.3 Effect of Melt Treatment.....	27

2.7.4	Iron Correcting Elements	28
2.7.5	Electromagnetic Filtration	30
2.7.6	Gravity Sedimentation	31
Chapter 3: Experimental Methods.....		32
3.1	Introduction.....	33
3.2	Design of Experiment.....	33
3.3	Experimental Procedures.....	34
3.3.1	Chemical Analysis	34
3.3.2	Mold Design	34
3.3.3	Melt Preparation and Casting	35
3.3.4	Pouring and Measurement of Cooling Rates.....	37
3.3.5	Heat Treatment	38
3.3.6	Mechanical Testing.....	39
3.3.6.1	Tensile test	39
3.3.6.2	Fatigue test	41
3.3.6.3	Hardness test	44
3.3.7	Metallographic Examination	45
Chapter 4: Experimental Results		48
4.1	Introduction.....	49
4.2	Cooling Curves	49
4.3	Microstructures	51
4.3.1	Effect of Iron addition on Microstructure	52
4.3.2	Effect of Manganese addition on Microstructure	53
4.3.3	Effect of Strontium addition on Microstructure	54
4.3.4	Effect of Sr and Mn Combined additions on Microstructure.....	56
4.3.5	Effect of Heat-Treatment on Microstructure.....	56
4.3.5.1	Effect of Iron addition and Heat Treatment on Microstructure .	57
4.3.5.2	Effect of Mn additions and Heat-Treat on Microstructure	58
4.3.5.3	Effect of Sr addition and Heat Treatment on Microstructure	58
4.3.6	Summary of Microstructural Results.....	60
4.3.7	ASTM Grain Size Number and Volume Fraction Measurement ...	61
4.4	Hardness Test.....	64
4.4.1	Effect of Iron addition on Hardness.....	64
4.4.2	The Effects of Fe, Mn, Sr and Heat Treatment on Hardness	65
4.5	Tensile Test.....	66
4.5.1	Tensile Strength	66
4.5.1.1	Effect of Iron additions on Tensile Strength.....	66

4.5.1.2	Effect of Manganese additions on Tensile Strength.....	67
4.5.1.3	Effect of Strontium Modification on Tensile Strength.....	67
4.5.1.4	Effects of Strontium and Mn Combined on Tensile Strength....	68
4.5.1.5	Effects of Heat-treatment, Sr and Mn on Tensile Strength.....	69
4.5.2	Ductility.....	70
4.5.2.1	Effect of Iron addition on Ductility	70
4.5.2.2	Effects of Manganese and Strontium Modification on Ductility	71
4.5.2.3	Effect of Heat-treatment on Ductility	72
4.6	Fatigue Results.....	73
4.6.1	Effect of Iron addition on Fatigue	74
4.6.2	Effects of Mn and Sr addition on Fatigue	76
4.6.3	Effect of Strontium and Manganese Combined on Fatigue	77
4.6.4	Effect of Heat-treatment and Strontium Modification on Fatigue .	78
4.6.5	Fatigue Crack Growth Rate.....	80
Chapter 5: Discussion of Results		83
5.1	Introduction.....	84
5.2	Thermal Analysis.....	85
5.2.1	Precipitation of α - Al Dendrite Network	85
5.2.2	Precipitation of Intermetallics	86
5.2.3	Precipitation of Al-Si Eutectic.....	87
5.3	Microstructural Characteristics.....	88
5.3.1	Effects of Iron addition on Microstructure.....	89
5.3.2	Effects of Manganese addition on Microstructure.....	90
5.3.3	Effects of Strontium Modification on Microstructure	91
5.3.4	Effects of Strontium and Mn Combined on Microstructure	93
5.3.5	Effects of Heat-Treatment on Microstructure	95
5.4	Mechanical Properties.....	97
5.4.1	Hardness Test	98
5.4.2	Tensile Properties	99
5.4.3	Fatigue Results Analysis.....	102
Chapter 6: Conclusions and Recommendations		105
6.1	Conclusions.....	106
6.2	Recommendations.....	108
References		109
Appendices		116
Appendix A:	Cooling Rates Analysis.....	117
Appendix B:	Hardness Testing	120
Appendix C:	Tensile Testing	121
Appendix D:	Fatigue Testing.....	127

List of Tables

Table 3.1: Chemical composition of the alloys used in this study.....	34
Table 3.2: Final percentage of iron, Mn and strontium after casting	35
Table 4.1: Precipitation temperatures of various phases for alloys	50
Table 4.2: Cooling rates of four alloys; P3, P4, P6 and P9.....	50
Table 4.3: Average ASTM Grain size of particles.....	62
Table 4.4: Volume fraction of intermetallics per unit volume	62
Table 4.5: Values of crack growth exponent and coefficient for alloys P0 to P3...	75
Table 4.6: Values of FCG rates, m, and corresponding fatigue cycle	81
Table A1: Results of time - temperature data for four alloys	118
Table B1: Vickers Hardness Number (HVN) for all cast samples	120
Table C1: Results of tensile tests.....	121
Table C2: Percentage elongation for specimens	125
Table C3: Percentage area-reduction for varying samples	126
Table C4: Ultimate Tensile Stress for varying samples	126
Table D1: Number of cycles versus crack length.....	127
Table D2: Crack growth rate, da/dN versus stress intensity factor range, ΔK ..	131

List of Figures

Figure 2.1: Microstructure of Al-12.5wt.% Si alloy; (a) Slowly cooled 200 \times , (b) Chill cast ²⁸	8
Figure 2.2: Microstructure of (a) modified Si seen as fibers, (b) Al-8.5Si-2.5Cu-0.4Fe -0.3Mg alloy ²⁴	9
Figure 2.3: Solubility of hydrogen in pure aluminium, 356 and 319 alloys ¹⁶	22
Figure 2.4: (a) Cast Al-Si-Mg alloy in T6 condition; arrows show porosity, (b) Cast Al-Si-Mg alloy in HIPed T6 condition; no evidence of Porosity ¹⁹	23
Figure 2.5: Microstructures of alloys cast into a graphite mold, showing the effect of (a) 0.3wt.%Mn alone and (b) 0.3wt.%Mn combined with 0.015wt.%Sr... 29	29
Figure 3.1: Permanent cast-iron mold used for casting.....	35
Figure 3.2: Electric Furnace used to melt the alloys under study	36
Figure 3.3: Heat Treatment Furnace	38
Figure 3.4: Specimens for Tensile test (dimensions in mm).....	40
Figure 3.5: Hounsfield Tensiometer type W	40
Figure 3.6: Tensile test specimens after testing	40
Figure 3.7: Schematic and dimensions of a Compact Tension (CT) specimen.....	41
Figure 3.8: Dimensions of a CT specimen used for fatigue test in mm	42
Figure 3.9: Fatigue Crack Growth test rig.....	43
Figure 3.10: Travelling Optical microscope.....	44
Figure 3.11: Vickers Hardness Testing using the LV 800AT machine.....	45
Figure 3.12: Metallographic preparation and examination using a microscope and camera connected to Leco LV800AT Hardness testing machine	47
Figure 4.1: Cooling curves for four alloys P3, P4, P6 and P9.....	49
Figure 4.2: Microstructure of alloys P0 (0.84wt.% Fe), P1 (1.2wt.% Fe), P2 (1.5wt.% Fe) and P3 containing 1.8wt.% Fe. Magnifications 200 \times and 500 \times	53
Figure 4.3: Microstructure of alloys P4 (1.2wt.% Fe, 0.6wt.% Mn) and P5 containing 1.8wt.% Fe, 0.9wt.% Mn under magnifications of 200 \times and 500 \times	54
Figure 4.4: Microstructure of alloys P6 (1.5wt.% Fe), P7 (1.8wt.% Fe) and P8 (0.84wt.% Fe) modified with 0.02wt.% Sr. 200 \times and 500 \times	54
Figure 4.5: Microstructure of alloy P9 containing 0.84wt.% Fe with addition of 0.6wt.% Mn and modified with 0.02wt.% Sr. 200 \times and 500 \times	56
Figure 4.6: Microstructure of alloys T0 and T1 with additions of 1.2wt.% Fe and 1.8wt.% Fe respectively. Magnifications of 200 \times and 500 \times	57
Figure 4.7: Microstructure of alloy H2 containing 1.2wt.% Fe with addition of 0.6wt.% Mn. Magnifications \times 200 and \times 500.....	58
Figure 4.8: Microstructure of alloys H3, H4 and H5 with 1.5wt.% Fe, 1.8wt.% Fe and 0.84wt.% Fe respectively modified with 0.02wt.% Sr. 200 \times and 500 \times	59
Figure 4.9: Distribution of ASTM Grain size number for alloys P0 and P1	61
Figure 4.10: Distribution of ASTM Grain size number for alloys P2 and P3	61
Figure 4.11: Distribution of ASTM Grain size number for alloys P4 and P5.....	62
Figure 4.12: Grain size as a function of iron concentration and Mn addition.....	63
Figure 4.13: Volume fraction of intermetallics as a function of iron concentration	63

Figure 4.14: The effect of iron addition on the hardness of Al-Si alloys	64
Figure 4.15: Effects of alloying elements and heat treat on hardness of Al-Si alloys .	65
Figure 4.16: The effect of various iron content on the UTS of Al-Si alloys.....	66
Figure 4.17: The effect of Mn and Fe addition on the UTS of Al-Si alloys	67
Figure 4.18: The effect of strontium modification on the UTS of Al-Si alloys.....	67
Figure 4.19: The effect of Sr and Mn combined on the UTS of Al-Si alloys.	68
Figure 4.20: Effects of heat-treatment and modification on Tensile strength	69
Figure 4.21: Effect of iron addition on ductility; (a) elongation, (b) area reduction....	70
Figure 4.22: Effects of Fe, Mn addition and Sr modification on ductility	71
Figure 4.23: Effect of Heat-treatment, Mn and Sr modification on ductility.....	72
Figure 4.24: da/aN versus ΔK curves for alloy P0, (0.84wt.% Fe).....	73
Figure 4.25: da/aN versus ΔK curves for alloy P1, (1.2wt.% Fe).....	73
Figure 4.26: da/aN versus ΔK curves for alloy P2	74
Figure 4.27: da/aN versus ΔK curves for alloy P3	74
Figure 4.28: da/aN versus ΔK curves for alloys P0, P1, P2 & P3 superimposed.....	75
Figure 4.29: da/aN versus ΔK curves for iron and manganese added alloy P4.....	76
Figure 4.30: da/aN versus ΔK curves for Strontium modified alloy P6.....	76
Figure 4.31: da/aN versus ΔK curves for Sr and Mn combined alloy P9	77
Figure 4.32: da/dN versus ΔK curves for alloys P4, P6 and P9 superimposed.....	77
Figure 4.33: da/aN versus ΔK curves for heat-treated alloy H0	78
Figure 4.34: da/aN versus ΔK curves for heat-treated alloy H5	78
Figure 4.35: da/aN versus ΔK curves for heat-treated alloys H0 and H5	79
Figure 4.36: Fatigue crack growth of nine alloys with varying elements	80
Figure 4.37: Fatigue Crack Path for FCG Test	82
Figure 5.1. Phase Diagram of binary Al-Si alloy	89
Figure 5.2: Microstructural comparison of alloy with 0.84wt.%Fe exhibiting (a) unmodified and (b) strontium modified morphologies	92
Figure 5.3: Microstructure of unmodified alloy P3 showing branched structure.....	93
Figure 5.4: Microstructure of (a) Mn added alloy compared to that of (b) Mn and Sr combined.....	94
Figure 5.5: Solidification routes in the Al-Si-Fe-Mn equilibrium phase diagram ³¹	95
Figure 5.6: Microstructures of unmodified alloys containing 1.2wt.%Fe, (a) as-cast condition and (b) after solution heat-treatment T6 condition.....	96
Figure 5.7: Microstructures of Sr modified alloys containing 1.5wt.% Fe: (a) as-cast condition and (b) after solution heat-treatment T6 condition.....	97
Figure 5.8: Graph of fatigue crack growth exponent, m, (MPa \sqrt{m}).....	102
Figure 5.9: Micrograph of an etched surface showing the intergranular fatigue crack growth crack path for FCG test conducted on heat-treated material.....	104
Figure A1: Locomotive engine (aluminium) pistons used in this research.....	119

Nomenclature

Constants

C	Fatigue crack growth coefficient
m	Fatigue crack growth exponent
R	Load ratio, $\frac{\sigma_{\min}}{\sigma_{\max}} = \frac{P_{\min}}{P_{\max}}$

Greek symbols

α	Alpha phase
β	Beta phase
ΔK	Stress intensity factor range
$\Delta P / F$	Load, Force range
$\sigma_{\min}, \sigma_{\max}$	Minimum and maximum applied stress
σ_{UTS}	Ultimate Tensile Stress
μm	Micro meter

Abbreviations

a_n	Crack length
ASTM	American Society of Testing and Materials
BCC	Body centred cubic crystallographic structure
BS	British Standard
CT..	Compact Tension
$^{\circ}\text{C}$	Degrees Celsius
DAS	Dendritic arm spacing
$\frac{da}{dN}$	Change in crack length per change in number of cycles
D_o, D_f	Initial and final gauge diameter
e	Base of natural logarithm
FCG	Fatigue crack growth
L_o, L_f	Initial and final gauge length
N	Number of cycles
Nm^{-2}	Newton's per unit area
RPM (rpm)	Revolutions per minute
VHN	Vickers Hardness number
wt.%	Weight percentage

INTRODUCTION

1.1. Synthesis of Aluminum Nitride Films

Aluminum nitride (AlN) films are synthesized via various methods such as metal-organic chemical vapor deposition (MOCVD), plasma-enhanced atomic layer deposition (PEALD), and sputtering. The synthesis of AlN films is a complex process involving the reaction of aluminum and nitrogen precursors.

CHAPTER 1: INTRODUCTION

The synthesis of AlN films is a complex process involving the reaction of aluminum and nitrogen precursors. The synthesis of AlN films is a complex process involving the reaction of aluminum and nitrogen precursors. The synthesis of AlN films is a complex process involving the reaction of aluminum and nitrogen precursors.

Aluminum nitride (AlN) films are synthesized via various methods such as metal-organic chemical vapor deposition (MOCVD), plasma-enhanced atomic layer deposition (PEALD), and sputtering. The synthesis of AlN films is a complex process involving the reaction of aluminum and nitrogen precursors.

The synthesis of AlN films is a complex process involving the reaction of aluminum and nitrogen precursors. The synthesis of AlN films is a complex process involving the reaction of aluminum and nitrogen precursors. The synthesis of AlN films is a complex process involving the reaction of aluminum and nitrogen precursors.

The synthesis of AlN films is a complex process involving the reaction of aluminum and nitrogen precursors. The synthesis of AlN films is a complex process involving the reaction of aluminum and nitrogen precursors. The synthesis of AlN films is a complex process involving the reaction of aluminum and nitrogen precursors.

INTRODUCTION

1.1 Overview of Aluminium Silicon alloys

Aluminium and aluminium alloys are characterized not only by lightness but also by a high thermal and electrical conductivity, strength, impact toughness, non-toxicity and ease of fabrication.^{1,2} Aluminium alloys are produced in a variety of grades:- commercially pure ingots (99.5wt.% to 99.99wt.% Al) which are soft and ductile come from electrolytic cell reduction of Al_2O_3 , while secondary metal ingots are prepared by melting recycled aluminium alloy products. Most of the impurities found in the primary metal come from the raw materials such as bauxite, carbon, etc.³

Aluminium and its alloys form the second most widely used group of cast metals worldwide after ferrous cast metals.⁴ With a wide range of casting alloys, various countries have developed their own alloy nomenclature and designation. The aluminium Association (AA) in the United States has adopted a four digit numerical system to identify aluminium casting alloys.^{5,6}

Wrought and cast aluminium alloys find widespread applications, such as in aerospace, automotive, building, chemical and process industries and in domestic appliances.^{7,8} Aluminium alloy castings are increasingly dominating the automotive industry at the expense of iron castings. They are widely used in cars for engine blocks, cylinder heads, pistons, rocker covers, inlet manifolds, differential castings, steering boxes, brackets, wheels, etc.^{9,10} Cast 319 and A356 alloys are two commercially popular alloys employed. The drive to energy conservation has led to widespread use of casting aluminium alloys, because of their excellent strength to weight ratio, which leads to an increase fuel efficiency. These alloys possess excellent tensile and fatigue properties with good corrosion resistance.^{11,12}

The strength of pure aluminium is improved by cold work or alloying. A wide range of elements such as Si, Cu, Zn, Mg, Mn, Fe, Sn, Cr, Ni and Ti, can be added to aluminium in small quantities to improve its strength, resistance to stress corrosion and other mechanical properties.

Silicon with copper imparts good castability and resistance to hot tearing. Magnesium, typically less than 0.75wt.%, may impair fluidity and feeding, but gives high strength with good ductility, excellent corrosion resistance and weldability.¹³ Manganese is used to control iron-rich intermetallics in the alloy, leading to improved ductility and shrinkage characteristics. Nickel imparts the high strength and hardness, zinc improves heat treatment and natural aging characteristics while titanium and boron refine the grain structure of the alloy.¹⁴ Others are lead which improves machinability, phosphorus that refines the primary silicon phase in hyper-eutectic alloys, strontium, sodium and antimony which modify the Al-Si eutectic structure and lithium is added to increase creep resistance.⁵¹

1.2 Statement of Research Problem

Iron is highly soluble in molten aluminium and is usually present in the range of between 0.03% and 1.0%.^{17,18} It is added unintentionally through use of steel tools or added intentionally to increase the high temperature strength and reduce die soldering. When the amount of alloying elements exceeds the solid solubility limit, second phase constituents form during solidification. Iron combines with other elements like manganese and chromium to form iron-rich (sludge) phases which reduce ductility and machinability.^{19,20} Thus, the deleterious effects of iron outweigh its benefits and efforts should be made to keep its levels as low as is economically possible. Two iron phases that are important in Al-Si hypoeutectic foundry alloys are, β - Al_5FeSi phase and α - $\text{Al}_{15}\text{Fe}_3\text{Si}_2$. The α - phase often appears as Chinese script while the β - phase appears as needles or platelets, and has been associated with coarsening of the grain size, porosity formation and a decrease in the secondary dendrite arm spacing in a 319 alloy, especially at low cooling rates.^{21,22} Other phases formed are δ - Al_4FeSi_2 phase with platelet morphology in high silicon alloys, γ - Al_3FeSi phase forms in high iron and silicon alloys while π - $\text{Al}_8\text{FeMg}_3\text{Si}_6$ phase forms in high Mg alloys among others.^{23,24,25}

In this work, an effort has been made to further our understanding of the effect of iron on cast aluminium alloys with the aim of expanding the scope of available knowledge and apply our understanding to alleviate the problems of iron presence in aluminium castings. The study focused on the effect of iron on thermal analysis behaviour, the microstructure, tensile properties, hardness and fatigue properties of silicon based cast aluminium alloys.

1.3 Objectives

1.3.1 Broad Objective

The primary objectives of this study was to experimentally determine the effects that iron has on the microstructure and mechanical properties of aluminium-silicon alloys used in locomotive engine pistons.

1.3.2 Specific Objectives

The specific objectives of this study were to:

- i) Study the solidification behavior of selected aluminium alloys with varying amounts of iron, strontium and manganese using thermal analysis techniques so as to establish:-
 - Solidification temperature of α -Al dendrite network,
 - Precipitation temperature of Al-Si eutectic and
 - Precipitation temperatures of intermetallics.
- ii) Study changes in microstructure of cast aluminium-silicon alloys with addition of iron and establish:-
 - Phases present and their morphology,
 - Grain size and volume fractions.
- iii) Study the effects of iron addition on the mechanical properties of aluminium alloys such as; ultimate tensile strength, ductility, hardness and fatigue.
- iv) Study the effects of strontium modification and manganese addition as iron-correcting elements through:-
 - Metallographic analysis of the cast samples and
 - Tensile test, hardness test, fatigue analysis.

LITERATURE REVIEW

2.1 Introduction

Aluminium is among the lightest metals that can be used for various applications as compared with other metals like iron. Throughout history, aluminium has been used in various forms, such as in the form of pig iron, for domestic and automotive as well as structural in the form of castings.

CHAPTER 2: LITERATURE REVIEW

Country, the application of aluminium pigments was limited to decorative uses and coating materials. After World War II, a dramatic increase in the aluminium casting industry occurred, especially in the automotive sector. The use of aluminium and its alloys primarily results in weight reduction which in turn help improve the compressional strength of structures by increasing their ductility and reducing their thermal expansion.

Like most other metals, aluminium is not a ductile metal in its pure state. Thus, alloying is used to improve its properties for most engineering applications. The most common alloying elements are silicon, copper, iron, nickel, zinc, tin, magnesium, and silver. Magnesium, zinc, tin, and iron are considered ferrometals and are considered here to separate as metals and the rest to be controlled properly to attain the quality of aluminium alloys.

2.2 Typical Microstructure of Aluminium-Silicon alloys

The microstructure of the cast aluminium alloy alloys depends strongly on the composition and the casting process. Other factors which influence microstructure are solidification, Al-Si eutectic modifications and heat treatment. Alloying elements in cast aluminium alloys, whether intentionally or unintentionally added, have significant effects on microstructure. Aluminium silicon alloys are generally a composite of hard, discontinuous silicon particles embedded in a ductile aluminium matrix. Binary aluminium silicon alloy close to the eutectic composition (11.7wt.% Si) exhibit spherical or lamellar eutectic alloys which is well dispersed throughout the aluminium matrix. The presence of polyhedral primary silicon particles is frequently observed because of non-equilibrium cooling but slight variations in composition. Primary silicon

LITERATURE REVIEW

2.1 Introduction

Aluminium is among the lightest metals that can be used for structural applications as compared with other metals like iron. Throughout history, aluminium has been used for many different applications including domestic, chemicals and automotive as well as structural. In the earlier part of the 20th Century, the application of aluminium castings was limited to decorative parts and cooking utensils. After World War II, a dramatic expansion of the aluminium casting industry occurred, especially in the automotive industry. The use of aluminium and its alloys primarily reduce the weight of vehicles which in turn help improve the environmental impact of automobiles by increasing their fuel efficiency and reducing their harmful emissions^{2,3}

Like most other metals, aluminium is not commonly used in its pure form. Thus, alloying is used to improve its properties for both wrought and cast products. The most common alloying elements are silicon, copper, iron, nickel, silver, tin, magnesium, zinc, silver, manganese, zirconium, titanium and rare earth elements. Copper, nickel, and iron forms detrimental intermetallics and are considered harmful impurities at certain level that need to be controlled properly to ensure the quality of aluminium alloys.¹

2.2 Typical Microstructure of Aluminum-Silicon alloys

The microstructure of the cast aluminum-silicon alloys depends strongly on the composition and the casting process. Other factors which influence microstructure are solidification, Al-Si eutectic modifications and heat treatment. Alloying elements in cast aluminum alloys, whether intentionally or unintentionally added have significant effects on microstructure. Aluminum silicon alloys are generally a composite of hard, discontinuous silicon particles embedded in a ductile aluminum matrix. Binary aluminum silicon alloys close to the eutectic composition (11.7wt.% Si) exhibit acicular or lamellar eutectic silicon which is well dispersed throughout the aluminum matrix. The presence of polyhedral primary silicon particles is frequently observed because of non-equilibrium cooling and slight variations in composition. Primary silicon,

which is the pre-eutectic silicon formed in hypereutectic aluminum-silicon alloys, tends to assume different morphologies like massive crystals of geometric star like or dendritic shape, complex regular silicon morphology. The predominant form in which primary silicon occurs is massive silicon (or polygonal silicon). The massive crystals of silicon usually found in hypereutectic alloys are bounded by [111] directions.^{4,5}

The ternary phases that can be in equilibrium with aluminum in the Al-Fe-Si system are α -Al₈Fe₂Si (31.6wt.%Fe, 7.8wt.%Si) with a Chinese script morphology and β -Al₃FeSi (25.6wt.% Fe, 12.8wt.% Si) with needle or platelet morphology. In high silicon alloys, δ -Al₄FeSi₂ (25.4wt.%Fe, 25.5wt.%Si) phases with platelet morphology are formed, while γ -Al₃FeSi (33.9wt.%Fe, 16.9wt.%Si) phase forms in high iron and silicon alloys among others like π -Al₈FeMg₃Si₆ phases. The presence of small amounts of Cu, Mn and Cr and the fast cooling facilitates the formation of the cubic, α -Al₁₅Fe₃Si₂ in place of hexagonal α -Al₈Fe₂Si.^{8,13,17}

Mondolfo¹ indicates some of the possible phases in Al-Fe binary system as Al₃Fe (40.7wt.%Fe). The crystal structure indicates a formula between Al₁₃Fe₄ (38.9wt.%Fe) and Al₁₉Fe (39.5wt.%Fe) but some analysis of crystals extracted from alloys are close to Al₇Fe₂ (37.3wt.%Fe). Equilibrium is usually reached during the hot working operations and Al₈Fe₂Si sometimes together with Al₃Fe is normally found in commercial metals.^{21,22,27}

The rapid cooling in pressure die-casting causes fine eutectic structure, small dendritic cells and arm spacing with reduced grain size. On the other hand, slower cooling rates encountered in permanent mold and sand casting necessitates the use of chemical modifiers such as strontium or sodium to obtain finely dispersed eutectic silicon.^{28,29} Chemical modifiers alter the morphology of the eutectic silicon from acicular or lamellar to fibrous with addition of strontium or sodium. Figure 2.1(a), depicts the microstructure of a eutectic Al-Si alloy that is slowly cooled with no primary aluminum; on the other hand, figure 2.1(b) depicting the microstructure of the same alloy cooled at a relatively faster rate shows primary aluminum dendrites.^{30,31,32}

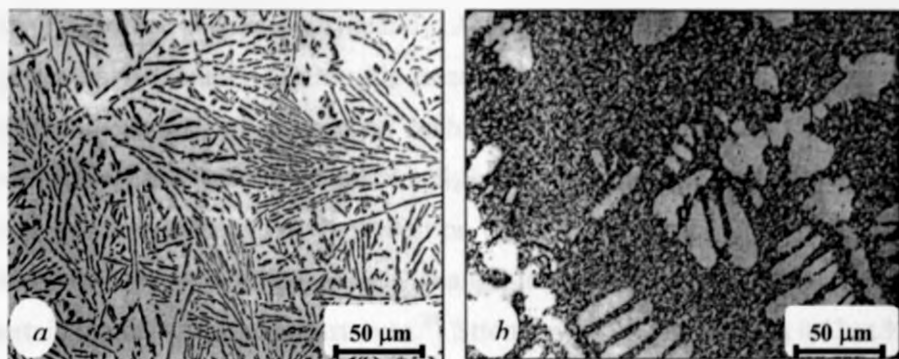


Figure 2.1: Microstructure of Al-12.5wt.% Si alloy; (a) Slowly cooled 200x, (b) Chill cast²⁸

2.3 Effects of Iron on Microstructure of Al-Silicon alloys

The effect of iron on properties of aluminum alloys depend largely on the amount and morphology of iron - bearing phases. The solubility of iron is high in molten aluminum than in solid aluminum. In binary Al-Fe system, the equilibrium solid solubility of iron in aluminum is between 0.03wt.% and 0.05wt.% at the eutectic temperature of 655°C, and much lower at room temperature or in the presence of other alloying elements that form compounds with iron. Iron forms intermetallic compounds with aluminum and several other elements present in the alloy exhibiting a variety of morphologies in form of large or small needles/platelets, Chinese script, spheroid or globular, rosette-like, polygonal, hexagonal, clusters, star-like shapes and/or polyhedral particles. Such morphologies of the iron - bearing phase is known to play a deciding role in the alloys mechanical properties, particularly ductility and strength. Many of these intermetallic phases at times are almost indistinguishable from each other although a particular colour and/or morphology can approximately identify some when observed with an optical microscope. Quantitative electron probe microanalysis (EPMA) technique is commonly used to analyze various second phase particles.^{19,20,24}

Complex intermetallic phases that exist in the microstructure of aluminum alloys containing Si, Mg, Fe, Mn, V, Cr and/or Cu are $Al_{12}Fe_3Si$, $Al_{21}Fe_3Si_5$, $Al_8FeMnSi_2$, $(FeAl_6)Si$, $Al_{12}(Fe,V)_3Si$, $Al_{15}(Fe,Mn)_3Si_2$ (where $Mn > 0.2wt.%$), $Al_9Fe_4MnSi_2$, $Al_5(FeMnCr)Si$, $\pi-Al_8FeMg_3Si_6$, Mg_2Si , $Al_5Cu_2Mg_8Si_6$,

$\text{Al}_{13}(\text{Cr,Fe})_4\text{Si}_4$ (star-like polyhedral), $\text{Al}_9(\text{Co,Fe})_2$ (Chinese script), Al_9FeNi (particle cluster) and $\text{Al}_8\text{CuMg}_8\text{Si}_6$ (needle-like). The presence of such phases in a particular alloy depends on both its composition and the processing conditions. Other phases such as $\text{Al}_4\text{Si}_2\text{Sr}$ have been reported to appear in Sr over modified A356 alloy.^{25,30} Addition of large amounts of modifier ($\text{Na} > 0.02\%$ and $\text{Sr} > 0.01\%$) causes a change in the morphology of silicon in certain regions of the microstructure.³⁴ Strontium levels greater than 0.03wt.% in A356 result in full modification of the silicon phase from flake to fibre morphology shown in fig 2.2(a). Fig 2.2(b) shows unmodified microstructure of the interdendritic region of the Al-8.5Si-2.5Cu-0.4Fe-0.3Mg alloy.^{35,36}

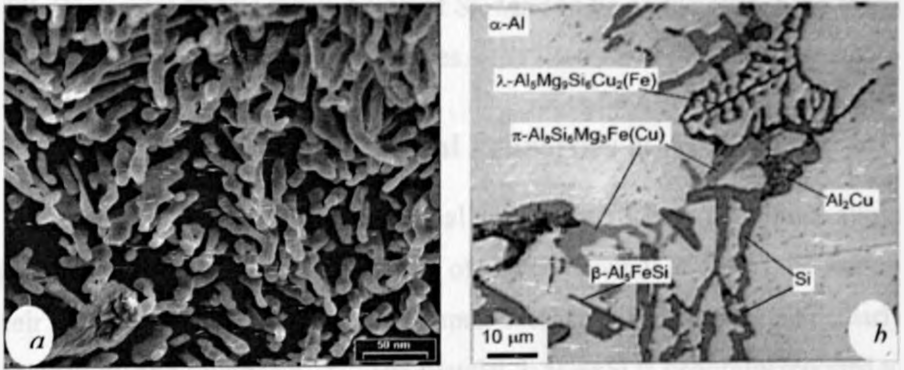


Figure 2.2: Microstructure of (a) modified Si seen as fibers, (b) Al-8.5Si-2.5Cu-0.4Fe-0.3Mg alloy²⁴

With low silicon content or in alloys containing Mg, Cu, Be or Zn, $\beta\text{-Al}_3\text{FeSi}$ platelets may appear as Chinese script. In the presence of Mg, the compound of $\text{Al}_8\text{FeMg}_3\text{Si}_6$, $\text{Al}_{10}\text{FeMg}_4\text{Si}_4$, $\text{Al}_5\text{FeMg}_8\text{Si}_6$ or $\pi\text{-Al}_8\text{FeMg}_3\text{Si}_5$ (when Sr and Mg $\sim 0.7\text{wt.}\%$ are present) may form as Chinese script when it is a eutectic or as globules when it is primary. Magnesium also combines with Sr to form a complex, $\text{Al}_4\text{Mg}_2\text{SrSi}_3$, intermetallic compound.²² When copper is present, iron may be associated with it forming acicular compound of Al_5FeCu_2 or $\text{Al}_8\text{CuMg}_8\text{Si}_6$ phase. The Chinese script of Al_3CuFe phase forms with 0.55wt.% Fe.^{18,29} Particle clusters of $\text{Al}_5\text{Cu}_2\text{Mg}_8\text{Si}_6$ form in the presence of $\text{Cu} > 1\%$ and $\text{Mg} > 2\text{Cu}$ or when Mg, Cu and Sr are present respectively.⁴² In addition, the Cu phase is observed mainly as pockets of Al-Al₂Cu eutectic

dispersed over the aluminum matrix, nucleated along the sides of the eutectic silicon particles and β -Al₅FeSi phases.^{37,38} Copper also forms Al₆(Fe,Cu) and Al₇FeCu₂ with iron, Al₆(Cu-Fe,Mn) and Al₂₀Cu₂Mn₃ with manganese, Al₇Cu₄Ni and several other compounds with Ni and iron. The copper compounds formed are controlled to some extent by the amount of silicon available. Thus silicon above 1% favors the Al₅SiFe phase over the iron-copper compounds and Al₁₅Si₂(CuFeMn)₃ over the Al₆(Cu-Fe,Mn) and Al₂₀Mn₃Cu₂ compounds.³⁹ When copper exceeds 5wt.%, commercial heat-treatment cannot dissolve it and the network of eutectics does not disintegrate. Structure of as-cast and heat-treated alloys have little difference at 10% to 15% Cu content.²⁹ The precipitation of Si, Mn and Fe on the other hand forms Al₁₅(Fe,Mn)₃Si₂ and Al₈FeMnSi₂ phases.^{40,41}

2.4 Effect of Iron on Mechanical Properties of Al-Si alloys

The effect of iron on the mechanical properties of cast aluminum alloys depends on the type and morphology of the compounds it forms, as well as their quantities. Iron is reported to impair mechanical properties particularly the ductility and toughness.^{28,29} The platelet β -Al₅FeSi is generally reported to be the most detrimental to mechanical properties.^{42,43}

2.4.1 Tensile Properties

Quality index (QI) which is an empirical relation between the materials UTS and ductility [given as $QI (MPa) = \sigma_{UTS} + a \log\%(\text{elongation})$] is found to decrease with iron levels above 0.1wt.%.¹⁴ The coefficient "a" depends upon the type of alloy, the fineness of the microstructure, the soundness of the casting and the solution heat treatment. There is also a reduction in tensile elongation with an increase in the iron content which is attributed to the presence of the β -Al₅FeSi phase.^{19,44}

Addition of Be, Cr and Sr increases the percentage elongation and tensile strength. Beryllium addition and/or strontium modification result in a significant improvement in elongation of A357. This improvement may be due

to the formation of the less harmful $\alpha\text{-Al}_3\text{Fe}_2\text{Si}$ phase in the Be-containing alloy by reducing the amount of primary $\beta\text{-Al}_5\text{FeSi}$ phases and spheroidization and decrease of the silicon particles. However, beryllium addition and sodium modification have a negative impact on mechanical properties at low iron levels below 0.05wt.% Fe.^{28,32,38} However, the tensile strength increases with addition of beryllium and strontium. The addition of beryllium to aluminum-silicon alloys transforms the needle-shaped iron-rich phase into the Chinese-script shape. Strontium modifies the brittle flake eutectic silicon to fiber-like (sphere-like) and may refine the iron rich phase.^{29,45} Increasing iron and magnesium has a slight effect on yield strength. Some results carried on an A357 alloy indicates that there is a consistent decrease in yield strength with increasing iron from 0.02wt.% to 0.1wt.% Fe. Couture¹⁸ however reported that iron does not affect the yield strength of chilled castings, but it increases the yield strength of sand casting.

It is also reported that iron contents up to 0.5wt.% enhance the ultimate tensile strength, σ_{UTS} , after which it reduces at levels of Fe > 0.5wt.%. Other researchers found that iron addition slightly reduces tensile strength, σ_{UTS} , linearly. This reduction in tensile properties has been attributed to the precipitation of the coarse needles-like, $\beta\text{-Al}_5\text{FeSi}$ and the π -phase. Study of Al-Si alloys containing 11.38 to 13.86wt.% Si, indicates that, increasing the iron content up to about 0.5 to 0.75% raises the tensile strength of sand-cast test bars. Beyond 0.75wt.%, iron additions reduce tensile strength.^{48,49}

The modulus of elasticity and that of rigidity increases as iron increases while ductility, Poisson ratio and impact energy reduces greatly.⁴³ Addition of manganese and chromium slightly improves both the modulus of elasticity and ductility to alloys with iron content. Chromium additions to Al-7Si-0.3Mg, (356) lead to coarse $\beta\text{-Al}_5\text{FeSi}$ platelets to be inhibited and some transformed to the Chinese script $\alpha\text{-Al}_{13}(\text{Fe,Cr})_4\text{Si}_4$ phase. In Al-13Si, 0.5wt.% Mn is reported to suppress the β -phase when Fe < 1.5% thus counteracting embrittlement caused by iron while beryllium and strontium addition improve ductility.⁵²

2.4.2 Hardness Properties

Hardness implies a resistance of metals to permanent or plastic deformation. It is largely a surface phenomena influenced by yield strength, tensile strength, work-hardening, modulus of elasticity and other material properties. Hardness in aluminum alloys increases with the iron-content.^{30,32,35,36} This is attributed to the formation of brittle β -Al₅FeSi plates and π -Al₁₉FeMg₃Si₆ intermetallic phases. These compounds are essentially insoluble and may be responsible for an improvement in strength, particularly at elevated temperatures. Addition of strontium decreases the hardness and strength of the magnesium-containing alloys, which could probably arise from a retardation of the precipitation of Mg₂Si during the aging process. Hardness is also affected by the grain size. This is probably because the needle iron-rich phase is brittle and less bonded to the aluminum-matrix.

2.4.3 Fatigue Properties

Factors influencing fatigue performance of different aluminum alloys reported by various researchers are casting defects, oxide films, heat-treatment, dendritic arm spacing, solidification rate, modification and intermetallic particles. It also depends on stress state and microstructural characteristics such as flow size, grain size, dendrite cell size and matrix yield strength. Fatigue life is strongly controlled by the size of larger pores, crack nucleation and propagation phases mainly β - phase.⁴³

In Al-Si alloys, the cracks nucleate at the pores or β -platelets, thus increased porosity results in reduced fatigue strength.⁵¹ Wang et al⁵² found that increasing iron-content reduces low-cycle fatigue life of aluminum die-casting alloys but does not have a significant effect on high-cycle fatigue life. It was also found that fatigue life of the higher and medium iron-containing alloys was lower compared with alloys having lower iron content.⁵³ This is linked to the presence of β -Al₅FeSi that facilitates increase in shrinkage porosity but could be improved with addition of beryllium. In beryllium and manganese added alloys, even though cracks nucleates at the (Be, Mn)-Fe Chinese scripts,

they will get arrested as they approach α -Al and hence cracks have to propagate along silicon particles. The increase in fatigue life with silicon content is believed to result from the lower tendency of shrinkage porosity formation and higher yield strength.^{19,20,43}

2.4.4 Creep Properties

Creep is the slow permanent deformation of a metal with time under constant tensile loading at an elevated temperature. In the Al-Fe system, iron significantly increases the creep strength, but reduces the fatigue strength, especially if massive crystals of Al_3Fe are present. It is reported that iron along with other elements like copper, nickel, cobalt, magnesium and chromium increases the creep strength of aluminum - silicon alloys. However, in aluminum - magnesium alloys, the Al_8Mg_5 compound may form as coarse particles (when Mg > 2wt.%) that reduce the alloys creep.^{35,52}

2.5 Effects of Iron on Chemical and Physical Properties

Corrosion is the chemical degradation of metals and alloys. Corrosive attack often produces pitting of aluminum alloy on the surface. The pits act as notches producing a reduction in fatigue strength. In Al-8Si-3Cu, iron increases corrosion susceptibility. Additions of iron results in formation of Al_3Fe particles that are cathodic to the aluminum matrix dispersed throughout and shift the corrosion from the intergranular to the pitting type. The addition of manganese may absorb the iron in Mn-Fe compounds thus reducing the amount of Al_3Fe and its pitting effect. Copper additions to aluminum die-casting alloys improve strength and fatigue resistance but at the expense of corrosion resistance. Other chemical neutralizers that can alleviate the detrimental effects of iron are; Chromium, Beryllium, Nickel and Cobalt.

Beryllium does reduces the oxidation rate of magnesium in the melting process by forming a protective layer on the melt and it also scavenges iron by reducing the number of iron-bearing phases and modifying their morphology. But some foundries hesitate to use beryllium due to its high toxicity.³⁷

Addition of iron in the Al-Si system reduces both the electrical and thermal conductivity of aluminum. Thermal expansion too decreases linearly with iron increase while magnetic properties are not greatly affected by iron addition. However, viscosity of molten alloys increases with iron addition but there is no appreciable change in surface tension.⁵²

2.6 Effects of Iron on Castability of Aluminium-Silicon alloys

In aluminium alloy foundry, castability refers to those properties of the alloy that characterize its behavior during casting process. The characteristics that should be considered in the casting process are the alloys' sludge formation tendency, die soldering tendency, hot tearing resistance, fluidity and porosity formation. The above casting characteristics are found to depend on the casting processes, design of mould and feeding system, melting practice such as degassing, filtration and modification, and alloying elements present on a molten metal. Certain casting characteristics are not important in some casting processes. For instance, die-soldering resistance is not necessary in sand casting while pressure die-casting needs an alloy with good die-soldering resistance.⁶⁵ It is also desirable that prior to manufacturing process the alloy to be cast should be easily machinable and weldable.

2.6.1 Sludge Formation Tendency

Sludge in foundry is the build-up of solid heavy element compounds on the floor of the melting and holding furnaces. Sludge are oxides of aluminium (Al_2O_3) and magnesium (MgO) and primary crystals that contain Al, Si, Fe, Mn, Mg and/or Cr, such as star-like and polyhedral phase of $\alpha - \text{Al}_{15}(\text{Mn,Fe,Cr})_3\text{Si}_2$ ²² This sludge tends to accumulate on the base of the furnaces due to their high melting points and high specific gravity. The net effect is to reduce the effective capacity of the furnace.^{34,51} The sludge crystals entrained into castings decrease the alloy's fluidity, make machining difficult, and may also increases the die-soldering tendency. The major factors that determine the quantity, size and morphology of the sludge that forms in aluminium die casting alloys are the Fe, Mn and Cr content of the alloy and

the cooling rate. Jorstad and Gobrecht [as reported by Shabestari¹⁵] studied the sludging phenomenon and defined a sludge factor (SF) for Al-Si-Cu alloys calculated from the Fe, Mn and Cr contents of the alloys as follows:

$$\text{Sludge factor (SF)} = (1 \times \text{wt.\% Fe}) + (2 \times \text{wt.\%Mn}) + (3 \times \text{wt.\%Cr}) \text{----}[2.1]$$

Although the Jorstad's relationship is widely accepted, inconsistency exists in such sludge factor formula, and therefore, some prefer the relation:

$$\text{Sludge factor (SF)} = (1 \times \text{wt.\%Fe}) + (1.5 \times \text{wt.\%Mn}) + (2 \times \text{wt.\%Cr}) \text{----}[2.2]$$

Sludge factor assists in determining the sludge formation tendency of the alloy and the quantity of sludge that may form.^{47,48.}

For a given iron content, Jorstad and Gobrecht also found that sludge only forms if a certain critical temperature is reached. Nucleation and diffusion are key issues involved in determining the critical temperatures and times of formation. The following relation was given by Shabestari¹⁵ to describe the dependence of sludge-forming temperature on the alloy's iron content;

$$\text{Temperature (}^\circ\text{C)} = 645.7 + 34.2(\text{wt.\% Fe})^2 \text{-----}[2.3]$$

It was also found that, the amount of sludge formed in an alloy is inversely proportional to holding temperature.^{22,33.} For instance, at holding temperature of 670°C for three hours, small star-like iron-rich particles were found in samples from A380 melts but this phase was not detected in A380 melts that were held at 720°C for same three hours. Such particles may dissolve in the melt at high holding temperature but may not dissolve completely at lower temperature. If the weight percentage of iron, manganese and chromium exceeds certain critical totals for a particular holding temperature, then sludge formation may occur. The sludge formed may have a composition of either $\text{Al}_{15}(\text{Mn,Fe,Cr})_3\text{Si}_2$ or $\text{Al}_{15}(\text{Mn,Fe})_3\text{Si}_2$. These are approximate compositions and may actually include small additional amounts of other elements such as Cu and Zn as well.^{47,65}

Flores et al [as reported by Cao et al³⁹] found that in Al-Si-Cu alloys at temperatures in the range of 610°C to 660°C, sludge in the form of

Al(Fe,Mn)Si is formed when the composition exceeds 0.06wt.%Fe, 0.5wt.%Mn and 8wt.%Si. These findings suggested that the Al(Fe,Mn)Si type sludge forms most readily at about 640°C.^{33,49}

Sludge particles were found to be much harder than the Al-matrix though softer than the primary silicon particles. The Vickers hardness number of the polyhedral, star-like and blocky particles is about 840 and those of the needle-like particles are about 650 while hardness of the aluminium matrix is 75.¹⁵ The amount, size and morphology of sludge particles depend largely on the alloy chemistry and on the cooling rate. Slower cooling rate, with strontium and manganese additions, favors the formation of sludge, with large Chinese script, platelets and polyhedral particles.⁴⁰ At high cooling rate, the size of sludge particles in form of star-like particles decreases to an extent that they may not contribute to sludge. The morphology of the iron-rich phases is also influenced by the ratio of Fe:Mn:Cr in the alloy. Generally, higher manganese levels leads to more Chinese script and a higher chromium levels favors the formation of polyhedral, star-like and blocky particles. Iron-rich, needle-like sludge particle surrounded by a primary silicon particles are detrimental to the alloy's mechanical properties. Such detrimental morphologies can be altered by addition of manganese, chromium or some other elements.

Sludge formation has therefore been shown to be dependent on the alloys chemistry, melting and holding temperatures, rate of cooling and poor-melt handling of die casting alloys with high levels of iron.¹⁵

2.6.2 Die-Soldering Tendency

Die-soldering refers to the sticking of molten aluminium alloys onto the inner surface of the ferrous-based die and core materials. It is a major concern in the die casting industry since it leads to malfunctioning of the die inserts causing significant decrease in productivity. The diffusion of iron from the die into the boundary zone of the casting, and the subsequent formation of Al-Fe-Si intermetallic phases is the main reason for the steady sticking of aluminium alloy on certain tool parts.

Kajock et al [as reported by Cao⁴¹] observed that the mechanism of soldering is purely based on the diffusion and chemical reactions of the elements in the die and the liquid metal, while Venkatesan et al [as reported by Morinaga et al⁴⁵] have shown the effects of temperature, gate velocity and gate design on the washout in dies. Thus, the molten aluminium entering the die with high velocity destroys the protective film on the die surface.

There are two types of soldering phenomena; impingement and deposition. Impingement soldering takes place in the vicinity of the gate when the molten metal stream strikes the die surface. It is aggravated by high plunger speeds and poor gate design. Deposition soldering occurs in those areas of the die where the metal velocity is low during filling and where washout occurs.

Diffusion of iron atoms from the ferrous die into the aluminium melt causes the formation of a series of binary and ternary intermetallic phases onto which the aluminium alloy solders. An iron-aluminium binary phase of an orthorhombic η -Al₅Fe₂ containing silicon and chromium forms at the inner compact layer next to the steel substrate.

The ternary phase α -Al₈Fe₂Si forms above the binary phase as a thin and continuous layer while a layer of θ -Al₁₃Fe₄ forms in-between the η -Al₅Fe₂ and α -Al₈Fe₂Si phase layers.³⁶ Zinc, manganese and other minor elements in the melt precipitate on the grain boundaries of the ternary α -Al₈Fe₂Si phase layer, while chromium, vanadium and other minor elements present in H-13 tool steel precipitates as phases in the binary η -Fe₂Al₅ phase layers.

Castings often have to be manually removed from the die chamber and damaged die surfaces require polishing to repair. This is costly in terms of lost production time, labour cost for polishing and shortening of die life.

Various die casting parameters have been found to play a critical role during die soldering. The dominant ones are; die lubrication and coating, die design and operating parameters such as temperature of the metal and die, chemistries of casting alloy and intermetallic layers. Materials that can withstand high temperature conditions such as graphite, boron compounds, TiN, Ti(C,N) and

WC-Co can withstand die soldering. Surface treatments such as nitriding are also found to reduce abrasive wear and improve thermal fatigue.²⁰

Use of molybdenum in place of H-13 die steel will also help to reduce soldering. However, molybdenum is more expensive and softer than H-13 steel and hence has a shorter lifetime. High metal and die surface temperatures lower the surface hardness and make the die surface less wear resistant. It also favors the growth of intermetallic phases by increasing the diffusion rate of the atoms of iron and aluminium. High temperatures may also break the lubricant film, and decrease its ability to prevent soldering. Holding temperature of the melt at $\sim 663^{\circ}\text{C}$ (1225°F) could minimize the occurrence of hot spots in the melt. Metal and die temperatures should also not be too low to cause poor filling or to result in the formation of cold soldering.

Aluminium exhibits a strong adhesive tendency to stick to iron. There is existence of an intermetallic layer consisting of zones of intermetallic compounds such as Fe_2Al_5 , Fe_3Al and FeAl_3 phases. Presence of silicon, copper and magnesium also results in the formation of complex intermetallic compounds in the intermediate layer. The soldering tendency diminishes as iron content approaches its maximum solubility in aluminium of 1.8wt.% iron at 650°C and 3wt.% iron; at 700°C . Iron content also influences the growth of intermetallics, which has a direct influence on the soldering. Use of high iron level alloys in the range of 0.5wt.% up to 1.3wt.% iron reduces soldering. However, excess iron results in a sludge formation. Manganese has a beneficial effect on soldering and is added to around 0.8% to compensate for low iron alloys with 0.4wt.% Fe. A titanium addition up to 0.125wt.% forms aluminides with aluminium and silicon in the melt, and thus reduces the polygonal iron aluminides sludge crystals in the melt. Nickel and chromium contents in the melt should be avoided because nickel ties down the effectiveness of the manganese while chromium increases the sludge factor.^{3,8}

2.6.3 Hot Tearing

When a casting alloy solidifies, tensile stresses are generated which might exceed the fracture stress of the partially solidified alloy resulting in hot tearing and cold cracks. This implies that the solid which forms at the mold wall during solidification of the casting should be more ductile and be able to deform in order to relieve tensile stresses set up during solidification. Some aluminium foundry alloys are more prone to hot tearing than others. Commercial Al-Si and Al-Si-Cu alloys with silicon content close to the eutectic have the highest hot tearing resistance. According to Makhlof et al⁶⁵ addition of iron improves the hot tearing resistance. This is due to decrease in solidification shrinkage and increased high temperature strength of Al-Si alloys with increased iron content. Modification with 0.02wt.% strontium tends to eliminate hot tears. Other elements like Ni, Cr, Co and Mo with high melting temperature can slightly improve hot tearing resistance, while zinc addition decreases the high temperature strength and thus tends to increase the alloys hot tearing tendency.²⁷

2.6.4 Fluidity

Fluidity of an alloy is the capability of the melt to fill the mould cavity. Fluidity of molten alloys can be measured in three ways; (i) measuring the maximum distance to which the metal will flow in a standard-fluidity testing mould, (ii) measuring the volume of flow through a given section before flow stops and (iii) measuring the pressure loss between two points placed a given distance apart in the alloys' flow path. Fluidity is affected by several factors such as the viscosity of molten metal, surface tension, inclusions, solidification pattern of the alloy, mold design, mould material, melt super-heat, rate of pouring, mold-metal heat transfer, mould cleanliness and mold vibration. Increase in silicon content tends to reduce the viscosity of molten Al-Si alloys. The minimum fluidity is found at around 5 – 6wt.% silicon content, while maximum fluidity is shifted to the hypereutectic composition of

around 18wt.% silicon. Viscosity of aluminium diecasting alloys is reported to depend more on temperature than alloy composition.⁶⁵

If the surface is subjected to a sharp curve against a non-wetted mould, then it will be subjected to a repulsive force, which will resist the entry of the metal. This is especially so if the sections are so thin that they become difficult to fill because of the resistance due to surface tension. Alloys with long freezing range have lower fluidity than alloys with shorter freezing range. Smooth crystals of solidifying intermetallic compounds create less resistance to melt flow.⁴

Addition of Sr modifier, Fe, Mn, Cr, Ni and Mg tend to reduce fluidity of an aluminium alloy due to the formation of intermetallic inclusions. Inclusions formed from oxidation of some alloying elements such as magnesium that forms on the melt surface also tend to increase the alloy surface tension. An addition of iron content to aluminium alloy decreases the fluidity due to increase of the insoluble iron bearing phases e.g. $\text{Al}_8\text{FeMg}_3\text{Si}_6$, but there is no appreciable change in surface tension.⁸

Fluidity increases with reduction in the rate of mould-metal heat transfer. Slow heat-transfer rates, in sand casting, result in higher measured fluidities than in more rapid heat-transfer processes in die-casting. Thus insulating ceramic coatings are applied to gravity and low pressure dies while carbon black is applied from a sooty flame to sand moulds to give very substantial increases in fluidity.

Melt super-heat is the difference between the liquidus temperature and the pouring temperature, and it determines the amount of excess heat that must be removed from the liquid metal before solidification can commence. In the Al-Si-Cu alloy system, an increase in the silicon content (to ~ 13wt.% Si) and the copper content of the alloy decreases the alloy's liquidus and solidus temperatures and thus increases melt fluidity.

The effect of melt cleanliness on casting fluidity may completely mask any other composition-related changes to fluidity arising from variation in viscosity or actual surface tension.

Flow pattern and stopping mechanism in die-casting are different from those in sand and permanent mold casting because the melt fills the die cavity at high pressure and velocity. This significantly enhances filling ability of the alloy in die casting.

2.6.5 Porosity Formation

Internal porosity within a casting must be controlled or reduced in order to avoid detrimental effects to the mechanical properties, pressure tightness and machined appearance of the cast. There is consensus in the casting industry that internal porosity is of two basic types; gas porosity and shrinkage porosity. Gas porosity occurs when a gas dissolved within the melt is released during solidification because of its reduced solubility in the solid phase. Hydrogen is the only significant gas involved in aluminium alloys. Shrinkage porosity occurs in regions within the casting which solidify last.

The role of silicon in Al-Si foundry alloys is complex. Shahani [as reported by Taylor et al³⁶] found that porosity levels increased as the silicon level was increased up to 7wt.% for equal hydrogen concentrations in Al-Si binary alloys. While Berezyanskaya et al³⁶ found that increased silicon levels caused a decrease in porosity levels after he studied a range of Al-Si-Cu-Zn-Mg-Fe-Mn alloys for silicon range of 4.1wt.% to 11.2wt.%. It is also reported that increase in iron, magnesium and manganese increases porosity.¹⁹ As reported by Mbuya et al⁸ equilibrium hydrogen gas pressure associated with a given amount of dissolved gas increases with iron content. Also, iron forms iron-bearing phases of β -Al₅FeSi which serves as effective pore nucleation sites in Al-9Si-3Cu alloys. At lower cooling rates with high percentage of magnesium, the Al₅FeSi needles may transform into Al₈Mg₃FeSi₆, which also has a negative effect on porosity.⁹

Modification with trace elements is often associated with changes in porosity in castings. Unmodified castings usually have large macro pores and shrinkage. Upon modification, large macro pores are replaced with fine distributed porosity. The differences in porosity distribution between a modified and an unmodified alloy have been attributed to several reasons, which are briefly discussed below.³⁶

1. The large difference in solubility of hydrogen gas in solid and liquid Al alloys (See Figure 2.3) causes the hydrogen gas to become entrapped in the solid, forming pores. The presence of strontium at levels above 0.01wt.% leads to increased hydrogen solubility in the melt causing more porosity.

2. Poor feedability in a casting leads to unfilled zones in the interdendritic regions causing the formation of pores. However, feedability itself is affected by many parameters, such as solidification range, liquid-solid interfacial energies, feeding paths, eutectic nucleation and growth, and the volume fraction and shape of intermetallic phases. Strontium is known to affect the solidification range and the liquid-solid interfacial energy of aluminium-silicon alloys, thus it can change the porosity distribution in modified alloys.

3. The presence of inclusions, such as oxides, nucleates pores and strontium based oxides act as extra nuclei for hydrogen pores.

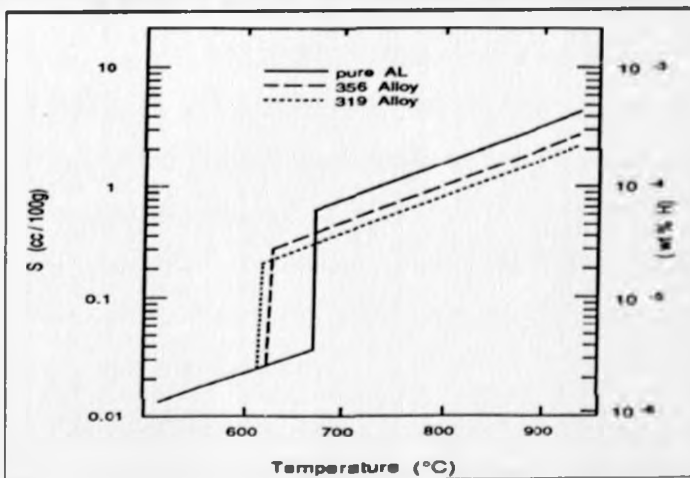


Figure 2.3: Solubility of hydrogen in pure aluminium, 356 and 319 alloys³⁶

Hot isostatic pressing (HIP) performed before the heat treatment process is reported to be an effective means of increasing the fatigue life of critical application parts by reducing the shrinkage and gas porosities inherent in the casting. The HIP process surrounds the castings with a pressurized gas that imparts a hydrostatic stress on the component. This compressive stress, in tandem with elevated temperatures, shrinks and heals potential stress-intensifying pores. The micrographs in figure 2.4 show the effects of HIP densification. In figure 2.4(a), the pores marked with arrows for the un-HIPed sample seems to have been eliminated in the HIPed sample as observed in figure 2.4(b).¹⁹

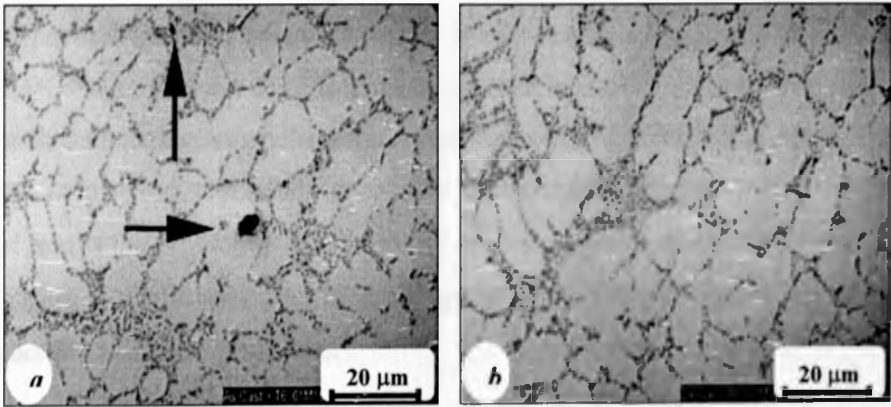


Figure 2.4: (a) Cast Al-Si-Mg alloy in T6 condition; arrows show porosity, (b) Cast Al-Si-Mg alloy in HIPed T6 condition; no evidence of Porosity¹⁹

2.7 Control of Iron Intermetallic Compounds and Removal of Oxide Films from Aluminum-Silicon Castings

The β -phase has undesirable characteristics because of its brittleness and weakness in mechanical properties. It was found to cause a sharp decrease in elongation to fracture and it also degraded the workability of aluminum alloys. It is therefore desirable for the iron compounds to crystallize in the less harmful form of α - (BCC) phase. Chinese script shape is less detrimental to the tensile properties of the alloys than the needles.^{30,34} This has been achieved through a number of approaches such as; reducing iron content of an alloy, increasing the cooling rates which tends to shift the eutectic towards higher iron contents hence dispersing the β - crystals, causing a decrease in DAS and application of high temperature melt heat-treatments prior to casting or by sedimentation or electromagnetic methods.^{38,40} Addition of neutralizers like manganese, chromium, cobalt, etc is also commonly used. Neutralization of iron is the promotion of compact or α -Chinese script morphologies and the inhibition of the β -platelet morphology with the goal of improving strength, ductility and other properties.^{49,54}

2.7.1 Effects of Solution Heat Treatment

Foundry alloys are often given a solution heat-treatment before age hardening. It is a process of heating the castings to a temperature below the solidus for a prolonged period to allow the alloying elements to go into solid solution. The purpose of a solution heat-treatment in Al-7Si-Mg casting alloys is to obtain the optimal combination of strength and ductility by dissolving Mg_2Si -containing phases, so as to place as much Mg in solution as possible, homogenize the cast microstructure, improve the morphology of the eutectic Si particles and dissolve Fe-particles.⁴⁴

The solution heat-treatment temperature is usually 540°C for an A356 (7%Si, 0.3%Mg) alloy for 12 hours.³¹ Recent quantitative metallographic data indicates that the π - Al_8FeMg_3Si or $Al_9FeMg_3Si_5$ phase transforms to the β -phase of very fine plates in alloys with low Mg contents, (0.3 ~ 0.4wt.%Mg).

and that the β -phase is often associated with decomposed π -remnants. At high Mg levels (0.6 ~ 0.7wt.%), the π -phase appears to be largely resistant to change during solution treatment. Alloys with intermediate Mg levels (~0.5wt.%), display a partial transformation of π -particles to β - phases. Close observation reveals that the clusters of β -needles are often in close proximity to π -phase particles of varying size. The as-cast “Chinese script” Mg_2Si phase is completely dissolved by solution treatment in the lower and intermediate Mg alloys. Some Mg_2Si remains in the higher Mg alloys in the form of isolated globularised particles. Complete Mg_2Si dissolution appears to be more likely to occur if the Fe content is low (0.05wt.%) rather than high (0.20wt.%).

It is reported by Niels et al²⁵ that during the homogenization process, at temperatures between 530°C – 600°C, plate-like monoclinic intermetallic β - Al_5FeSi particles transform to multiple rounded α -particles. This phase transformation improves the processability of the aluminum considerably. The plate-like β -particles can lead to local crack initiation and induce surface defects. The more rounded α -particles in the homogenized material improve the extrudability of the material and the surface quality.

Moustafa¹¹ reported that the hardness and strength (YS, UTS) of Mg-containing alloys decrease with the addition of strontium. This is due to the sluggish dissolution of the $Al_5Cu_2Mg_8Si_6$ and α - $Al_{15}(Mn,Fe)_3Si_2$ phase during solution treatment, at 500±2°C for 24 hours, and a delay in the precipitation of Mg_2Si or Al_2MgCu phases during artificial aging at 155°C for 5 hours thereafter. The properties of the Cu-containing alloys, however, remain unaffected by the addition of Sr. The plate-like β - Al_5FeSi phase, which may nucleate on SrO particles during solidification, was found to partially dissolve during solution treatment through the diffusion of Si atoms into the surrounding aluminum matrix. The presence of dissolved Ni and Cu in the α - $Al_{15}(Mn,Fe)_3Si_2$ phase contributes to its stability during solution treatment. The modification effect of Sr on the β - Al_5FeSi platelets is intensified in the presence of Zn following solution heat-treatment at 500°C for 24 hours.

Experiments carried out by Lee et al,²⁹ showed that the increase of the solution temperature reduces the quantity and average length of β - Al_5FeSi platelets, enhance the dissolution of the copper intermetallics and effectively improve the mechanical properties. By adding Be to the A319 alloy and optimizing solution treatment temperature, the number of fracture initiation sites of β - Al_5FeSi platelets is decreased and the tensile properties and fracture toughness is significantly improved. Apelian et al⁵⁹ reported that a thorough study conducted on the effect of iron in A357 alloys with and without the presence of Be shows that the detrimental effect of iron is caused by the precipitation of the $\text{Al}_{10}\text{Mg}_4\text{Si}_4\text{Fe}$ intermetallic phase, which does not dissolve in solution heat-treatment. In this intermetallic, iron ties up Mg and thus reducing the Mg content available for strengthening.

2.7.2 Cooling Rate Effects

High cooling rates also neutralize the effect of iron. The critical iron content at which the β - phase appears, with no manganese, is found to be 0.75wt.%Fe at a cooling rate of 1°C/s, 0.90wt.%Fe at a cooling rate of 5°C/s and 1.0wt.%Fe at a cooling rate of 10°C/s. Anantha et al,³⁵ suggested 5°C/s and 10°C/s as the optimum cooling rate for the best microstructure for 319 and 413 alloys respectively. At these cooling rates, all of the iron compounds were absent except for the star-like intermetallics, the volume percent of which was minimal (less than 0.2%).

Couture¹⁸ reported that the deleterious influence of iron on the tensile strength and elongation is more marked in the slowly cooled than in the chilled metal. Samuel et al⁵⁵ also found that, increasing the cooling rate results in the precipitation of the α -Chinese script form with no β -needles visible in the microstructure. The strontium-modified alloy, particularly at the slowest cooling rates shows the precipitation of pre-dendritic α -phase and the absence of β -needles.³¹ This would be accounted for in part by the influence of strontium on the fragmentation and dissolution of the β -platelets. At the highest cooling rate, close to die casting conditions, only pre-dendritic α -

Chinese script phase is observed, situated within the α -Al dendrites. Furthermore, faster cooling rate facilitates the finely dispersed nucleus with smaller secondary dendritic arm spacing (SDAS)¹⁴ and since the β -Al₃FeSi platelets form mainly in the inter-dendritic spaces, the phase size can be controlled and restricted.^{25,32} The strontium and manganese combined addition, together with higher cooling rate is found to be the most effective method to modify the intermetallic compounds.³¹

There is no unanimity amongst the various sources consulted on the effect of iron on the mechanical properties of aluminum casting alloys. For instance, some reported increase of tensile strength while others argue reduction of it. However, in general, iron is detrimental. Various methods are advocated to decrease the influence of iron when it is present above a specified level. Rapid cooling may be effective, but, if this is not sufficient or feasible, neutralizers, such as manganese produce consistently good results. The amount of manganese needed to neutralize iron varies with cooling rate during solidification. Manganese was found to inhibit β -Al₃FeSi formation for Fe<1.2% in thin, chilled sections and when Fe<0.75% in sand cast steel bars.¹⁹

2.7.3 Effect of Melt Treatment

Melt treatment of aluminum-alloys is a process of treating the molten metal prior to casting to improve the properties, surface appearance and entire microstructure of the alloy. It removes both oxide films and primary intermetallic compounds from aluminum melt. It is shown that thermal melt treatment can significantly refine the primary silicon in hyper-eutectic Al-Si alloys including the primary α - phase and intermetallic compounds and improve alloy mechanical properties.⁶³ Increasing the superheat temperature increases the cooling rate and hence results in refinement of the eutectic silicon and iron intermetallics from β -Al₃FeSi phase to the α - phase without any addition of external elements.⁵⁵ A study on 319 alloy by Anantha et al³⁵ shows that at a melt temperature of 750°C (super-heat of 140°C), the iron intermetallics crystallized in the α - phase form at manganese concentrations

of 0.5%. Upon melt superheating to 850°C (superheat of 240°C), the α - phase particles were present on 413 alloy containing 1.2%Fe, 0.3%Mn, and 0.1%Cr.

The profound influence of superheating temperatures on the crystallization behavior of primary α iron containing particles might be related to the transformation of oxide films from γ -Al₂O₃ or η -Al₂O₃ to α -Al₂O₃. With the increase of melt super-heating temperature, there is a decrease in volume fraction of primary α iron particles. In the absence of magnesium, increasing the super-heat temperature of A380, 319 or eutectic Al-13%Si-1.5%Fe-0.06%Mg alloys from 750°C to 1020°C does not change the nature of oxide films or their ability to nucleate β -Al₃FeSi. However, when magnesium is added to the melt, the kinetics of Al₂MgO₄ formation may not allow for nucleation of β -Al₅FeSi to take place.^{55,56}

2.7.4 Iron Correcting Elements

The other method of controlling the formation of β - phase has been through the addition of iron correcting elements such as Mn, Cr, Co, Mo, Be, V, W, Cu, Ni or the rare earth elements like Y, Nd, La and Ce.^{38,49} Most commonly used are Be and Mn. Beryllium apart from reducing the oxidation rate of magnesium during the melting process also tends to “scavenge” iron by reducing the number of iron-bearing compounds and also by favorably modifying their morphology.⁵⁰ The addition of beryllium could; (i) reduce the amount and modify the morphology of iron intermetallics from platelet-like β -Al₅FeSi phases to comparatively harmless Chinese-script α -Al₈Fe₂Si phases, (ii) enhance the precipitation kinetics and increase the amount of strengthening precipitates by releasing back into the alloy the magnesium otherwise tied up in the iron-compounds, (iii) spheroidize and decrease the size of the silicon particles.^{38,50} Beryllium has the most profound iron-neutralizing effect with an optimal level of 0.26wt.%Be per 1wt.%Fe.³ Beryllium transforms the needle β -Al₅FeSi into Be-Fe type phases of (Be-Fe)-Al₈Fe₂SiBe/Al₄Fe₂Be₅ with Chinese script morphology and AlFeBe₄ at additional levels of 0.2wt.% – 0.5wt.%.⁴⁸ However, beryllium has toxic effects especially during welding.⁴⁶

Manganese addition transforms β -Al₅FeSi plates into Chinese scripts, α -Al₁₅(Fe,Mn)₃Si₂ and irregular shapes. The amount of manganese plus iron should not exceed 0.8wt.%, otherwise, large primary, Al₁₅(FeMn)₃Si₂ particles will form which reduce machinability.¹ Strontium refines and increases the numbers of primary α -iron particles through fragmentation and dissolution of the β -Al₅FeSi platelets. Addition of strontium at low levels neutralizes the positive effect of manganese in reducing the harmful beta-phase. Strontium is normally added at levels of 0.05wt.% or less.^{31,60} Strontium is effective in reducing the size of β - platelets at lower cooling rates. The addition of 0.03% Sr to A413 alloy, in the presence of 1wt.% Mn, aid the fragmentation of the β - phase. The Sr and Mn combined addition, together with higher cooling rate is found to be the most effective method to modify the intermetallic compounds. Figure 2.5 shows the microstructures of the Mn and Sr modified alloys where both the Chinese script and sludge type morphologies are formed in addition to the needle-like β -phase in the Sr-free alloy and the β -phase almost disappears with the addition of Sr.⁶¹

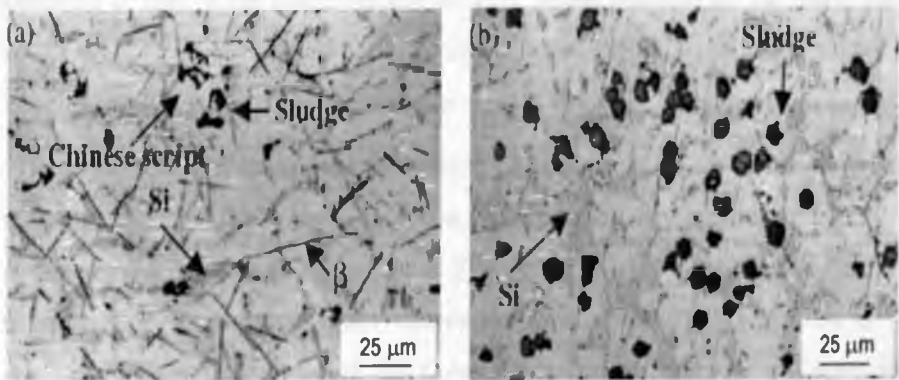


Figure 2.5: Microstructures of two alloys cast into a graphite mold, showing the effect of (a) 0.3wt.% Mn alone and (b) 0.3wt.% Mn combined with 0.015 wt.% Sr.⁶¹

Chromium additions transform β - plates into both Chinese scripts and star-shaped Cr-Fe phases, which are finer in the chill casting than in the sand castings. However, Cr is of limited use because of its tendency to contribute to sludge formation.⁵⁷ It is reported that the best iron-corrector is probably cobalt (Co) and Mo because though chromium and nickel may also correct the iron,

$\text{Al}_{13}(\text{Fe,Cr})_4\text{Si}_4$ or $\text{Al}_2(\text{Fe,Cr})_5\text{Si}_8$ and Al_9FeNi phases may form which are more elongated and thus produce some brittleness.⁶² Mondolfo¹ favors the use of cobalt and manganese as the best iron-correcting elements, because they do not combine with silicon. The Chinese script $\text{Al}_9(\text{Fe,Co})_2$ phase, formed in the alloy is limited as it forms mainly within the aluminum dendrites rather in the inter-dendritic regions.²³ In Al-Si alloys, cobalt may slightly increase the alloy's strength at room temperature and at elevated temperatures, and may also slightly increase ductility, but only if it acts as an iron correctors. However, cobalt reduces the alloys strength, ductility and may increase the alloys fatigue resistance.⁶²

2.7.5 Electromagnetic Filtration

In electromagnetic filtration, the electromagnetic force is exerted on the melt in the separation chamber. Electromagnetic force induced in the aluminum melt scarcely acts on the primary iron-rich phase due to its low electric conductivity, the Fe-intermetallic compounds then moves in a direction opposite to that of the electromagnetic force as the reaction of the force. As a result, the primary iron-rich particles are separated from Al-Si alloy melt and are collected in the separation chamber while the melt is in continuous flow.²⁶

The method of electromagnetic filtration of primary iron-rich phases is highly efficient and amenable for continuous flowing melt in contrast with natural settling and filtration as reported by Zhenming et al.⁵⁴ They found that the iron content in the cast ingot decreases from 1.20wt.% to 0.41wt.% by electromagnetic filtration and the composition of the alloy could meet the demand for casting. Ho et al²⁶ in their experiments found that, when a current of 40A is induced, the iron content at the center of the specimen decreased from 1.64wt.% Fe to 0.45wt.% Fe. It is considered that small particles of angular $\text{Al}_{15}(\text{Fe,Mn})_3\text{Si}_2$ compounds were also eliminated by electromagnetic force. However, as the induced currents and the magnetic field intensity increases, the iron-intermetallic compounds are effectively eliminated at the bottom wall opposite to the electromagnetic force.

2.7.6 Gravity Sedimentation

Sedimentation of primary Fe-rich particles leads to the depletion of the level of iron in solution in the liquid alloy.⁴¹ The sedimentation of primary intermetallic also has a potential to cause the precipitation of oxide films from liquid metal. These methods are practically limited to inclusion sizes greater than 100 μm .⁵⁶ This is because; alumina in liquid aluminum is a stable solid inclusion, and together with its entrained layer of air, is nearly neutrally buoyant, and it is in the form of an extended or convoluted film, greatly increasing its drag and so impeding its separation from the melt.

Although this method has been beneficial to casting properties, the accidental inclusion of large precipitated particles is highly detrimental in castings. In addition, the loss of iron can be a problem in pressure die-castings because of the increased tendency of die-casting to "solder" to the dies. Iron reportedly can be reduced to 0.3wt.% in aluminum held between 620°C and 660°C with about 10% metal loss to sludge. Another method combines Mn additions with holding between 590°C and 660°C to remove Ti, in addition to iron.⁴⁸

CONSTITUTIONAL REFORMS

3.2. Conclusions

As a result of the process, the Commission has identified a number of areas for reform...

CHAPTER 6: CONCLUSIONS AND RECOMMENDATIONS

The Commission has identified a number of areas for reform...

1. The Commission has identified a number of areas for reform...

2. The Commission has identified a number of areas for reform...

3. The Commission has identified a number of areas for reform...

4. The Commission has identified a number of areas for reform...

5. The Commission has identified a number of areas for reform...

CONCLUSIONS AND RECOMENDATIONS

6.1 Conclusions

A number of experiments were carried out to ascertain the effects of iron on solidification, microstructure and mechanical properties of aluminium silicon alloys and the following conclusions can be drawn from the results of the investigation:-

- During solidification of aluminium silicon alloys, presence of iron, manganese and strontium tend to concentrate in ways to influence the solidification behavior and also tend to trigger the nucleation and growth of second phases. Solidification temperature of α -Al dendrite was found to increase from 596°C to 606°C with addition of 0.6wt.% Mn.
- The results show that even slight changes in the concentration of these elements can cause a variation in the reaction temperature and resultant microstructure.
- The results also show that strontium modification tends to raise the precipitation temperature of intermetallics from 577°C to 587°C but it lowers the eutectic temperature of aluminium silicon from 547°C to 540°C.
- Observation of the microstructure revealed a number of intermetallic phases formed as iron content increases. Iron addition in combination with other elements results in the formations of needle β -phases (Al_5FeSi), α -phase ($Al_{15}(Fe,Mn)_3Si_2$) and α - Al_8Fe_2Si phase whose grain size and volume fraction increases with iron concentration.
- Both grain size and volume fraction of intermetallic phases were found to increase from 5.35 μm to 7.25 μm and from 4.2% to 8.6% respectively as the iron content increases from 0.84wt.% to 1.8wt.%.
- Strontium modification at levels of 0.02wt.% tends to reduce the size of intermetallic phases and also refines eutectic silicon.

- Addition of 0.02wt.% Sr and 0.6wt.% Mn combined is found to be more effective in modifying the needle-like β -phase to shorter, more separated ones and changing the morphology to the Chinese script type and more refined silicon particles than addition of Mn or Sr alone.
- A T6 heat treatment cycle tends to fragment the intermetallic phases and spheroidize the silicon phases.
- A combination of strontium modification at a level of 0.02% and heat-treatment at 500°C results in a more coarsened and rounded silicon with further reduction of intermetallic phases.
- Hardness of Al-Si alloy increases as iron content is increased to 1.8wt.% with further increase with addition of 0.9wt.% manganese due to the formation of a hard α -Al₁₅(Fe,Mn)₃Si₂ script.
- However, strontium modification at levels 0.02wt.% and heat-treatment tend to reduce the effects of iron resulting to decrease in hardness.
- The present experimental result reveals that iron addition decreases fatigue, tensile strength and ductility of Al-Si alloys. This detrimental effect of iron on mechanical properties is due to the size and number of iron-containing intermetallics (particularly the brittle β -phase) that increases with iron content. Since these participate directly in the fracture mechanism, the more intermetallics there are, the lower the ductility and the less the number of cycles for the fatigue failure.
- Addition of 0.02wt.% strontium leads to slight improvement of ductility, tensile strength and fatigue due to fragmentation and dissolution of β -platelets.
- Strontium and manganese combined is more effective in reducing the size and number of β -platelets in addition to spheroidization of silicon resulting in improved ductility, tensile strength and fatigue.
- Heat-treatment in our study is also found to slightly reduce the intensity of the negative effects of iron with improved mechanical properties.

6.2 Recommendations

- It was not clear how iron influences the reaction temperatures during solidification and thus a proper design of our mold to accommodate a number of thermocouples would be useful in ascertaining the role of iron in influencing change in reaction temperatures.
- Observation of figure 4.3 shows that increasing manganese does not necessarily result in the alpha phase formation. As evident in figure 4.3(c), some iron constituents still appear as needles. This means that a Mn:Fe ratio of 1:2 given by Gowri et al¹³ is insufficient to prevent the β - plates forming, thus at these slow cooling rates, a ratio closer to 1:1 may be necessary but caution must be taken to avoid sludge formation. However, presence of magnesium seems to influence the formation of various intermetallic phases such as π -phase ($Al_8FeMg_3Si_2$) and further studies on effects of magnesium on aluminium alloys would be of useful.
- Generally, iron is found to have detrimental effects both on microstructure and in mechanical properties of Al-Si alloys and any process that can be employed to raise its permissible concentrations should unequivocally deal with possible reduction in mechanical properties especially fatigue, ductility and tensile strength. This is so because, although strontium and manganese is recommended in reducing detrimental effects of iron, they tend to cause porosities and hard intermetallics in form of sludge respectively at certain levels. Hence alloy development should focus on neutralizer strategies which seem to offer great potential in reducing harmful effects of all concentrations of iron despite their drawbacks.
- As stated earlier, aluminium has found wide application especially in automotive and aerospace industry due to its light weight hence improved fuel efficiency. This research needs to be carried out at high temperatures so as to come up with aluminium engine blocks and cylinder heads with high strength especially during combustion stage since they are normally subjected to temperatures of up to 440°C.

EXPERIMENTAL METHODS

1. Introduction

The purpose of this chapter is to provide a comprehensive overview of the experimental methods used in the study.

CHAPTER 3: EXPERIMENTAL METHODS

The experimental methods used in this study are described in detail in this chapter. The methods are divided into two main sections: the experimental design and the data collection and analysis procedures.

The experimental design section describes the overall structure of the study, including the selection of participants, the assignment of conditions, and the timing of the measurements. The data collection and analysis procedures section describes the specific methods used to collect and analyze the data.

2. Experimental Design

The experimental design is a 2 (Condition) x 2 (Group) design.

The independent variables are:

- Condition (Control and Experimental)
- Group (High and Low)

The dependent variable is the number of correct responses.

3. Participants

The participants in this study were 40 undergraduate students from a large university. They were randomly assigned to one of the two groups (High and Low) and one of the two conditions (Control and Experimental). The participants were paid for their participation in the study.

The participants were screened for any conditions that might affect their performance.

- Participants were screened for any conditions that might affect their performance.
- Participants were screened for any conditions that might affect their performance.
- Participants were screened for any conditions that might affect their performance.

EXPERIMENTAL METHODS

3.1 Introduction

Under this chapter, the design of various experiments conducted to further our understanding on the effects of iron on microstructure and mechanical properties of aluminum silicon alloys is discussed. Various parameters used in the experiments along with the materials used to conduct the experiments are also discussed. It is followed with a step by step description of the procedures used in the experimentation.

Several experimental approaches were simultaneously undertaken to study the effects of iron on microstructure and mechanical properties of aluminum silicon alloys. A multi-pronged approach was necessary in order to arrive at a comprehensive understanding of this complex phenomenon.

The following is a list of experiments conducted during this study:-

- Melting of aluminium silicon locomotive engine pistons into ingots,
- Thermal analysis of unmodified and Sr modified Al-Si alloys,
- Heat-treatment of Al-Si castings,
- Carrying out hardness, tensile and fatigue testing,
- Microstructural analysis of Al-Si castings with addition of Fe, Mn and Sr.

3.2 Design of Experiment

Before designing an experiment, knowledge of the product or process under investigation is of prime importance in identifying the factors likely to influence the outcome. The dependent variables such as alloying, shrinkage porosity and constants like mold design, mold temperature and holding temperature played a major role during the experimental design stage.

The following items and instruments were used during this research work:-

- Approximately 110 kilograms of locomotive aluminum pistons purchased from Kenya Railways Cooperation, iron master alloy filings, fluxing agent, grain refiner, degasser, fifty and five kilograms capacity graphite crucible, strontium modifier and manganese

- Permanent (cast-iron) mould, thermocouples, metallurgical microscope for metallographic analysis, specimen cutter, grinding wheel, abrasive papers, silicon carbide paste and Keller's etchants.
- Hounsfield tensiometer machine, Fatigue Testing - machine, heat-treatment furnace, and macro Vickers hardness tester LV800AT.

3.3 Experimental Procedures

3.3.1 Chemical Analysis

Six identical pistons shown in Figure A1 (Appendix A) each weighing about 19 kilograms purchased from Kenya Railways Cooperation were broken into small pieces to fit the melting crucible and then melted in an oil-fired furnace giving a total of about 110 kilograms of molten metal. Prior to pouring onto steel cups having the shapes of a 5 kilogram crucible, melt treatments such as fluxing, degassing and skimming were carried out. After cooling, the ingots were removed from the cups, and then sample specimens were prepared and taken for chemical/compositional analysis at Booth Extrusions Limited (Thika). Further elemental analysis was also done at the Ministry of Environment and Mineral Resources and an average of all the elements analyzed recorded in Table 3.1.

Table 3.1: Chemical composition of the alloys used in this study

Alloy	Si	Cu	Mg	Fe	Ni	Zn	Sn	Pb	Mn	Ti	Cr	Other	Al
wt %	8.53	1.52	1.21	0.84	1.83	0.49	0.18	0.17	0.14	0.13	0.05	<0.10	>83.5

3.3.2 Mold Design

A permanent mold made of cast iron was used in this experiment as seen in Figure 3.1. The mold was well designed with running system; gating, and risers to facilitate smooth flow of melt into the cavity and to promote sequential solidification of the casting with no defects. During mold design, allowances were also made for taper to facilitate its withdrawal from the mould. Coating of the inner surface of the mould with thin refractory film of graphite was done to facilitate easy removal of the casting, also to reduce the heat transfer and to impart good surface finish.

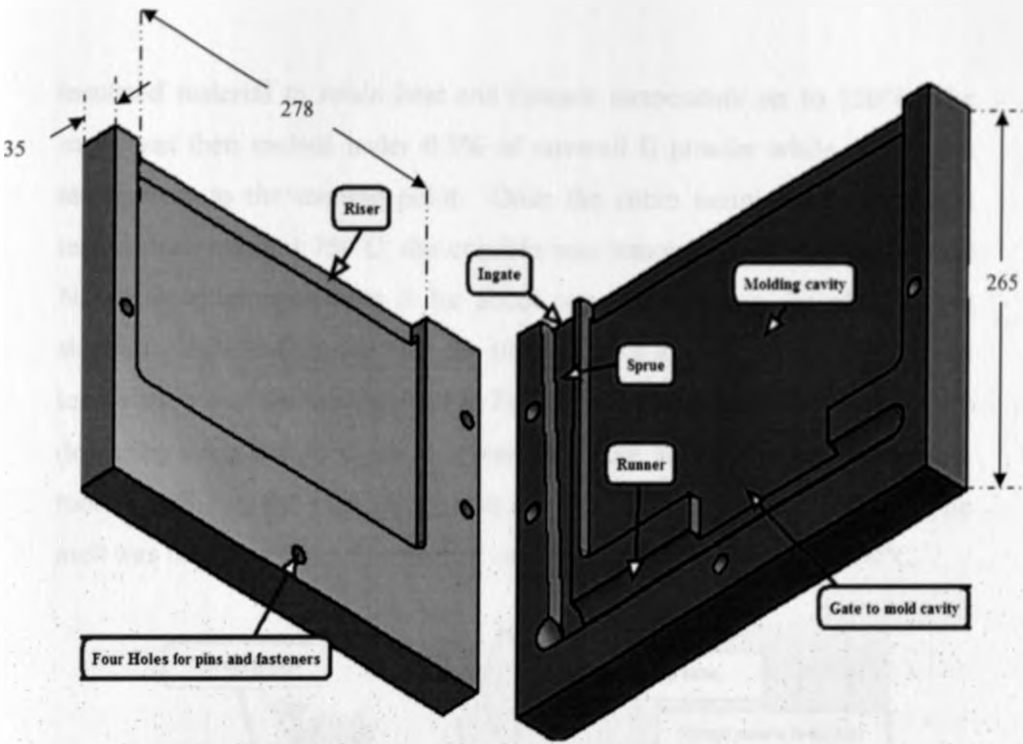


Figure 3.1: Permanent cast-iron mold used for casting

3.3.3 Melt Preparation and Casting

The supplied aluminium ingots were grouped into two and labeled as P0 to P9 for non-heat treated samples and H0 to H5 for heat-treated specimens so as to give an average final chemical composition shown in Table 3.2 upon addition of iron, manganese and strontium. When the iron content exceeds 0.45wt.% as reported by Gowri et al¹³, the iron: manganese ratio should be maintained at 2:1. This therefore forms the basis of choosing 0.6 and 0.9wt.% of manganese respectively.

Table 3.2: Final percentage of iron, Mn and strontium after casting

Samples	P0	P1	P2	P3	P4	P5	P6	P7	P8	P9	H0	H1	H2	H3	H4	H5
% Fe	0.84	1.2	1.5	1.8	1.2	1.8	1.5	1.8	0.84	0.84	1.2	1.8	1.2	1.5	1.8	0.84
% Mn	0.14	0.14	0.14	0.14	0.6	0.9	0.14	0.14	0.14	0.6	0.14	0.14	0.6	0.14	0.14	0.14
% Sr							0.02	0.02	0.02	0.02				0.02	0.02	0.02

The experiment begins with loading the base alloy e.g. P0 into a five kilograms graphite crucible. The crucible was loaded into an electric furnace shown in Figure 3.2. The furnace opening was then closed with an

insulated material to retain heat and furnace temperature set to 750°C. The ingot was then melted under 0.5% of coverall II powder while raising the temperature to the melting point. Once the entire sample has melted and temperature reached 750°C, the crucible was removed from the furnace and Navac tablet plunged onto it for about one minute using the plunger and skimming done before returning the samples back to the furnace. The furnace temperature was then maintained at 730°C for 15 minutes while carrying out degassing using nitrogen gas as shown in Figure 3.2 by means of a ceramic tube dipped into the melt through an opening at the top of the furnace. The melt was then poured to a permanent cast iron mould pre-heated to 450°C.

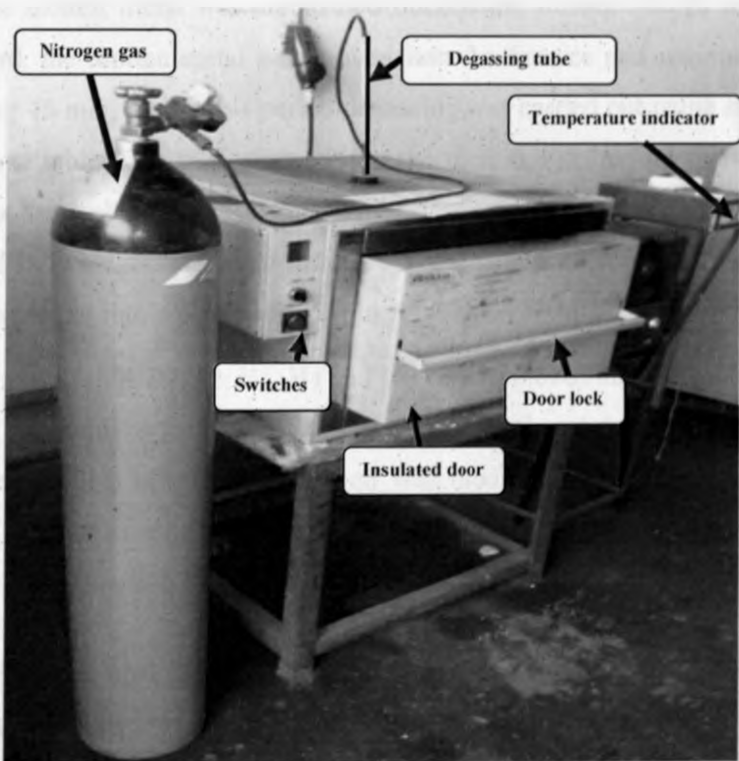


Figure 3.2: Electric Furnace used to melt the alloys under study

In other castings involving the addition of irons for samples P1, P2, P3, H0 and H1, the above procedure though slightly changed was repeated in order to make castings with varying amounts of iron (i.e. 1.2%Fe, 1.5%Fe and 1.8%Fe). During this casting, samples were melted in a five kilogram graphite crucible in an electric furnace under 0.5% of coverall II. After the melt

attained a temperature of 750°C, iron was added and the temperature raised to 850°C and maintained at this temperature for 1½ hours in order to complete dissolution of the intermetallics and homogenize silicon. After a complete dissolution of the compounds, the alloys were maintained at 730°C for 20 min and then skimmed and degassed prior to pouring onto the cast iron mold.

In another experiment where iron and manganese were added to the alloy to give samples P4, P5, P9 and H2, the temperature was maintained at 750°C for 1½ hours to completely dissolve the added iron in the matrix of the molten metal. Molten metal was then brought out from the furnace and manganese added to the molten metal. Likewise, dissolving manganese was carried out when the molten metal was maintained outside the furnace for 10 minutes. Afterward, the molten metal was moved into the furnace and maintained at 730°C for 15 min, and in this period degassing was carried out using nitrogen gas. Navac tablet was then plunged into the melt and skimming carried out. After mechanical stirring, the melt was allowed to dwell for 5 minutes, followed by a degassing stage lasting approximately 10 minutes. Then the melt was poured into a permanent cast iron mold.

Lastly, samples P6, P7, P8, H3, H4 and H5 were achieved through addition of iron and strontium to the base alloy. The above mentioned melting procedures were repeated but in addition, the melt was modified with strontium in the form of short, thin rods then stirred, degassed and left in the furnace for 10 minutes before pouring into the cast iron mold.

3.3.4 Pouring and Measurement of Cooling Rates

The liquid metal was poured into a permanent cast iron mold that was preheated to 450°C and coated with graphite to facilitate easy removal of the casting. In order to determine the possible reactions that could take place during solidification, thermal analysis was carried out simultaneously, using a K-type thermocouple placed at the center of the permanent mold and temperature - time data acquired using temperature data logger machine capable of acquiring data. All samples were allowed to cool and solidify in the permanent mould while their temperatures were monitored by the

thermocouples connected to a data acquisition unit. Once the sample has completely solidified, the casting was removed from the mold and the procedure repeated for subsequent castings. Control of solidification rate was necessary in the casting process in order to improve mechanical properties of an alloy and to minimize the formation of shrinkage cavities, porosity and surface depression.

3.3.5 Heat Treatment

A T6 heat-treatment cycle was employed for H0, H1, H2, H3, H4 and H5 specimens using heat-treatment furnace shown in Figure 3.3. This included solutionizing for 18 hours at 500°C in a forced-air furnace, then quenched in warm water at 70°C for 20 minutes, pre-aged at room temperature for 20 hours and then artificially aged at 170°C for 6 hours.

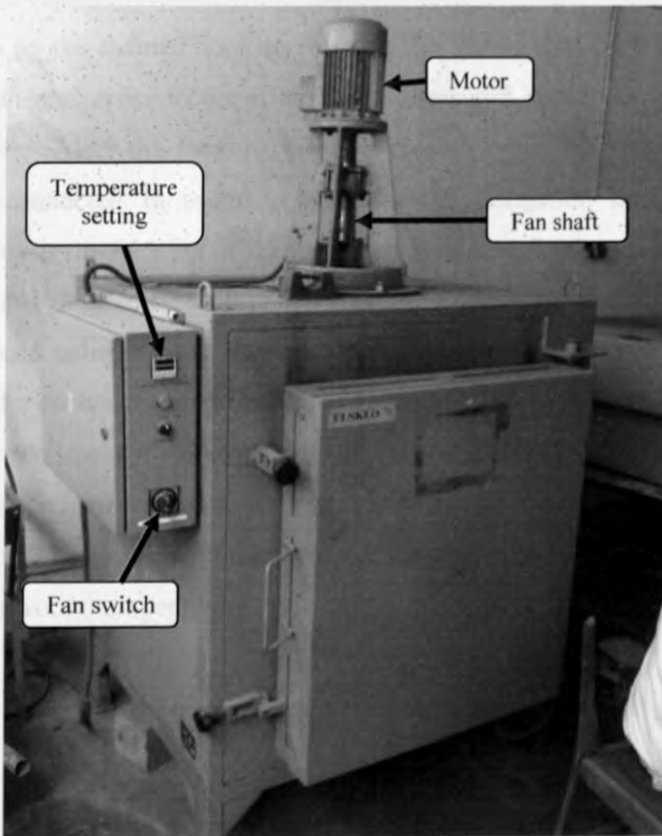


Figure 3.3: Heat Treatment Furnace

3.3.6 Mechanical Testing

Three types of mechanical tests were performed in this study namely; tensile test, fatigue and hardness tests at room temperatures in order to reveal positive or negative effects of intermetallic elements. Hardness and tensile tests were carried out on all alloys including modified and un-modified and heat-treated and non-heat-treated samples. However, nine samples namely, P0, P1, P2, P3, P4, P6, P9, H0 and H5 were tested for fatigue.

3.3.6.1 Tensile test

After casting, five samples for tensile testing were suitably prepared for each alloy according to ASTM 557M standards for tensile tests with diameters of 6.30 ± 0.3 mm and a total length of 38.00 ± 0.2 mm, whereas the gauge length was 25.05 ± 0.5 mm as shown in Figure 3.4. Tensile tests were then carried out on a one-ton capacity Hounsfield tensiometer type W (Figure 3.5) as per the instructions on the manual booklet. Prior to the tensile test, each specimen's gauge length and cross-sectional area was measured and recorded using a caliper device. After the fracture, the two pieces of the test specimen were physically connected in order to measure the elongation and the cross sectional area at the location of fracture. The maximum load to cause fracture was also noted so as to be used to calculate the ultimate tensile stress. Graphs were produced using a hand operated autographic recorder. Five tests were carried out for each sample and values of length elongation, area reduction and ultimate tensile strength tabulated and averaged for each alloy. Some bars were heat-treated before tensile testing so as to compare their resultant tensile properties with unheat-treated samples. All the tensile tests (Figure 3.6) were carried out at room temperature.

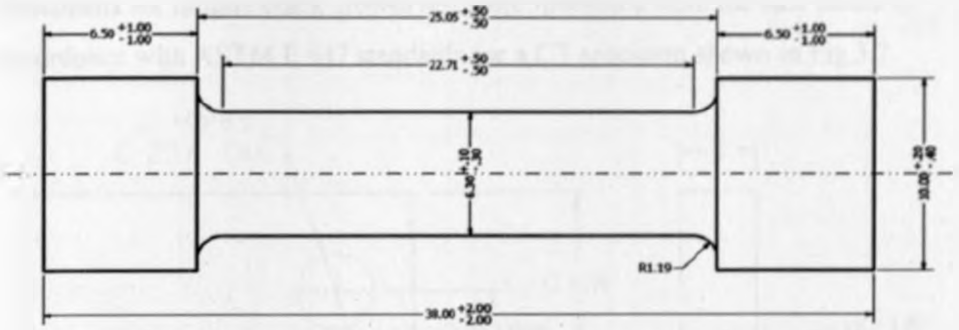


Figure 3.4: Specimens for Tensile test (dimensions in mm)

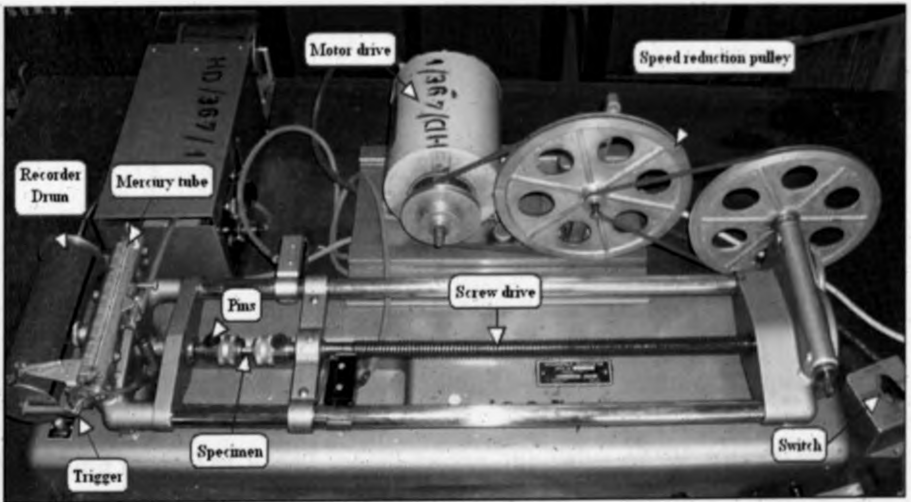


Figure 3.5. Hounsfield Tensiometer type W

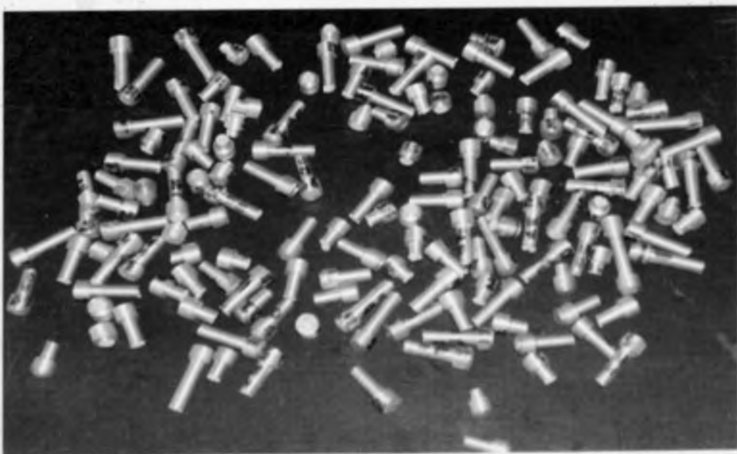


Figure 3.6. Tensile test specimens after testing

3.3.6.2 Fatigue test

Specimens for fatigue crack growth test were machined from the cast plates in accordance with ASTM E 647 standards for a CT specimen shown in Fig 3.7.

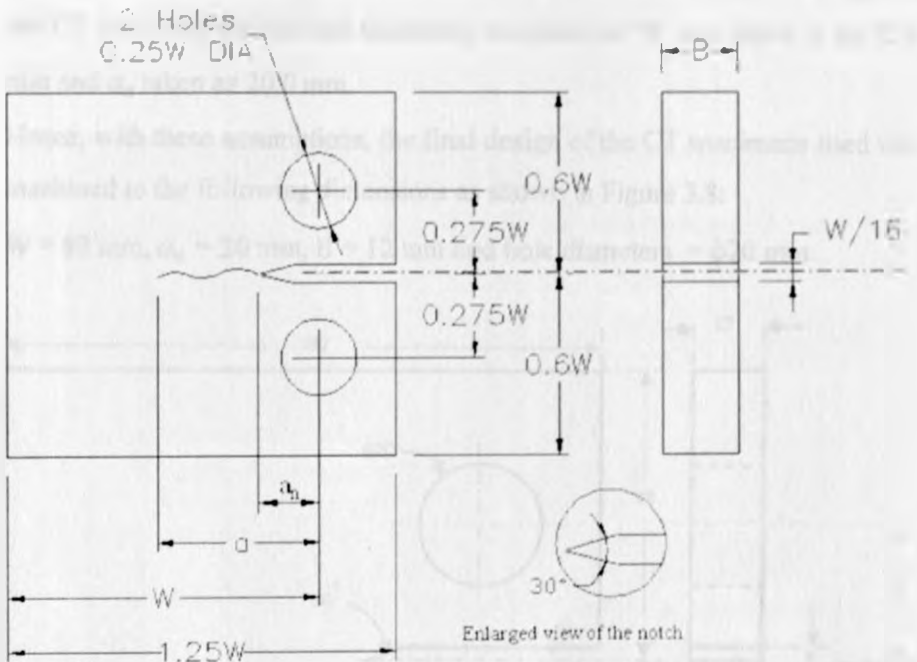


Figure 3.7. Schematic and dimensions of a Compact Tension (CT) specimen

According to ASTM E 647 specifications, the value of 'W' was taken to be 80.0 mm and the recommended thickness, B, of the specimen given by the criterion,

$$\frac{W}{20} \leq B \leq \frac{W}{4} \text{[3.1]}$$

For $W = 80.00$ mm, equation [3.1] becomes; $\frac{80}{20} \leq B \leq \frac{80}{4}$,

$$\therefore \text{Thus } 4 \leq B \leq 20 \text{[3.2]}$$

While the initial crack length a_n is given as,

$$a_n \geq 0.2W \text{[3.3]}$$

$$\text{and for } W = 80 \text{ mm, then } a_n \geq 0.2 \times 80, \therefore \text{Hence, } a_n \geq 16 \text{ mm ----[3.4]}$$

At the beginning, the initial crack length was assumed to be 16.0 mm, but according to ASTM E647 it is required that the machined notch, a_n , in the

C(T) specimen be at least $0.2W$ ($a_n \geq 16$ mm) in length so that the CT specimen will not fail at the two holes instead of at the crack tip. For designing the CT specimen for this test therefore, the value of 'B' was taken to be 12.0 mm and a_n taken as 20.0 mm.

Hence, with these assumptions, the final design of the CT specimens used was machined to the following dimensions as shown in Figure 3.8:

$W = 80$ mm, $a_n = 20$ mm, $B = 12$ mm and hole diameters = $\phi 20$ mm.

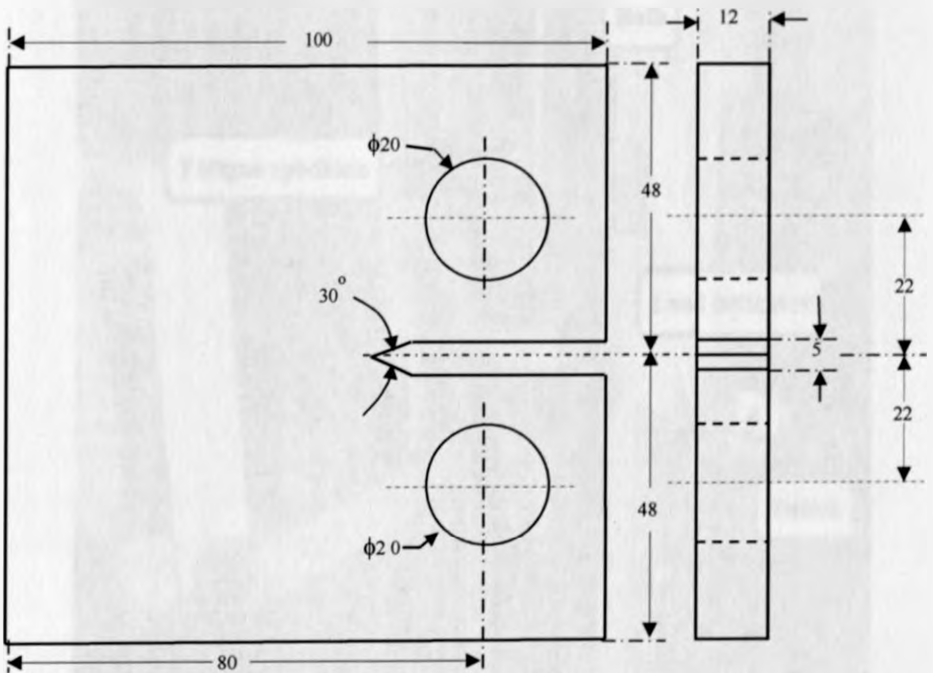


Figure 3.8. Dimensions of a CT specimen used for fatigue test in mm

After polishing the expected crack path, the fatigue test was carried out using a fatigue crack growth test rig (Figure 3.9) at the University of Nairobi, mechanical engineering workshop using a constant load of 650 lbs (2894 Kg-ms^{-2}) at a motor speed of 1502 rpm. The pre-cracked specimen was set between the jaws of the test rig tightly by use of spacers and clevis pins. A load of 650 lbs was then set on the load cell by use of a spanner to tighten the overhead nut followed by tightening the lock nut so that the specimen was only subjected to constant load amplitude.

All materials were tested at room temperature. The crack length a_n observed using a microscope was then recorded at a decreasing load until the specimens completely fail.



Figure 3.9. Fatigue testing machine.

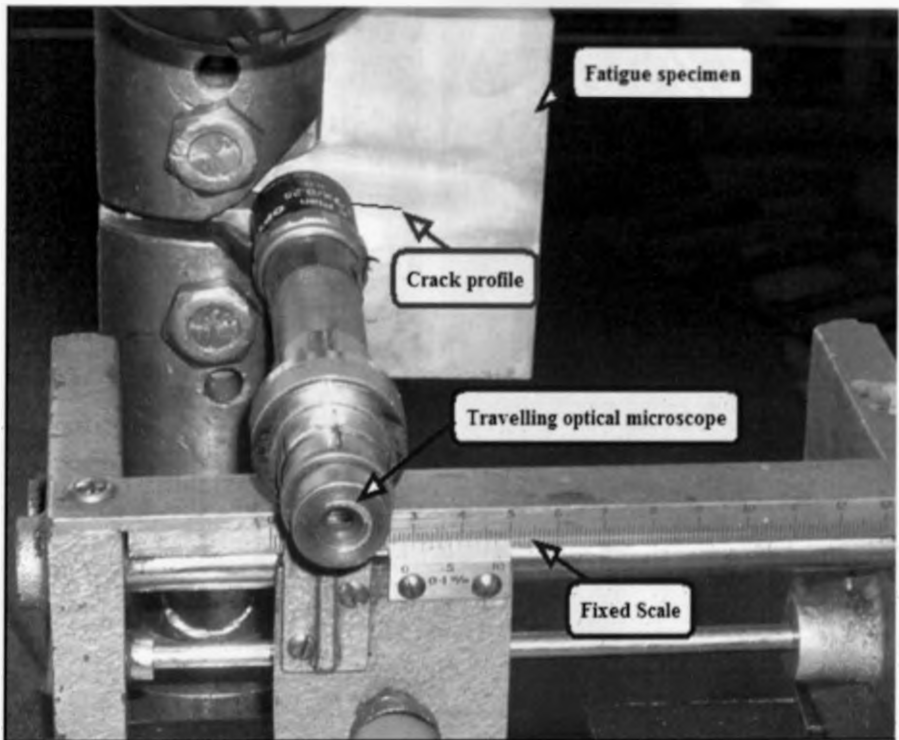
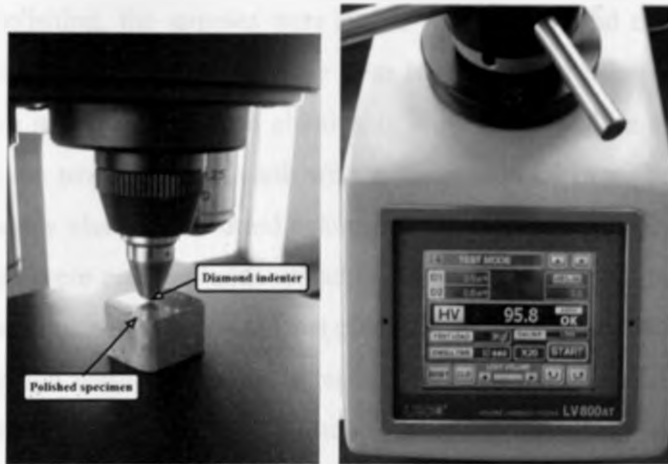


Figure 3.10. Travelling Optical microscope

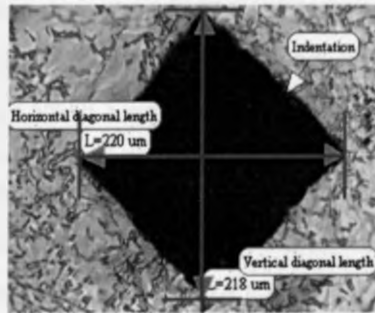
3.3.6.3 Hardness test

Samples for hardness test were sectioned from each alloy containing varying amount of iron, strontium, manganese and from heat-treated samples. All samples were ground using a series of SiC papers with grit numbers 240, 320, 400 and 600. Polishing was performed with a 7 μm and 6 μm diamond paste to a fine finish followed by cleaning and rinsing in clean water before drying. Macro-hardness tests were then carried out at room temperature using a Vickers Hardness Tester LV800AT machine.

During hardness testing, the load was applied gradually to the polished sample without a jerk to a full test load of 3 kgf for 10 seconds. A load of 3 kgf was chosen since it was giving a moderate indentation which was easier to measure. The diagonals of the impression at opposite angles were then measured and the Vickers hardness number obtained directly from the screen as shown in Figure 3.11. Each test was repeated six times and the average value taken as the Vickers hardness number (VHN) for each alloy.



3.11(a). Load of 3 kgf applied 3.11(b). Reading of VHN



3.11(c). Measuring indented diagonals

Figure 3.11. Vickers Hardness Testing using the LV 800AT machine

3.3.7 Metallographic Examination

The samples were first cut from each alloy using a circular saw and well labeled so as not to get mixed up. Each sample was then machined to give flat and parallel surfaces. Test pieces were not mounted in Bakelite resins since the same samples were to be used for the hardness test. Grinding was then performed on each sample using a series of silicon carbide (SiC) grinding papers ranging from 250, 320, 400, 600 and 1200 grit. During grinding, warm tap water was used since it does not seem to have any bearing on the final polish.

Before moving to next smaller grit of SiC, each sample was thoroughly rinsed to remove any residual which might be reallocated to that next grit. Liquid washing soap was used to dress the higher grit SiC papers when smearing occurred.

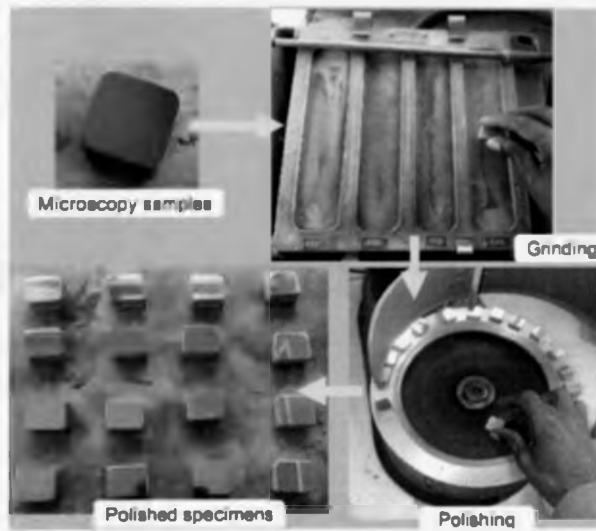
Prior to polishing, the samples were rinsed with ethanol and cleaned using serviette tissue papers. Samples were then hand polished using a polishing cloth with a suspension of 7 μ m alumina in a solution of white spirit before moving to the next polishing cloth with a suspension of 1 μ m. Each sample was thoroughly cleaned and dried before moving to the next polishing cloth. The samples were polished until scratches appear as uniform as possible and then thoroughly cleaned in ethanol and placed in a drier for several minutes.

After thorough washing and drying, each sample was immersed into a fresh Keller's etchant for 10 seconds. This was followed by rinsing in water to wash away any residual of etchant. Finally, the specimens were dipped in methanol to prevent staining before drying. Etchant used contained 95% distilled water, 2.5% Nitric acid, 1.5% Hydrochloric acid and 1% of Hydrofluoric acid (95% H_2O , 2.5% NHO_3 , 1.5% HCl , and 1.0% HF).

After preparing samples for metallographic examination and image analysis, examination of the microstructure for all samples was carried out using the microscope connected to the Leco LV800AT hardness testing machine (Figure 3.12) with an eye piece magnification of $\times 10$. The machine was fitted with an Optika digital camera which was connected to a computer and all micrographs taken in full color. Polarized light was used in cases where it was advantageous.

These color digital micrographs portrayed a more accurate representation of the true microstructure. Even without polarized light microstructural features of aluminium alloys such as different phases, develop specific colorations after being etched. The iron-intermetallic phases were therefore identified from their morphology and colour.

Morphology and identification of intermetallic compound were investigated and measured using image analysis so as to calculate the particle average size (μ m) and volume fraction/percentage (%) of intermetallics. The average grain size and volume fraction was automatically processed using microstructure characterizer software 3.0 (MIC 3.0).



Metallographic preparation

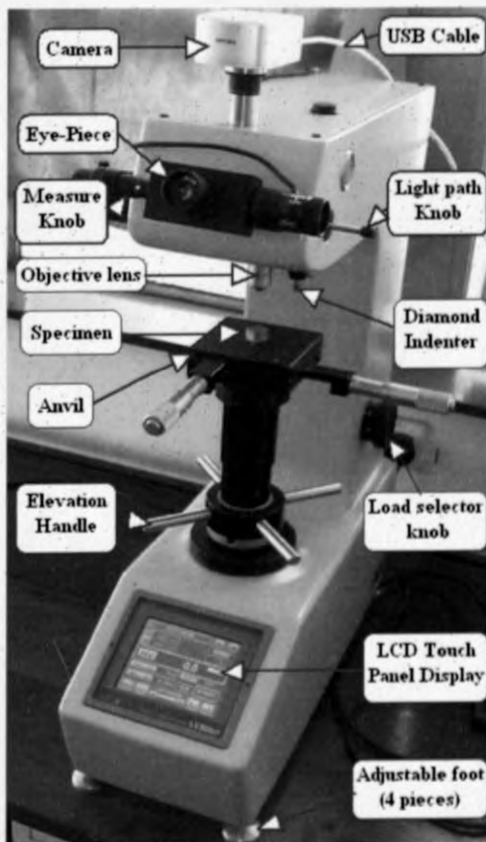


Figure 3.1. Metallographic preparation and examination using a microscope and camera connected to Leco LV800AT Hardness testing machine

EXPERIMENTAL RESULTS

4.1 Introduction

The objective of the results section is to present a clear and concise summary of the experimental results, which are presented in a logical and systematic manner. The results are presented in a clear and concise manner, and the conclusions are drawn from the results.

CHAPTER 4: EXPERIMENTAL RESULTS

4.2. Results Overview

Using the statistical analysis data presented in Table A1, respectively, the following statistical analysis is shown in Figure 4.1, using statistical software.

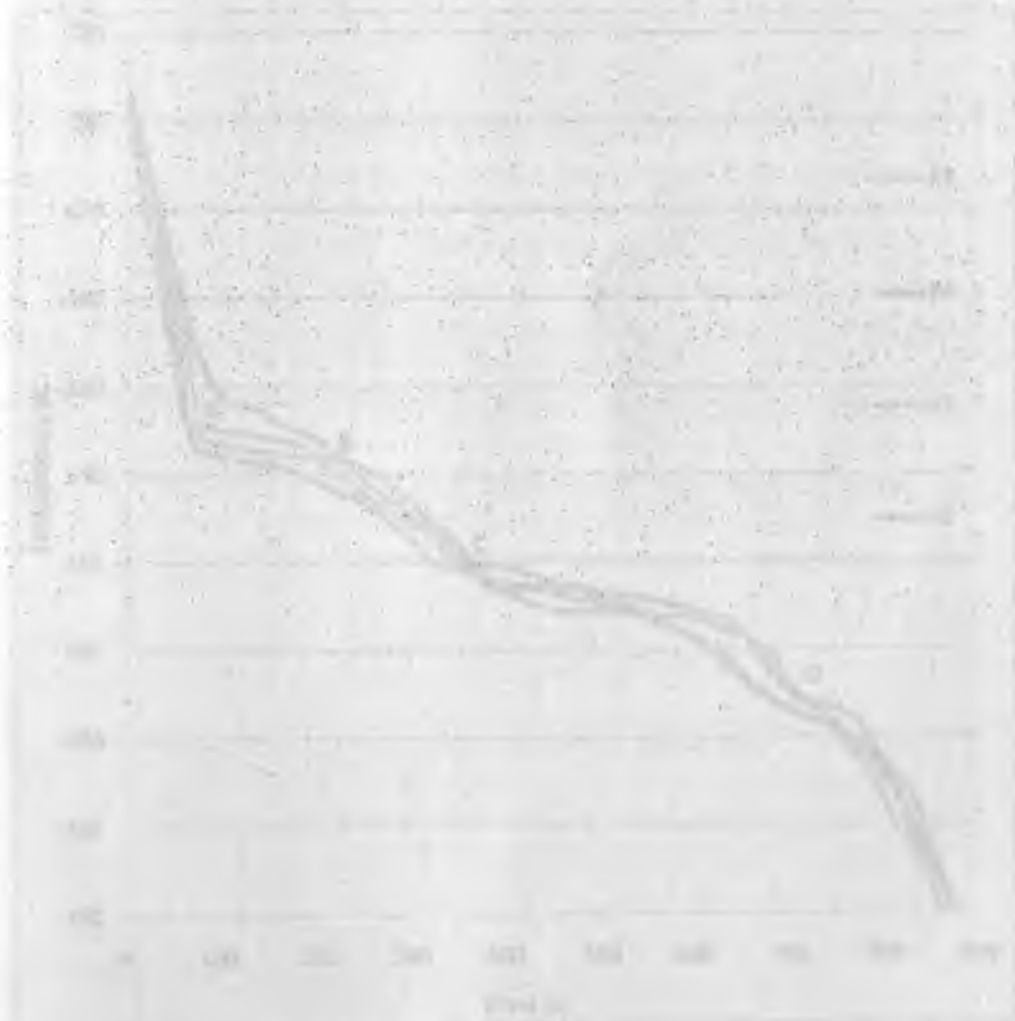


Figure 4.1) Chilling capacity (kW) over time (min) for P1, P2, P3 and P4

EXPERIMENTAL RESULTS

4.1 Introduction

The structure of the results section is based around three experiments which were carried out namely cooling rates taken during the solidification of the casting, microstructural analysis and testing of mechanical properties.

4.2 Cooling Curves

Using the thermal analysis data recorded in Table A1, (appendix A), the cooling curves were plotted as shown in Figure 4.1 using excel software.

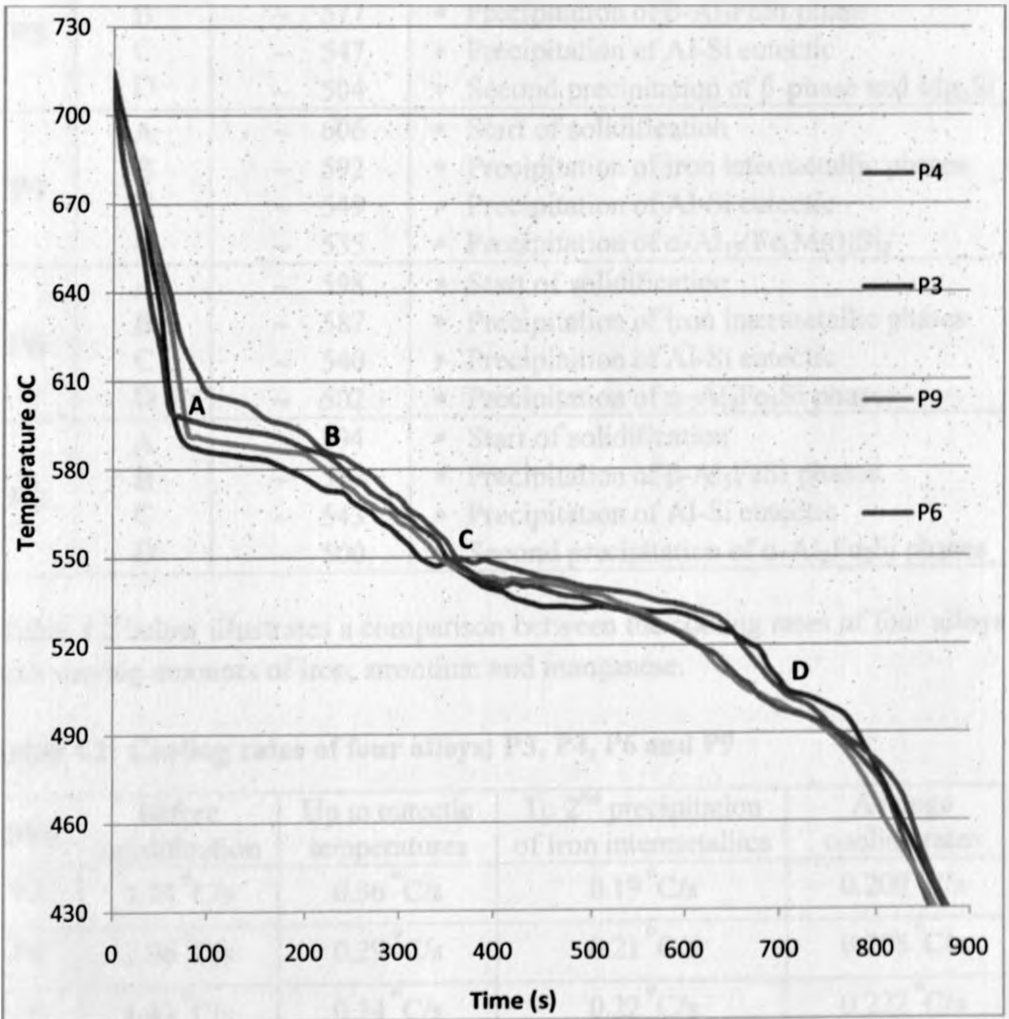


Figure 4.1: Cooling curves for four alloys P3, P4, P6 and P9

From the cooling curves of Figure 4.1, the precipitation temperatures of various phases were obtained and tabulated in Table 4.1. The temperatures noted in Table 4.1 correspond to the peaks observed whereby the liquidus temperature displays the sharp peaks while the other peaks represents the range over which the phase formation and/or its transformation takes place.

Table 4.1: Precipitation temperatures of various phases for alloys

Alloy	Peak (Fig 4.1)	Temperature (°C)	Reaction
P3	A	~ 596	* Start of solidification
	B	~ 577	* Precipitation of β -Al ₅ FeSi phase
	C	~ 547	* Precipitation of Al-Si eutectic
	D	~ 504	* Second precipitation of β -phase and Mg ₂ Si
P4	A	~ 606	* Start of solidification
	B	~ 592	* Precipitation of iron intermetallic phases
	C	~ 549	* Precipitation of Al-Si eutectic
	D	~ 535	* Precipitation of α -Al ₁₃ (Fe,Mn) ₃ Si ₂
P6	A	~ 598	* Start of solidification
	B	~ 587	* Precipitation of iron intermetallic phases
	C	~ 540	* Precipitation of Al-Si eutectic
	D	~ 502	* Precipitation of α -Al ₈ Fe ₂ Si phases
P9	A	~ 594	* Start of solidification
	B	~ 587	* Precipitation of β -Al ₅ FeSi phases
	C	~ 543	* Precipitation of Al-Si eutectic
	D	~ 500	* Second precipitation of α -Al ₈ Fe ₂ Si phases

Table 4.2 below illustrates a comparison between the cooling rates of four alloys with varying amounts of iron, strontium and manganese.

Table 4.2: Cooling rates of four alloys; P3, P4, P6 and P9

Alloy	Before solidification	Up to eutectic temperatures	To 2 nd precipitation of iron intermetallics	Average cooling rates
P3	1.74 °C/s	0.36 °C/s	0.19 °C/s	0.200 °C/s
P4	1.66 °C/s	0.29 °C/s	0.21 °C/s	0.208 °C/s
P6	1.43 °C/s	0.34 °C/s	0.22 °C/s	0.222 °C/s
P9	1.12 °C/s	0.33 °C/s	0.25 °C/s	0.231 °C/s

Recording of cooling rates for all the alloys were carried out for a period of 15 minutes (900 seconds) on each alloy using a thermocouple mounted to the permanent cast iron mold. Examination of Figure 4.1, Table 4.1 and Table 4.2 reveals some differences in the solidification of the unmodified alloy P3, manganese added alloy P4, strontium-modified alloys P6 and P9. While there are some minor differences in the primary aluminium reaction in which precipitation of α -Al dendrite network takes place, the most significant differences between all alloys occur during the aluminium-silicon eutectic reaction. In the unmodified alloy P3 and P4, the eutectic reaction occurs at a high temperature of about 547°C and 549°C respectively with a small degree of recalescence, the temperature stabilizes during growth and the eutectic plateau is relatively isothermal.

The strontium-modified alloy P6 has the lowest nucleation temperature of the four alloys, as observed, there is significant recalescence after nucleation and the isothermal region of the growth plateau occurs over a short interval at an intermediate temperature. The Mn and Sr added alloy P9 has a nucleation temperature between that of the unmodified and strontium-modified alloys and it displays little recalescence.

4.3 Microstructures

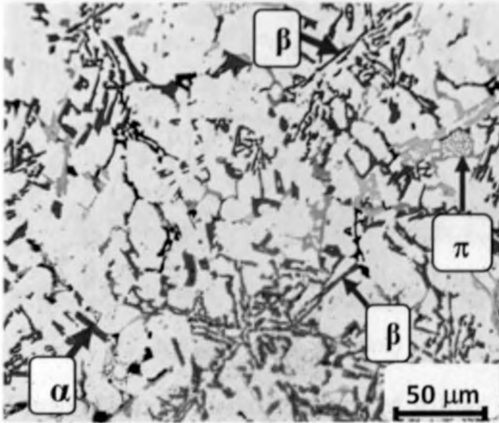
In this section, micrographs for all the samples with addition of iron, manganese and modified with strontium both for heat – treated and non – heat treated are presented. After preparing samples using standard microstructural procedures described earlier under methodology, microstructural analysis was done using the microscope attached to Leco LV800AT hardness tester. All observations of microstructure were carried out using magnifications of 200× and 500×.

Presentations of microstructures are divided into five categories namely:

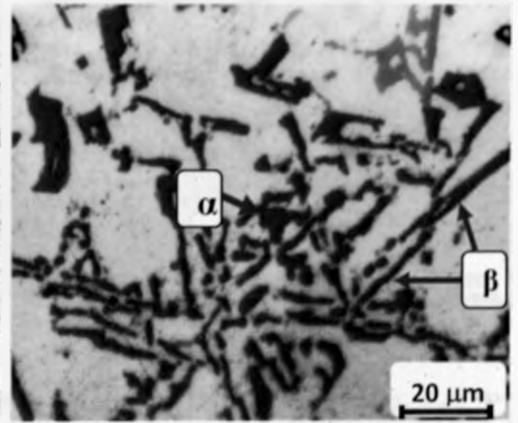
- Effects of iron addition,
- Effects of Mn addition,
- Effects of strontium and manganese combined addition.
- Effects of strontium addition,
- Effects of heat - treatment,

4.3.1 Effect of Iron addition on Microstructure

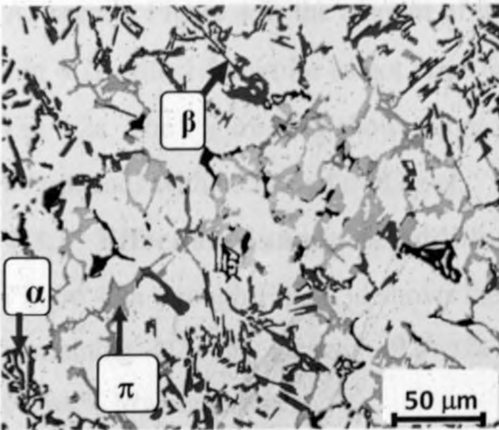
Alloys P0, P1, P2 and P3 are shown in Figures 4.2a through Figure 4.2h.



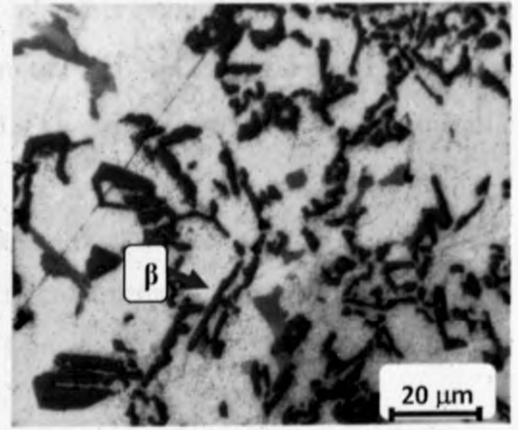
(4.2a) alloy P0, (200×)



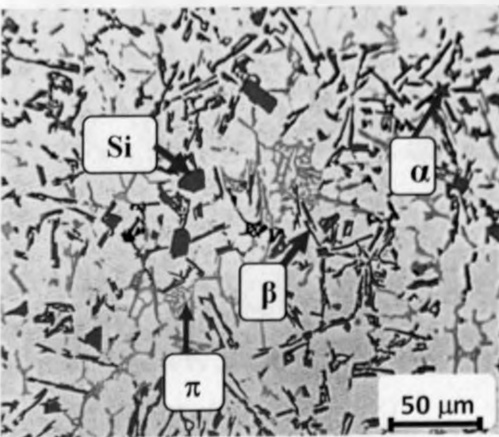
(4.2b) alloy P0, (500×)



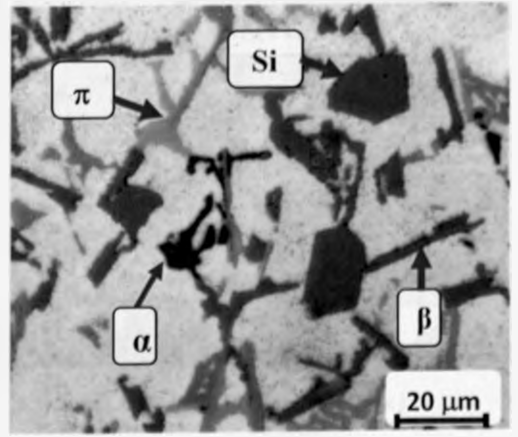
(4.2c) alloy P1, (200×)



(4.2d) alloy P1, (500×)



(4.2e) alloy P2, (200×)



(4.2f) alloy P2, (500×)

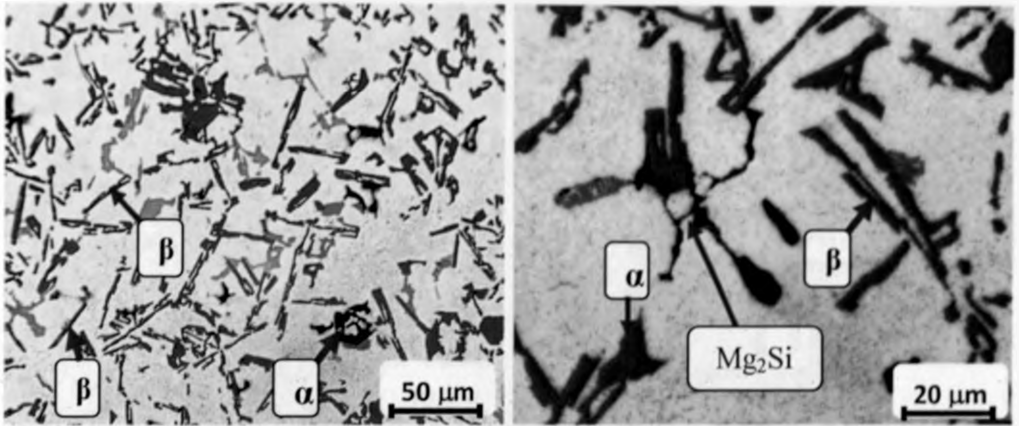
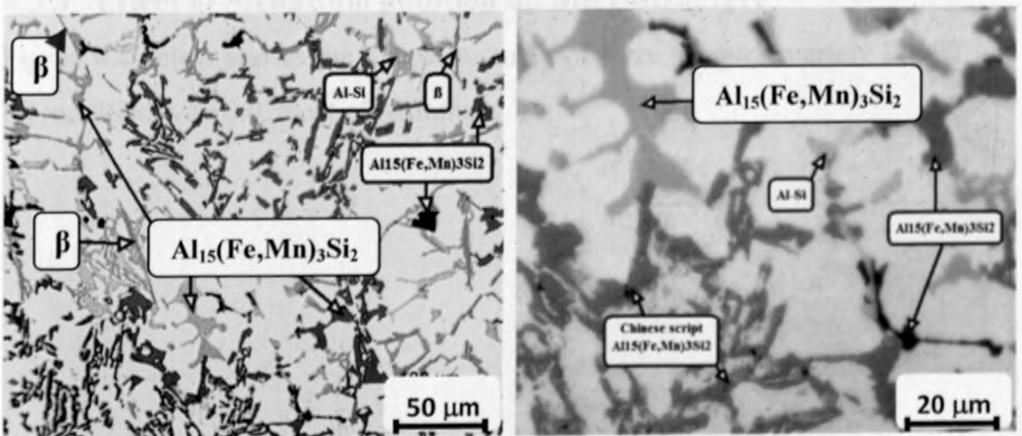
(4.2g) alloy P3, (200 \times)(4.2h) alloy P3, (500 \times)

Figure 4.2: Microstructure of alloys P0 (0.84wt.% Fe), P1 (1.2wt.% Fe), P2 (1.5wt.% Fe) and P3 containing 1.8wt.% Fe. Magnifications 200 \times and 500 \times .

As seen in Figure 4.2, the amount of β - platelets increases with increase in iron. Fig 4.2g with 1.8%wt Fe as got large amount of β - phases compared to those of Fig 4.2a. The Figure also shows more β - phases in form of needle-like metallic compounds with increased iron level.

4.3.2 Effect of Manganese addition on Microstructure

Figure 4.3a through Fig. 4.3d shows the microstructure of two samples P4 and P5 containing 1.2wt.% Fe with 0.6wt.% Mn, and 1.8wt.% Fe with addition of 0.9wt.% Mn respectively.

(4.3a) alloy P4, (200 \times)(4.3b) alloy P4, (500 \times)

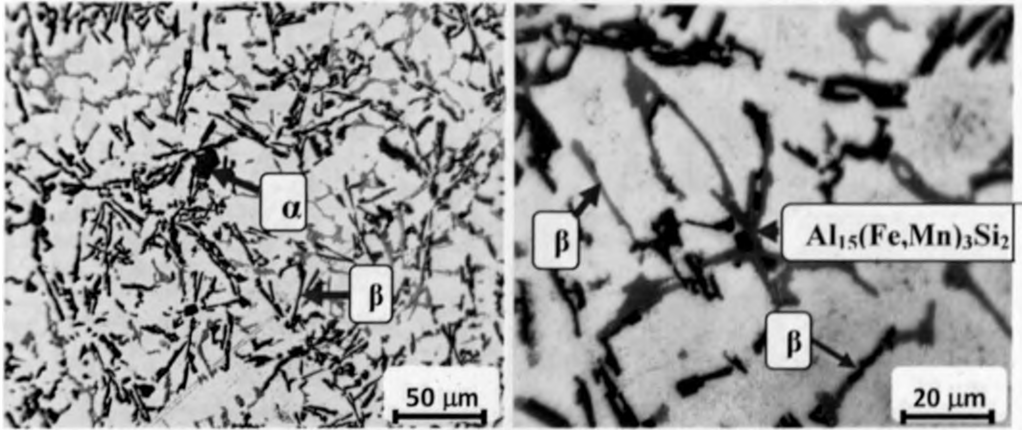
(4.3c) alloy P5, (200 \times)(4.3d) alloy P5, (500 \times)

Figure 4.3: Microstructure of alloys P4 (1.2wt.% Fe, 0.6wt.% Mn) and P5 containing 1.8wt.% Fe, 0.9wt.% Mn under magnifications of 200 \times and 500 \times .

The microstructure of alloys P4 and P5 basically comprises of aluminium dendrites, eutectic silicon and iron-rich intermetallic particles. Some iron-rich intermetallics observed in Figure 4.3 occur as dendritic phase while those of Figure 4.2 are in form of needle-like phase. There are two types of iron-bearing intermetallics observed in Fig. 4.3 namely: β -phase (Al_3FeSi), and α -phase ($\text{Al}_{15}(\text{Mn}, \text{Fe})_3\text{Si}_2$). Some β -phases forms as thin plates as seen in Fig. 4.3a while in Fig. 4.3c are in form of rods or branched structure.

4.3.3 Effect of Strontium addition on Microstructure

Figure 4.4 below shows the microstructures of three samples namely P6, P7 and P8 modified with 0.02%wt of strontium.

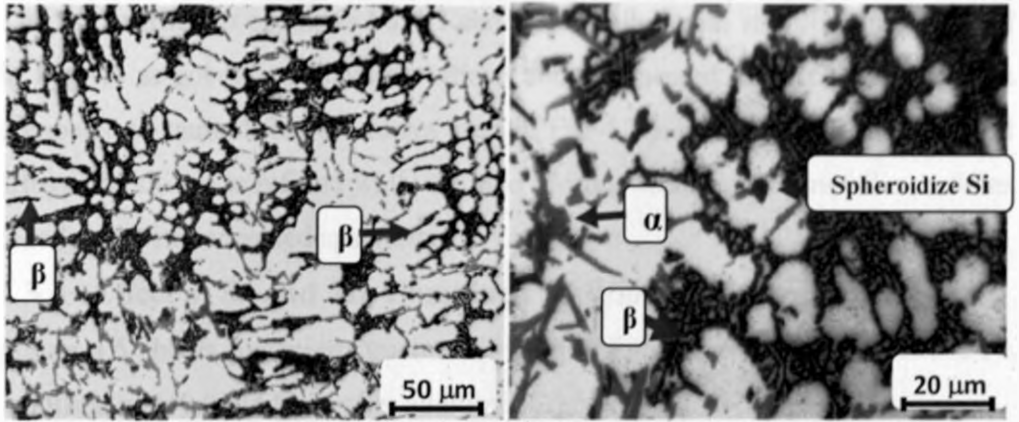
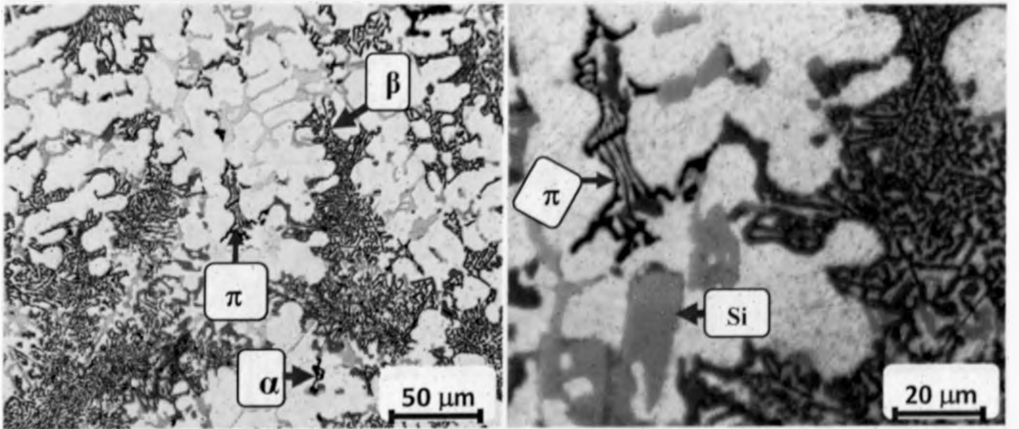
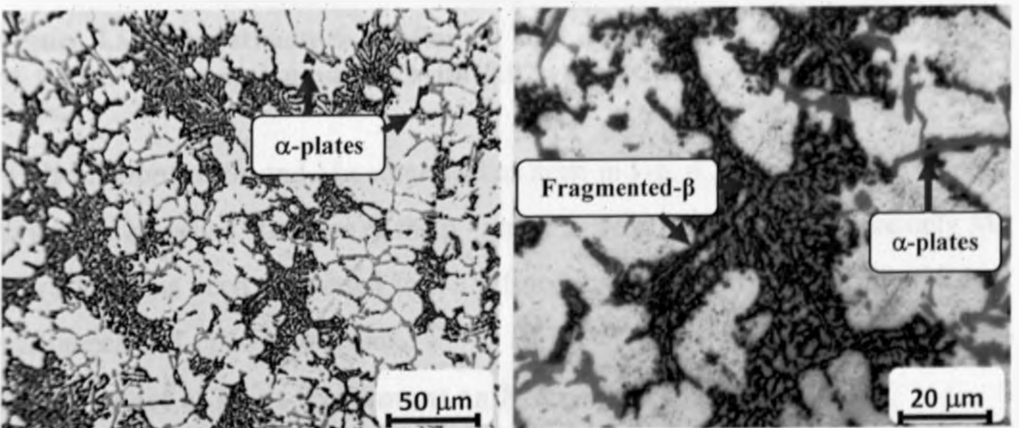
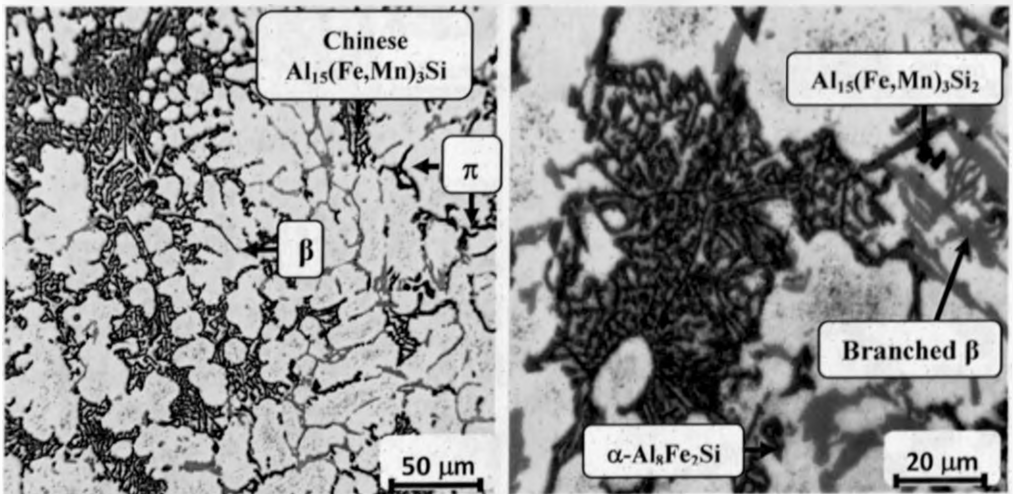
(4.4a) alloy P6, (200 \times)(4.4b) alloy P6, (500 \times)(4.4c) alloy P7, (200 \times)(4.4d) alloy P7, (500 \times)(4.4e) alloy P8, (200 \times)(4.4f) alloy P8, (500 \times)

Figure 4.4: Microstructure of alloys P6 (1.5wt.% Fe), P7 (1.8wt.% Fe) and P8 (0.84wt.% Fe) modified with 0.02wt.% Sr. Magnifications 200 \times and 500 \times .

The microstructure of alloys P6, P7 and P8 modified with strontium as observed in Fig 4.4 as got refined eutectic silicon and fragmented intermetallic phases as compared to unmodified structures seen in Fig 4.2 and Fig 4.3. In this modified alloys, the silicon is refined while the size of iron – bearing intermetallic particles is reduced with increased sphericity.

4.3.4 Effect of Sr and Mn Combined additions on Microstructure

Figure 4.5 shows the microstructure of sample P9 a base alloy of 0.84wt.% Fe modified with 0.02wt.% Sr after addition of 0.6wt.% Mn.



(4.5a) alloy P9, (200×)

(4.5b) alloy P9, (500×)

Figure 4.5: Microstructure of alloy P9 containing 0.84wt.% Fe with addition of 0.6wt.% Mn and modified with 0.02wt.% Sr. Magnifications 200× and 500×.

With additions of Sr and Mn combined as seen in Fig. 4.5, the flake-like eutectic Si and the branched structure of the β - phase as seen in Figure 4.3 where only Mn was added has been converted into a refined and modified eutectic Si with less and branched β - phase structure.

4.3.5 Effect of Heat-Treatment on Microstructure

Six samples named as H0, H1, H2, H3, H4 and H5 with varying percentages of iron, manganese and strontium were heat-treated and their micrographs presented in Figures 4.6 through Figures 4.8.

4.3.5.1 Effect of Iron additions and Heat Treatment on Microstructure

Figure 4.6 show microstructures of heat-treated samples of H0 and H1.

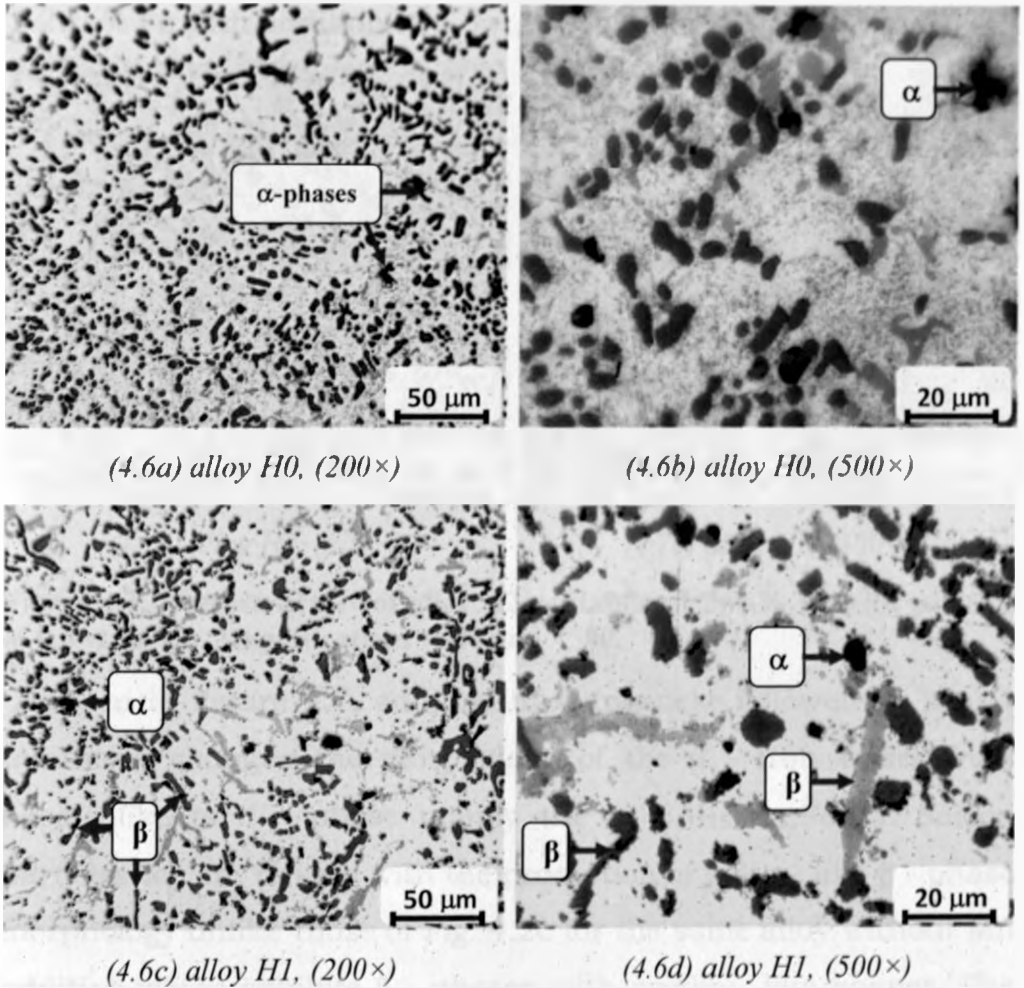
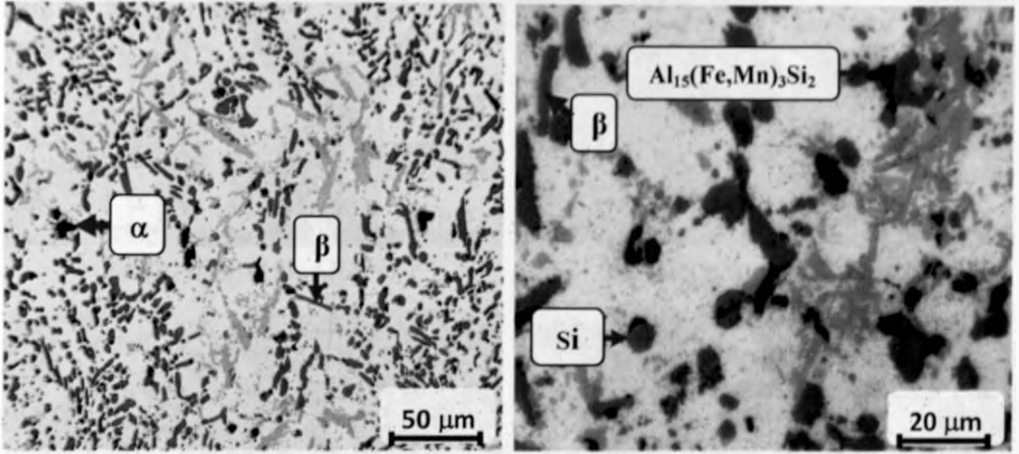


Figure 4.6: Microstructure of alloys H0 and H1 with additions of 1.2wt.% Fe and 1.8wt.% Fe respectively. Magnifications of 200× and 500×.

The microstructure of the fully heat-treated T6 condition as shown in Figure 4.6 consists of aluminium cells bounded by irregularly shaped silicon particles and some iron-bearing compounds of fine dendritic α -phase. Here, the edges of silicon particles are not as flaky as observed in alloys of Figure 4.2 that was not heat-treated.

4.3.5.2 Effect of Manganese additions and Heat-Treat on Microstructure

Figure 4.7 shows the micrograph of sample H2 containing 1.2wt.% Fe with addition of 0.6wt.%.



(4.7a) alloy H2, (200×)

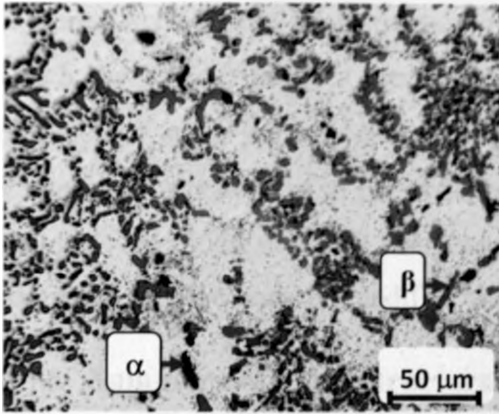
(4.7b) alloy H2, (500×)

Figure 4.7: Microstructure of alloy H2 containing 1.2wt.% Fe with addition of 0.6wt.% Mn. Magnifications ×200 and ×500.

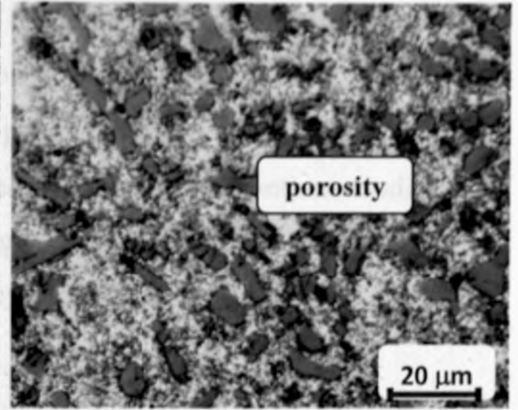
As seen in Figure 4.7, addition of manganese followed by heat treatment changes the morphology of the β - iron phase from needle like to α - phase mainly the α - Al₁₅(Mn,Fe)₃Si. Silicon particles too are refined with the promotion of plate - like β - phase morphology unlike those of Fig. 4.2c for the same alloy without Mn addition which exhibits β - phases with needle - like shapes. The amount and size of beta - phases are also reduced in Fig 4.7 compared to those of Fig 4.3a for the same alloy with addition of Mn without heat treatment.

4.3.5.3 Effect of Strontium addition and Heat Treatment on Microstructure

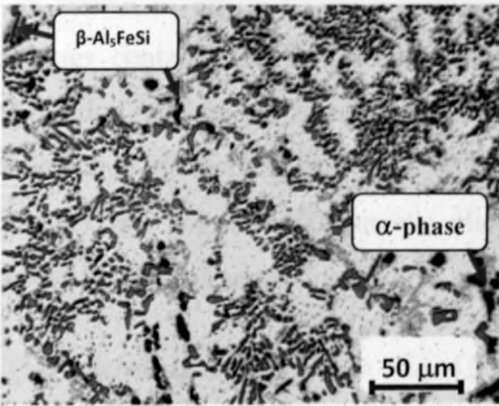
The Figures 4.8a through 4.8f below shows three alloys H3, H4 and H5 modified with strontium then heat-treated.



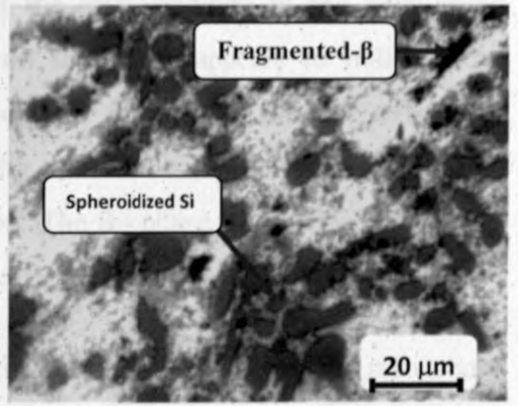
(4.8a) alloy H3, (200×)



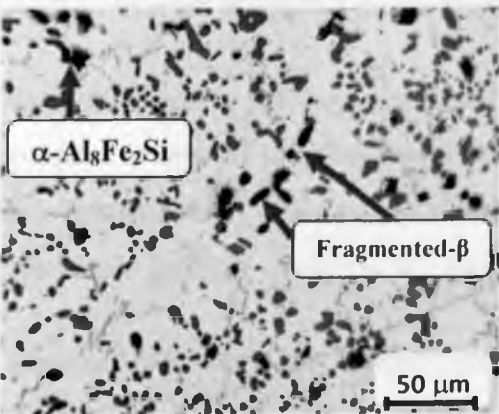
(4.8b) alloy H3, (500×)



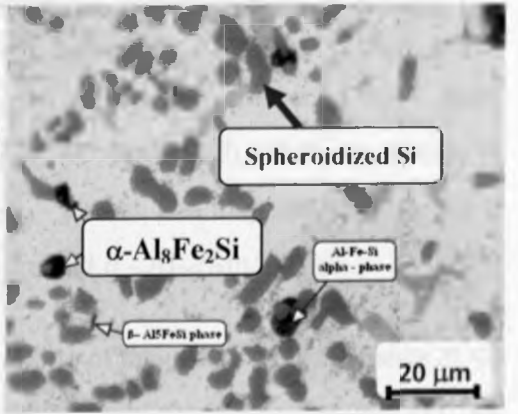
(4.8c) alloy H4, (200×)



(4.8d) alloy H4, (500×)



(4.8e) alloy H5, (200×)



(4.8f) alloy H5, (500×)

Figure 4.8: Microstructure of alloys H3, H4 and H5 with 1.5wt.% Fe, 1.8wt.% Fe and 0.84wt.% Fe respectively modified with 0.02wt.% Sr. Magnifications 200× and 500×.

Figure 4.8 shows the microstructure of three alloys modified with strontium in which the silicon particles are seen to have been spheroidized though with presence of some porosity. Some β - phases are seen intact while some are fragmented. As observed in Fig. 4.8e, heat-treatment and strontium modification changed the microstructure morphology from plate-shaped to star-like as compared with the same un-modified alloy observed in Fig. 4.2a.

4.3.6 Summary of Microstructural Results

As shown in Fig. 4.2, the majority of the microstructure in the unmodified castings contains coarse plate-like silicon that often appears to radiate from polyhedral silicon particles. Some regions of the casting contain a bimodal distribution of silicon in which the typically coarse silicon plates are accompanied by finer, but still plate-like eutectic silicon. The β - phase is also observed in un-modified samples appearing in form of needle-like shape.

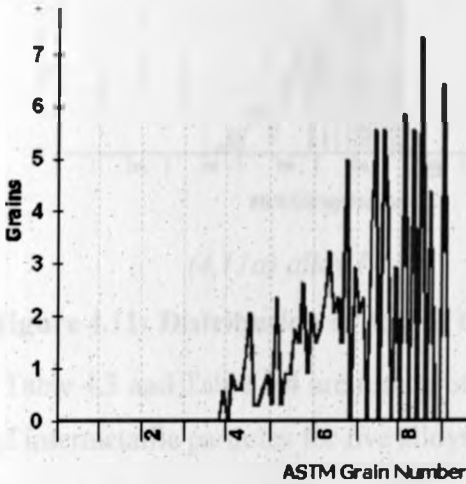
The microstructures seen in Fig 4.3 for alloys with addition of manganese exhibits α - phases in form of dendrites with less β -phases while for the modified samples observed in Fig. 4.4 shows fibrous silicon with fragmented β -phases.

With the addition of both strontium and manganese combined with heat-treatment as seen in microstructures of Fig. 4.5 through Fig. 4.8, the silicon is fully spheroidized while most of the β - phases are fragmented with some transformed to alpha - phases of α - $\text{Al}_8\text{Si}_2\text{Fe}$ and α - $\text{Al}_{15}(\text{Mn}, \text{Fe})_3\text{Si}_2$.

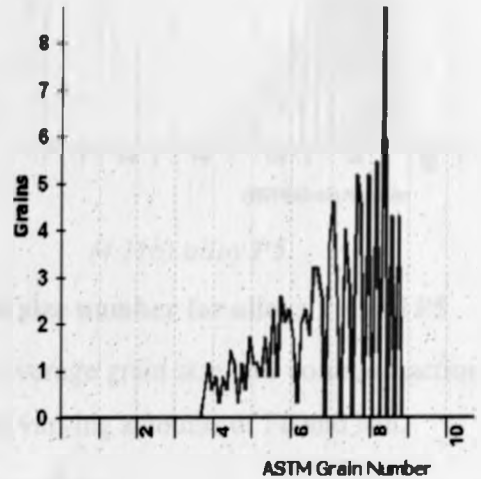
The results also show that although iron is one of the principal constituents at an iron level of 1.8wt.% with 0.9wt.% of manganese, the microstructure did not reveal formation of sludge but merely some intermetallic phases.

4.3.7 ASTM Grain Size Number and Volume Fraction Measurement

The results of the average grain size of particles measured using an automated microstructure characterizer is given in Figure 4.9 through Figure 4.11.

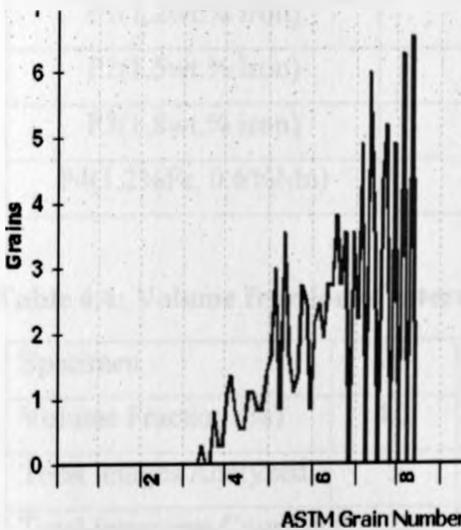


(4.9a) alloy P0

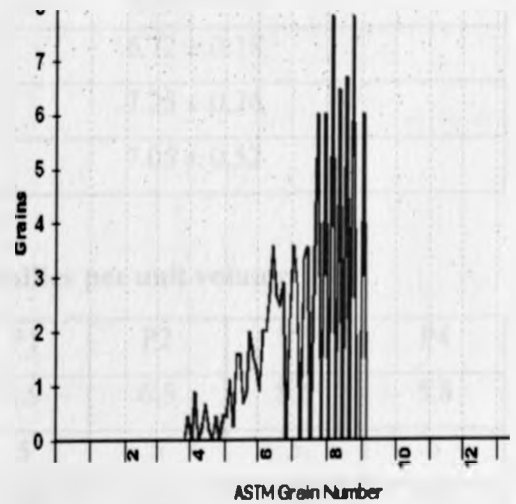


(4.9b) alloy P1

Figure 4.9: Distribution of ASTM Grain size number for alloys P0 and P1



(4.10a) alloy P2



(4.10b) alloy P3

Figure 4.10: Distribution of ASTM Grain size number for alloys P2 and P3

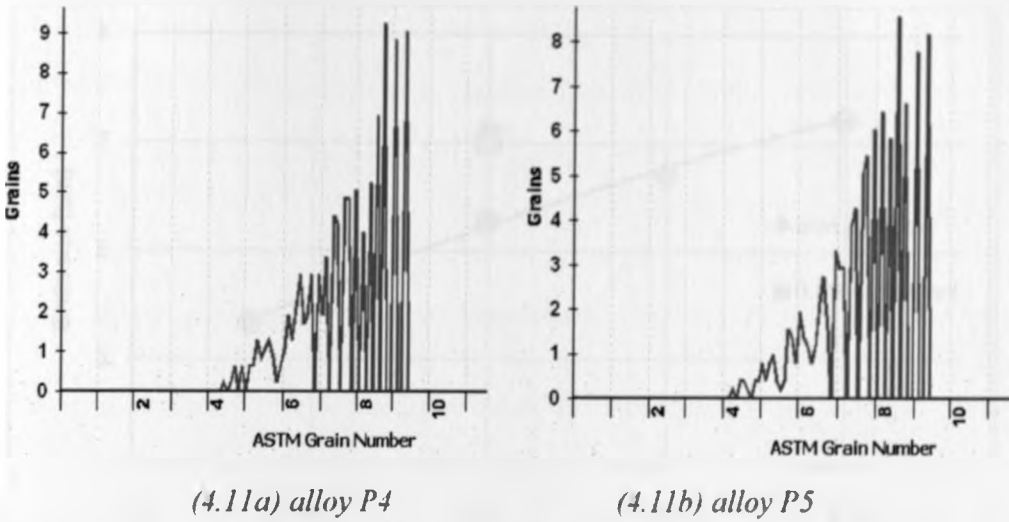


Figure 4.11: Distribution of ASTM Grain size number for alloys P4 and P5

Table 4.3 and Table 4.4 are results of the average grain size and volume fraction of intermetallic particles for five alloys with varying amounts of Fe and Mn.

Table 4.3: Average ASTM Grain size of particles

Alloy	Average ASTM Grain size number (μm)
P0 (0.84wt.% iron)	5.35 ± 0.44
P1 (1.2wt.% iron)	6.29 ± 0.20
P2 (1.5wt.% iron)	6.72 ± 0.18
P3 (1.8wt.% iron)	7.25 ± 0.26
P4 (1.2%Fe, 0.6%Mn)	7.05 ± 0.52

Table 4.4: Volume fraction of intermetallics per unit volume

Specimen	P0	P1	P2	P3	P4
Volume Fraction (%)	4.2	4.9	6.5	8.6	5.8
Total Images Analyzed	5	5	5	5	5
Total Intercepts Counted	122	121	125	124	125
Percentage Error	3.58%	6.51%	1.45%	3.185%	2.03
Standard Deviation	$\pm 3.03\%$	$\pm 5.32\%$	$\pm 1.25\%$	$\pm 2.75\%$	$\pm 1.54\%$

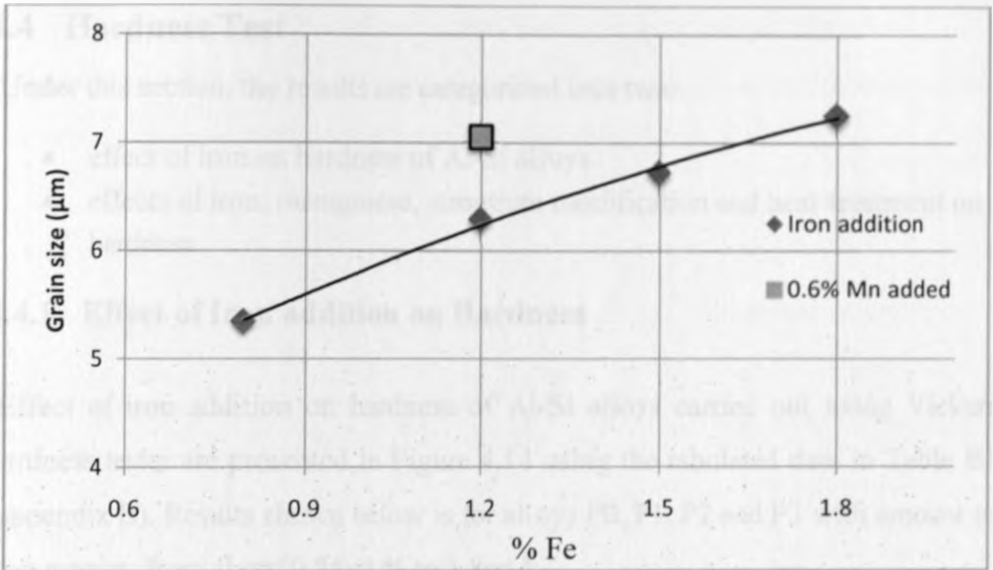


Figure 4.12: Grain size as a function of iron concentration and Mn addition

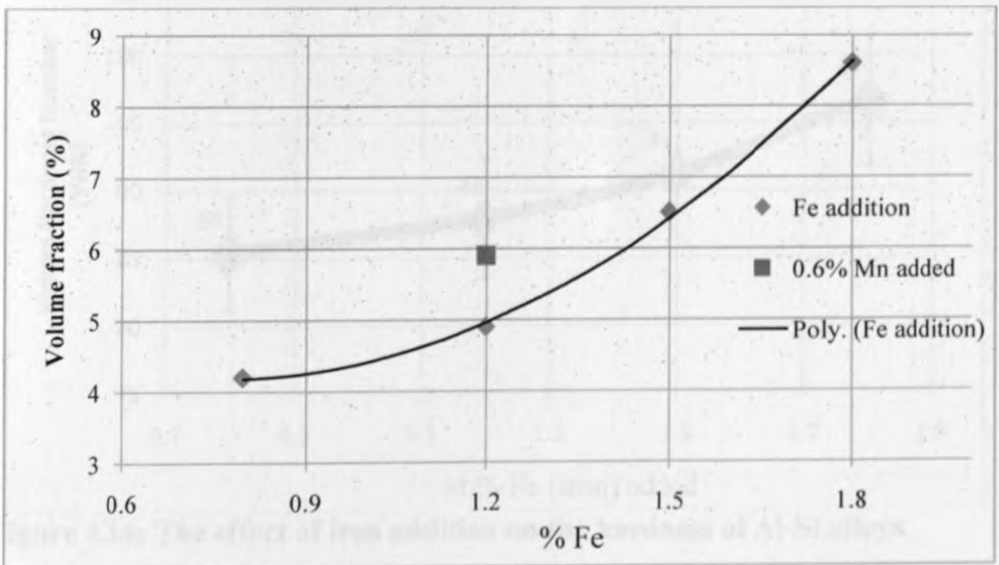


Figure 4.13: Volume fraction of intermetallics as a function of iron concentration

In Fig. 4.13, the volume fraction of the intermetallics present in alloys P0, P1, P2, P3 and P4 is plotted as a function of iron concentration. The above Figures indicate that the size of intermetallic particles as well as the volume fraction increases with addition of iron in the alloy.

4.4 Hardness Test

Under this section, the results are categorized into two:

- effect of iron on hardness of Al-Si alloys
- effects of iron, manganese, strontium modification and heat-treatment on hardness.

4.4.1 Effect of Iron addition on Hardness

Effect of iron addition on hardness of Al-Si alloys carried out using Vickers hardness tester are presented in Figure 4.14 using the tabulated data in Table B1 (appendix B). Results shown below is for alloys P0, P1, P2 and P3 with amount of iron ranging from about 0.84wt.% to 1.8wt.%.

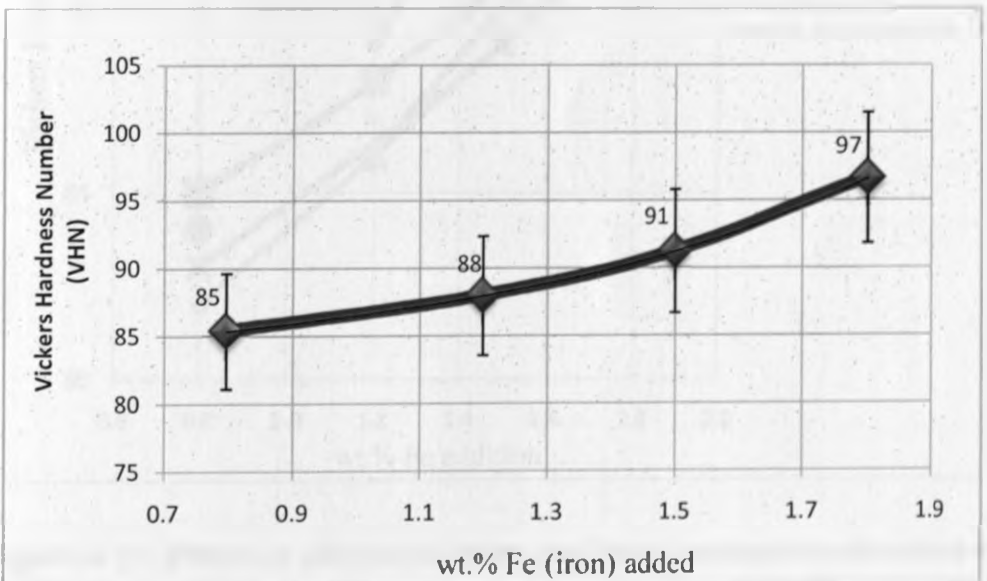


Figure 4.14: The effect of iron addition on the hardness of Al-Si alloys

In Figure 4.14, the effect of iron on the hardness of aluminium alloys P0, P1, P2 and P3 showed that as iron levels increases from 0.84 to 1.8 wt. %, the hardness of Al-Si based alloys increases from 85 to 97 VHN. The effect of iron on hardness can be described by the size and shape of iron-containing intermetallics (particularly β - phase) which are increased with iron content.

4.4.2 The Effects of Fe, Mn, Sr and Heat Treatment on Hardness

Hardness test for alloying elements (Mn and Sr modification) and heat treatment compared with iron added samples are presented in Figure 4.15.

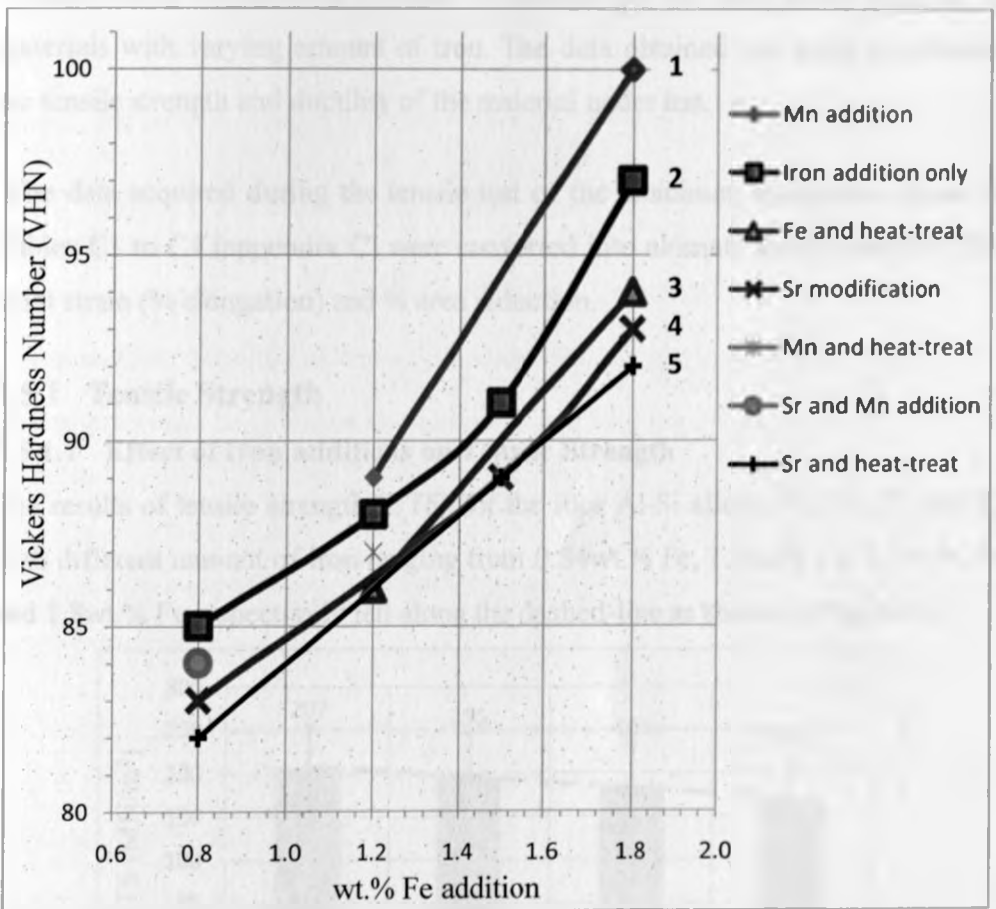


Figure 4.15: Effects of alloying elements and heat treatment on hardness of Al-Si alloys

In Figure 4.15, increase in manganese and iron content leads to an increase in alloy hardness as indicated by line 1 and 2 respectively. However, heat treatment and strontium modification depicted by line 3, 4 and 5 is found to reduce the hardness of aluminium silicon alloys. According to Figure 4.15, the highest hardness number 100 VHN, is related to the alloy P5 with 1.8wt. % of iron with addition of 0.9wt. % manganese.

4.5 Tensile Test

Tensile test of ten alloyed samples and six heat-treated aluminum alloy samples was conducted at the University of Nairobi, Department of Mechanical and Manufacturing Engineering in order to characterize the mechanical behavior of materials with varying amount of iron. The data obtained was used to calculate the tensile strength and ductility of the material under test.

The data acquired during the tensile test of the aluminum specimens shown in Tables C1 to C4 (appendix C) were converted into ultimate tensile stress (UTS), axial strain (% elongation) and % area reduction.

4.5.1 Tensile Strength

4.5.1.1 Effect of Iron additions on Tensile Strength

The results of tensile strength (UTS) for the four Al-Si alloys, P0, P1, P2 and P3 with different amount of iron ranging from 0.84wt.% Fe, 1.2wt.% Fe, 1.5wt.% Fe and 1.8wt.% Fe respectively fall along the dashed-line as shown in Fig. 4.16.

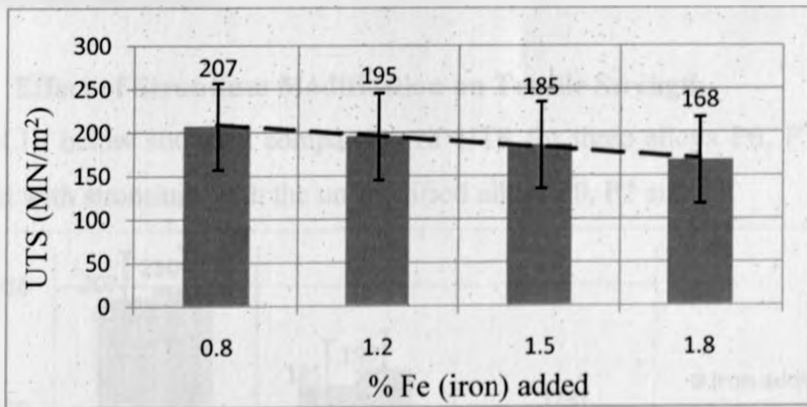


Figure 4.16: The effect of various iron content on the UTS of Al-Si alloys

The results of UTS in Fig. 4.16 show that when the iron content increases, the UTS steadily decreases from 207 MPa with 0.84wt.% of Fe to 168 MPa when the iron content reaches 1.8wt.%. The UTS moves to lower levels with higher iron content probably due to higher amount of intermetallics present in the matrix.

4.5.1.2 Effect of Manganese additions on Tensile Strength

Figure 4.17 shows the UTS of two alloys P4 and P5 with addition of iron and manganese combined compared with ultimate strength with addition of iron only.

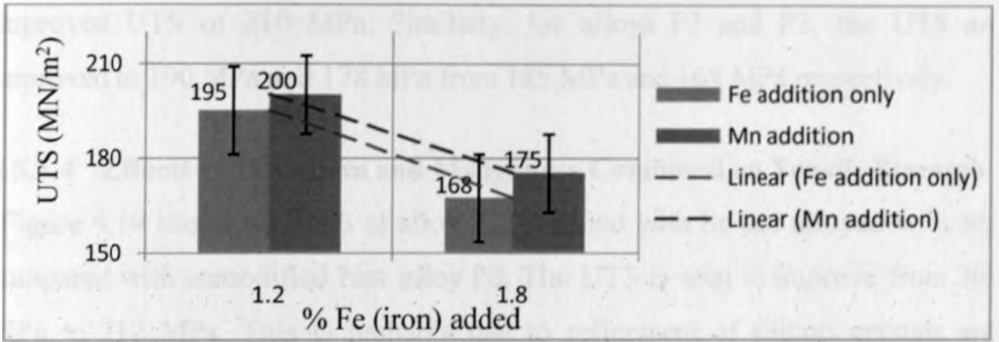


Figure 4.17: The effect of Mn and Fe addition on the UTS of Al-Si alloys

As seen in Fig. 4.17, addition of 0.6wt.% Mn to alloy P4 improves the ultimate strength from 195 MPa to 200 MPa while that of alloy P5 with 0.9wt.% Mn is raised to 175 MPa from 168 MPa. It can therefore be seen that the addition of Mn to some extent suppresses the negative effects of iron on the ultimate strength of aluminium silicon alloys.

4.5.1.3 Effect of Strontium Modification on Tensile Strength

Figure 4.18 below shows a comparison of UTS for three alloys P6, P7 and P8 modified with strontium with the un-modified alloys P0, P2 and P3.

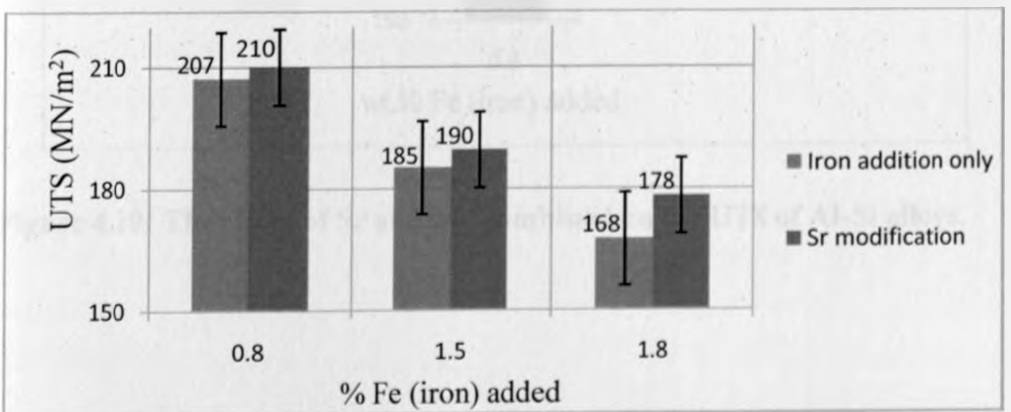


Figure 4.18: The effect of strontium modification on the UTS of Al-Si alloys.

The UTS in Figure 4.18 is seen to improve slightly on modified alloys compared to un-modified ones. Un-modified alloy P0 has an UTS of 207 Mpa while strontium modified alloy P8 with same amount of iron (0.84wt.%Fe) has improved UTS of 210 MPa. Similarly, for alloys P2 and P3, the UTS are improved to 190 MPa and 178 MPa from 185 MPa and 168 MPa respectively.

4.5.1.4 Effects of Strontium and Manganese Combined on Tensile Strength

Figure 4.19 shows the UTS of alloy P9 modified with Sr and alloyed with Mn compared with unmodified base alloy P0. The UTS is seen to improve from 207 MPa to 212 MPa. This is probably due to refinement of silicon crystals and fragmentation of detrimental β - phase promoting some Chinese-like α -phase morphology.

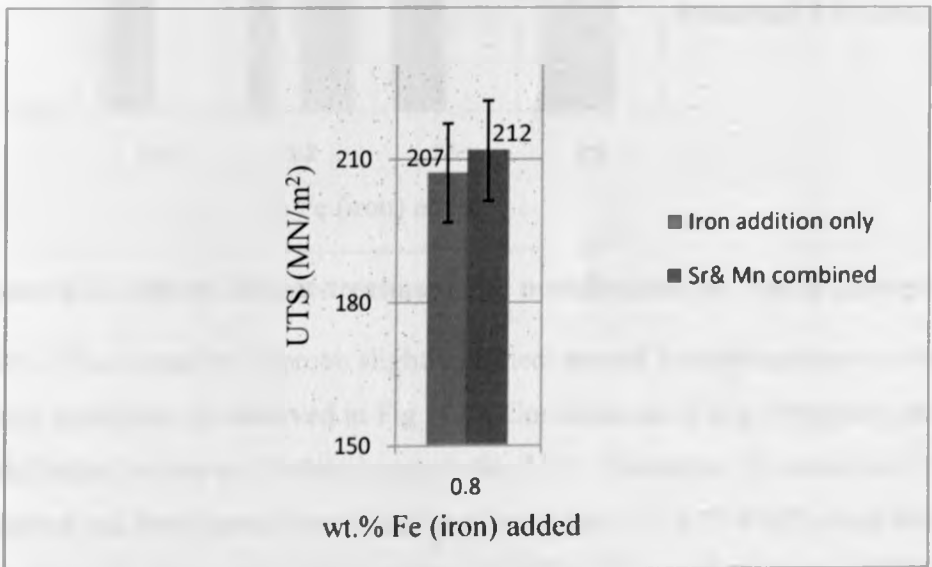


Figure 4.19: The effect of Sr and Mn combined on the UTS of Al-Si alloys.

4.5.1.5 Effects of Heat-treatment, Sr Modified and Mn addition on Tensile Strength

Figure 4.20 shows the UTS of several samples namely H0, H1, H2, H3, H4 and H5 which were heat-treated after addition of Mn and/or modified with strontium.

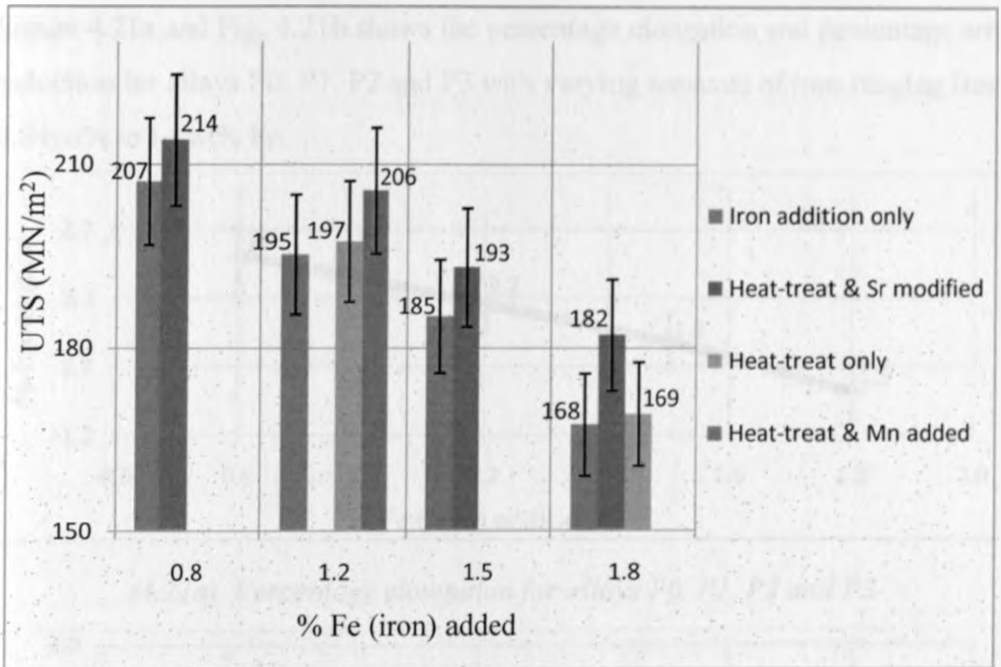


Figure 4.20: Effects of heat-treatment and modification on Tensile strength

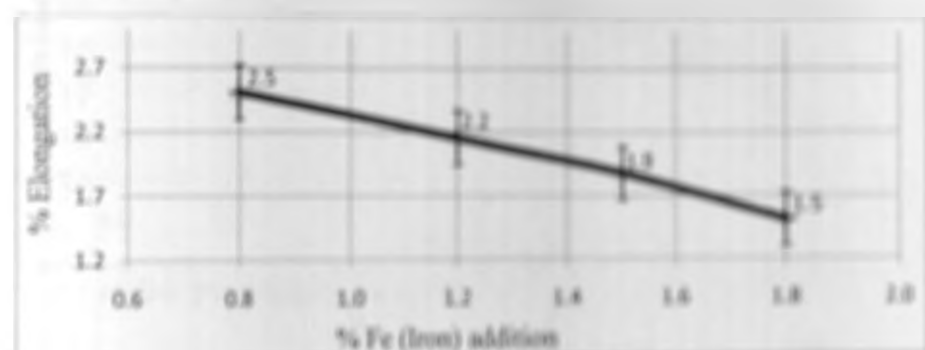
The UTS is found to improve slightly on heat-treated samples compared to untreated specimens as observed in Fig. 4.20. Combination of heat-treatment and Sr modification seems to further improve the UTS. Specimen H5 modified with strontium and heat-treated was found to increase its UTS to 214 MPa from that of base alloy P0 which was found to be 207 MPa. This improvement of UTS is probably due to spheroidization of silicon phase and fragmentation of some β - phases. Generally, heat-treatment is found to slightly increase the UTS.

4.2 Ductility

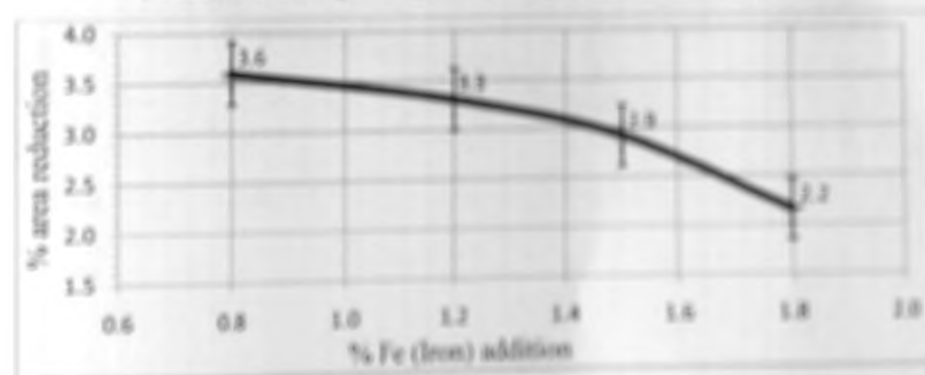
Two parameters namely percentage elongation and percentage area reduction were used to determine the ductilities of the alloys under investigation.

4.2.1 Effect of Iron addition on Ductility

Figure 4.21a and Fig. 4.21b shows the percentage elongation and percentage area reduction for alloys P0, P1, P2 and P3 with varying amounts of iron ranging from 0.84wt% to 1.8wt% Fe.



(4.21a). Percentage elongation for alloys P0, P1, P2 and P3



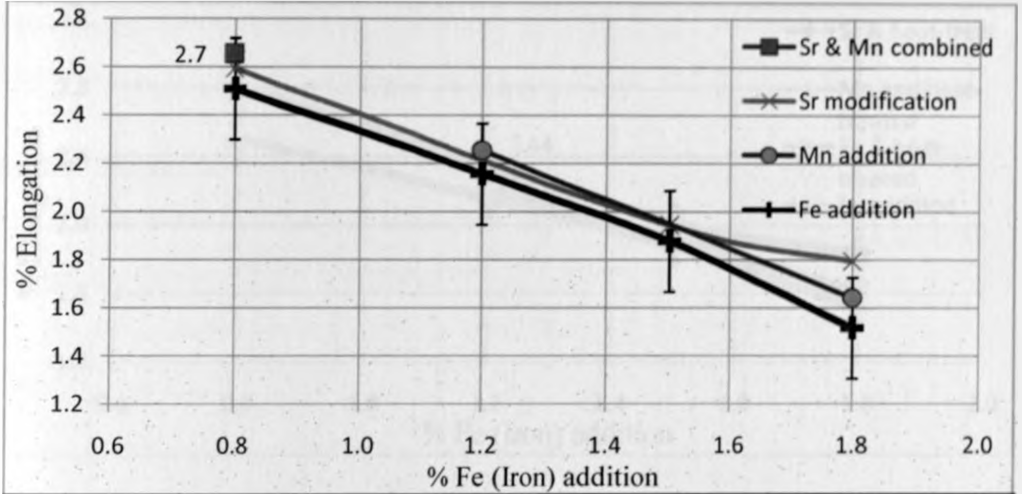
(4.21b). Percentage area reduction for alloys P0, P1, P2 and P3

Figure 4.21: Effect of iron addition on ductility; (a) elongation and (b) area reduction

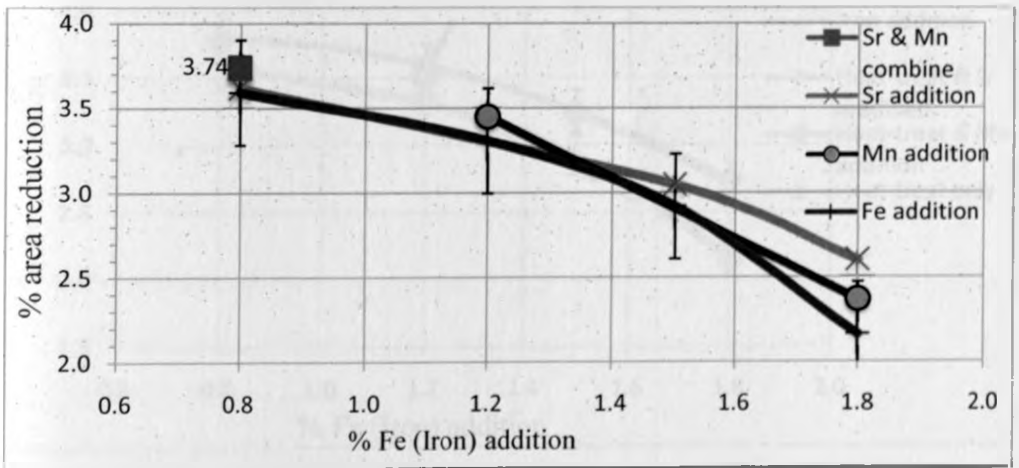
As observed in Figure 4.21, iron addition reduces the ductility of Al-Si alloys. As iron increases, the β - phases were found to increase in number and thus is attributed to detrimental effects on ductility probably due to its brittleness.

4.5.2.2 Effects of Manganese and Strontium Modification on Ductility

Figure 4.22 illustrates the effects of Mn and Sr modification on ductility for alloys P4, P5, P6, P7, P8 and P9.



(4.22a). Percentage elongation for alloys P4, P5, P6, P7, P8 and P9



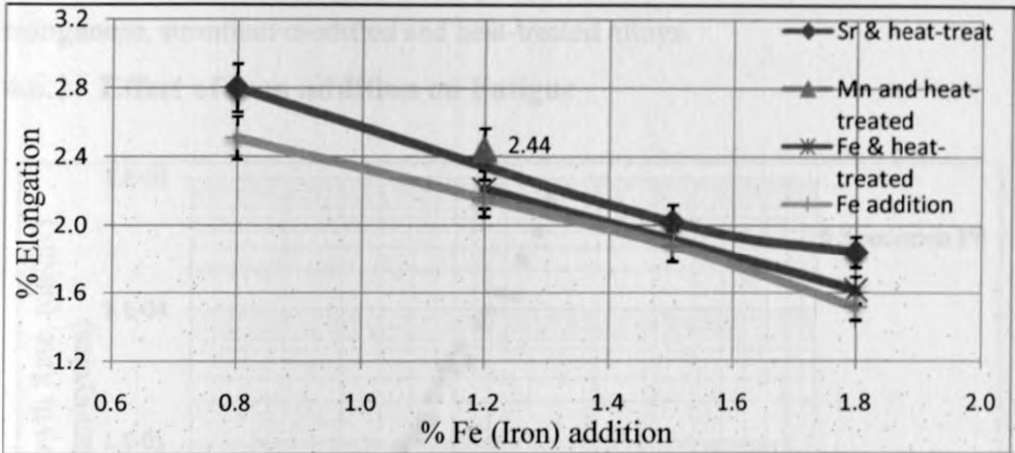
(4.22b). Percentage area reduction for alloys P4, P5, P6, P7, P8 and P9

Figure 4.22: Effects of Fe, Mn addition and Sr modification on ductility

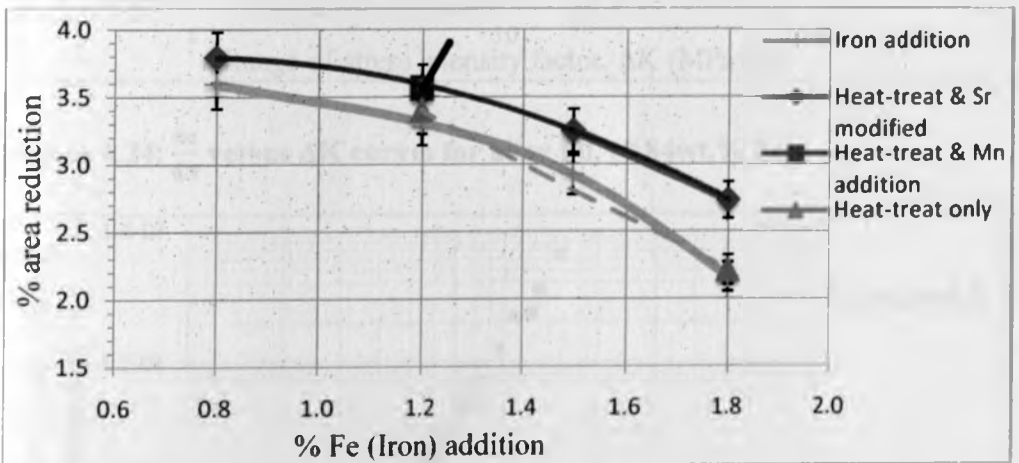
Figure 4.22 shows that ductility of Al-Si alloys slightly improves with addition of Mn and Sr modification. For base alloy P0, the percentage elongation and area reduction increased to 2.7% from 2.5% and to 3.62% from 3.59% respectively on modification.

4.5.2.3 Effect of Heat-treatment on Ductility

Ductility of heat-treated alloys H0, H1, H2, H3, H4 and H5 are shown in Figure 4.23.



(4.23a). Percentage elongation for heat-treated alloys H0, H1, H2, H3, H4, H5



(4.23b). Percentage area reduction for heat-treated alloys H0, H1, H2, H3 to H5

Figure 4.23: Effect of Heat-treatment, Mn and Sr modification on ductility

Heat-treatment was found to slightly improve the ductility of aluminium - silicon alloys as seen in Figure 4.23 with further improvement with a combination of modification and heat-treatment. This is probably attributed to spheroidization of silicon particles and fragmentation of β - iron intermetallic phases.

4.6 Fatigue Results

Fatigue results tabulated in Table D1 and Table D2 (appendix D) are plotted in graphs of Figure 4.24 through Figure 4.35 for varying amounts of iron, manganese, strontium modified and heat-treated alloys.

4.6.1 Effect of Iron addition on Fatigue

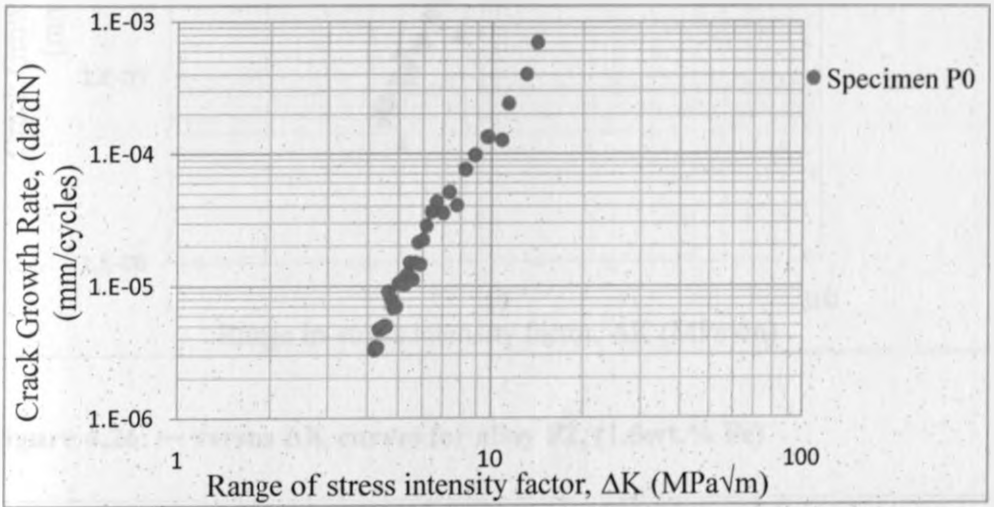


Figure 4.24: $\frac{da}{dN}$ versus ΔK curves for alloy P0, (0.84wt.% Fe)

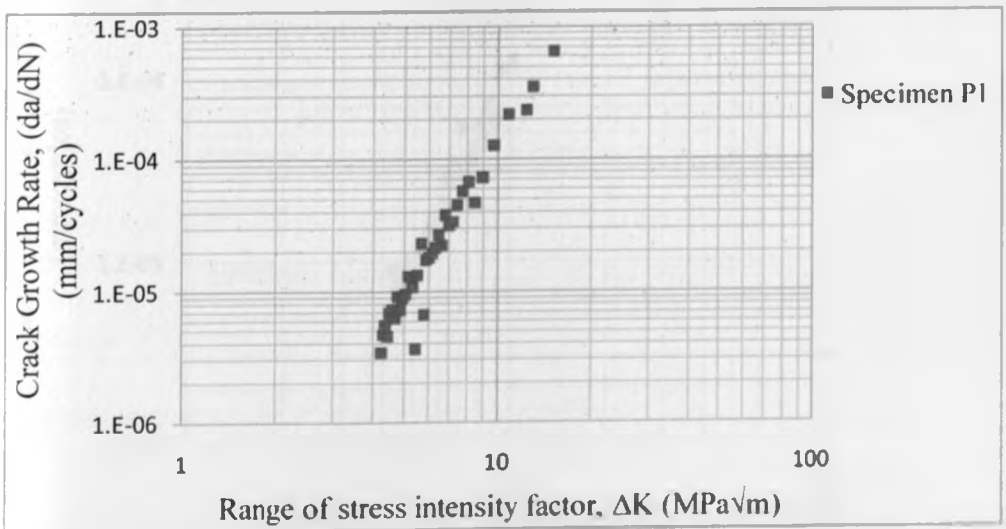


Figure 4.25: $\frac{da}{dN}$ versus ΔK curves for alloy P1, (1.2wt.% Fe)

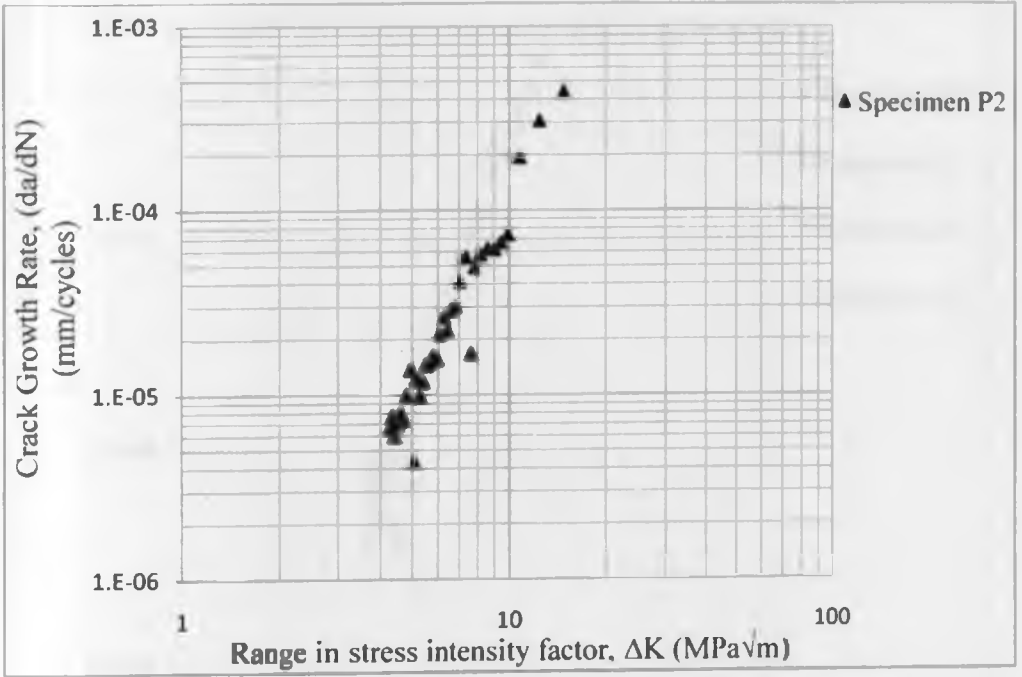


Figure 4.26: — versus ΔK curves for alloy P2, (1.5wt.% Fe)

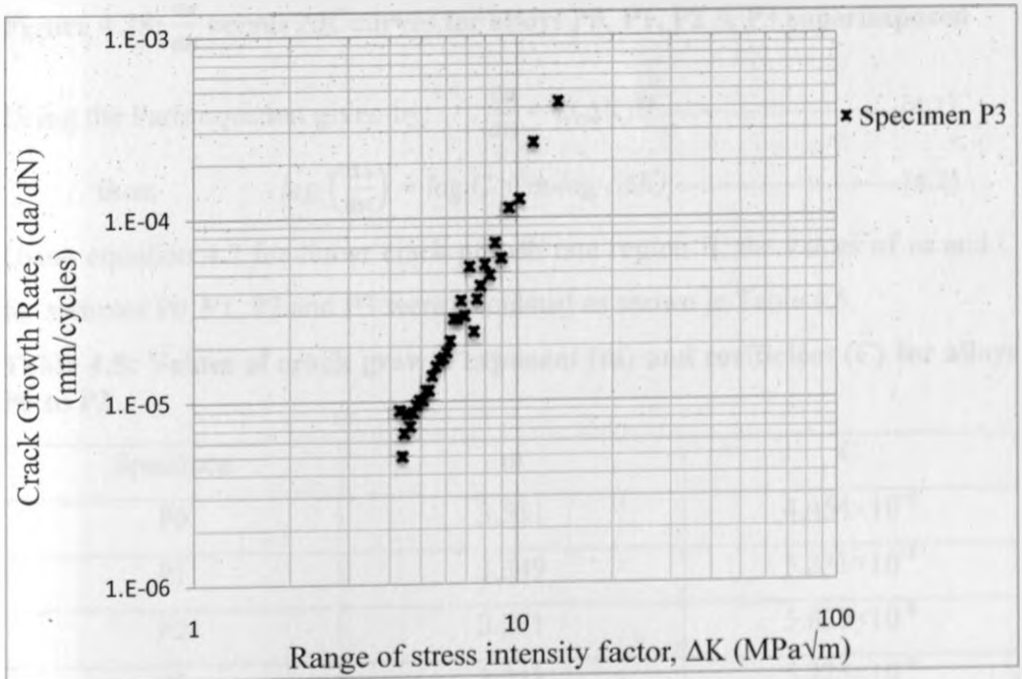


Figure 4.27: — versus ΔK curves for alloy P3, (1.8wt.% Fe)

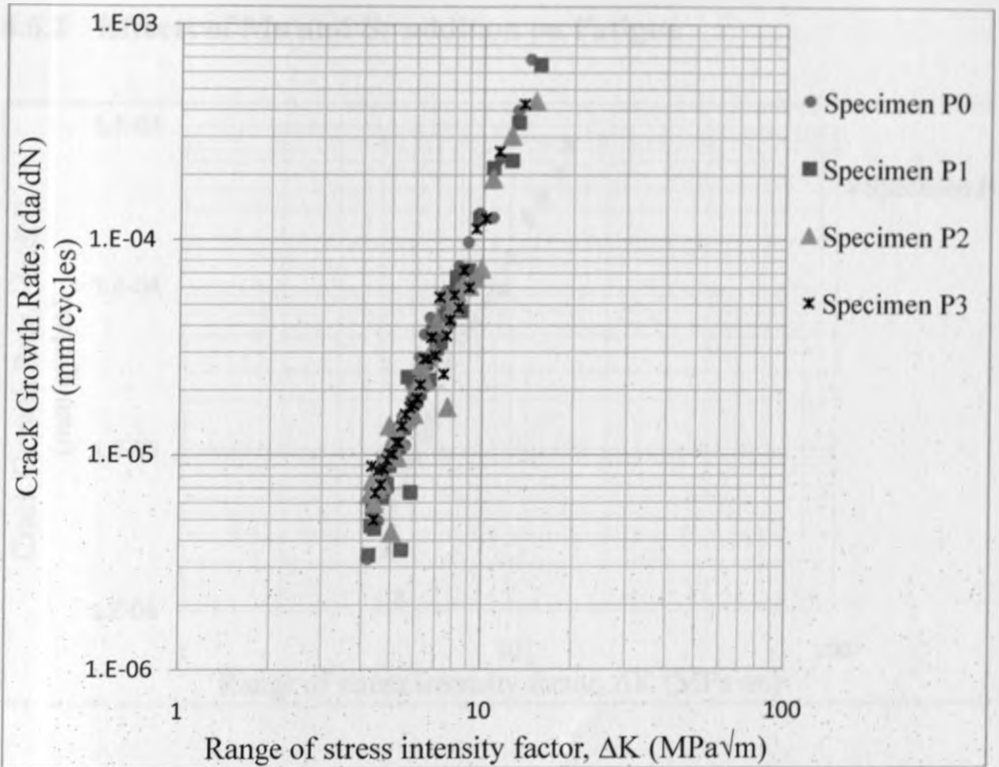


Figure 4.28: $\frac{da}{dN}$ versus ΔK curves for alloys P0, P1, P2 & P3 superimposed

Using the Paris equation given by: $\frac{da}{dN} = C(\Delta K)^m$ [4.1]

\therefore thus; $\log\left(\frac{da}{dN}\right) = \log C + m \cdot \log(\Delta K)$ [4.2]

Using equation 4.2 for linear crack growth rate region II, the values of m and C for samples P0, P1, P2 and P3 were calculated as shown in Table 4.5.

Table 4.5: Values of crack growth exponent (m) and coefficient (C) for alloys P0 to P3

Specimen	m	C
P0	3.511	4.454×10^{-8}
P1	3.349	5.331×10^{-8}
P2	3.251	5.629×10^{-8}
P3	3.233	5.225×10^{-8}

4.6.2 Effects of Mn and Sr addition on Fatigue

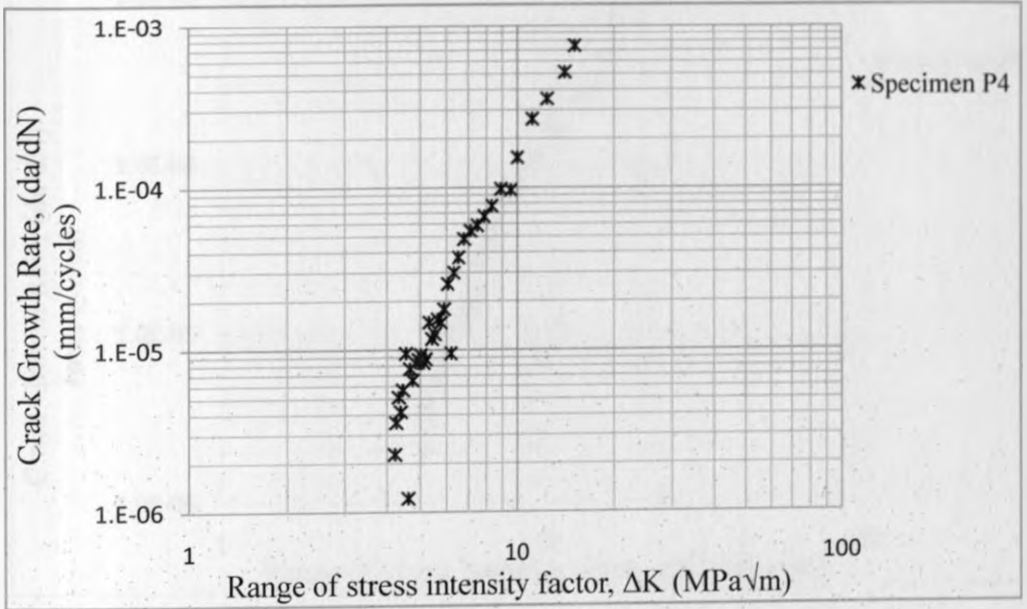


Figure 4.29: $\frac{da}{dN}$ versus ΔK curves for iron and manganese added alloy P4

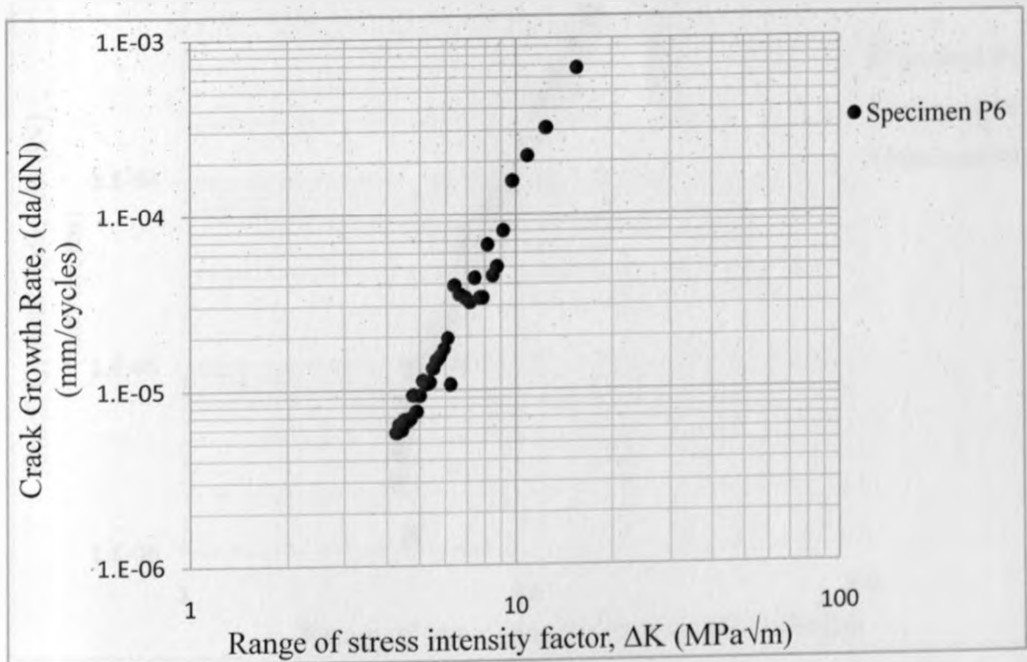


Figure 4.30: $\frac{da}{dN}$ versus ΔK curves for Strontium modified alloy P6

4.6.3 Effect of Strontium and Manganese Combined on Fatigue

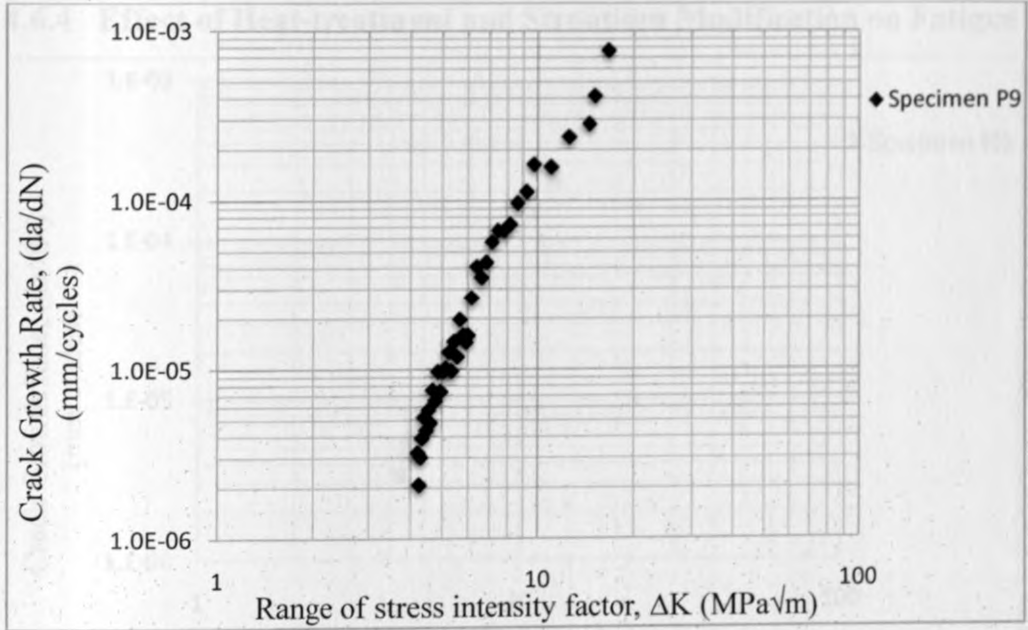


Figure 4.31: — versus ΔK curves for Sr and Mn combined alloy P9

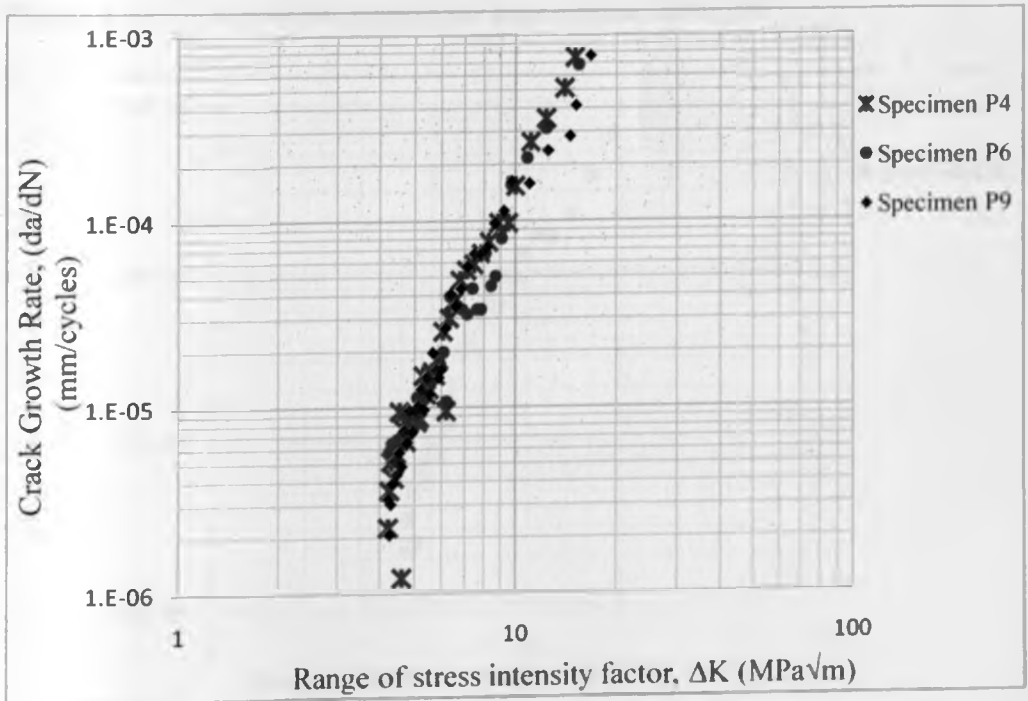
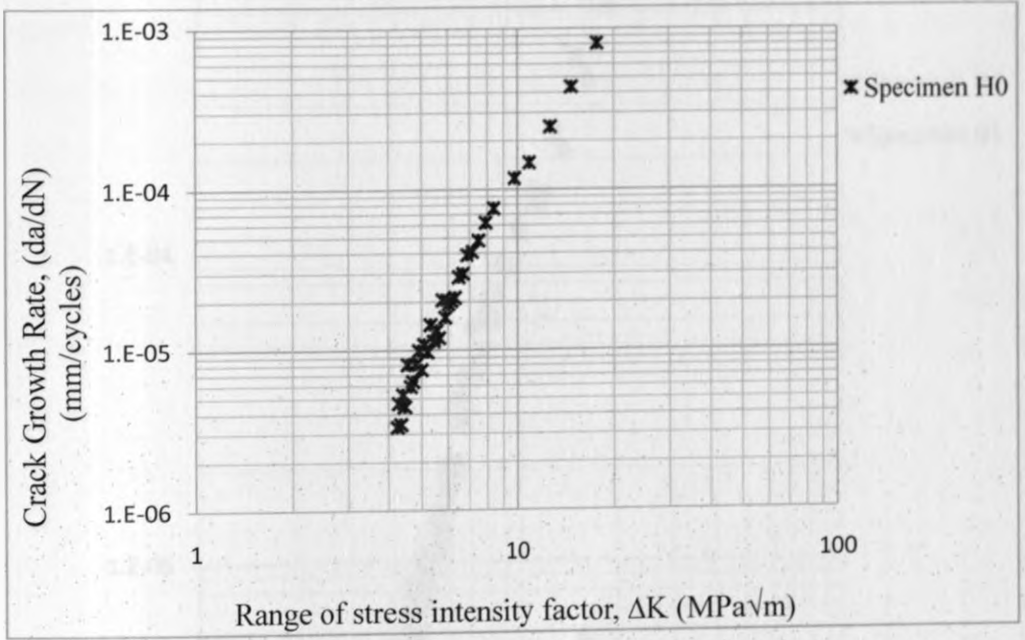
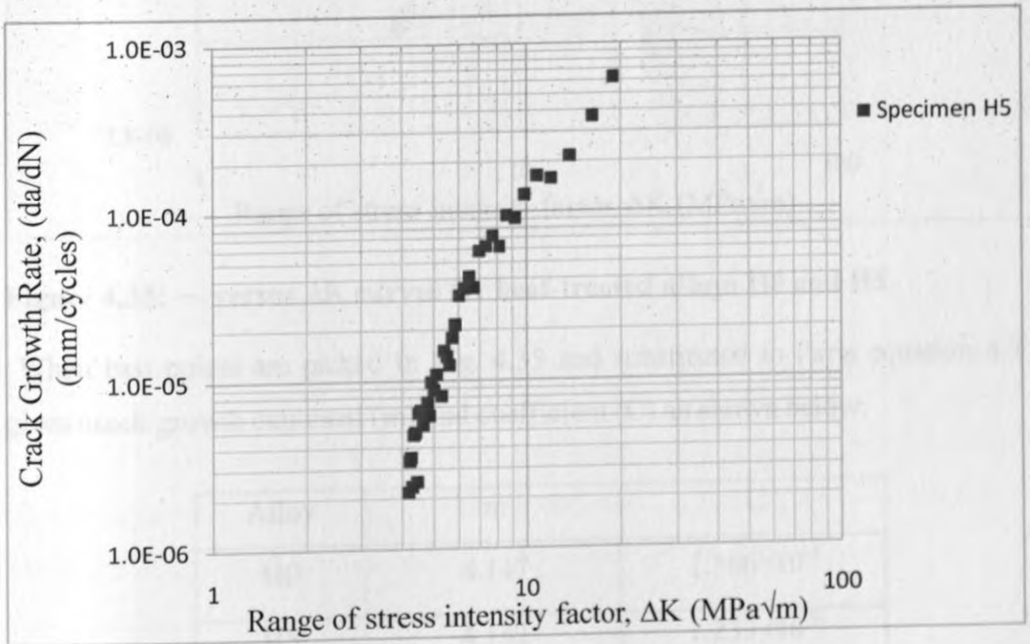


Figure 4.32: — versus ΔK curves for alloys P4, P6 & P9 superimposed

4.6.4 Effect of Heat-treatment and Strontium Modification on Fatigue

Figure 4.33: $\frac{da}{dN}$ versus ΔK curves for heat-treated alloy H0Figure 4.34: $\frac{da}{dN}$ versus ΔK curves for heat-treated alloy H5

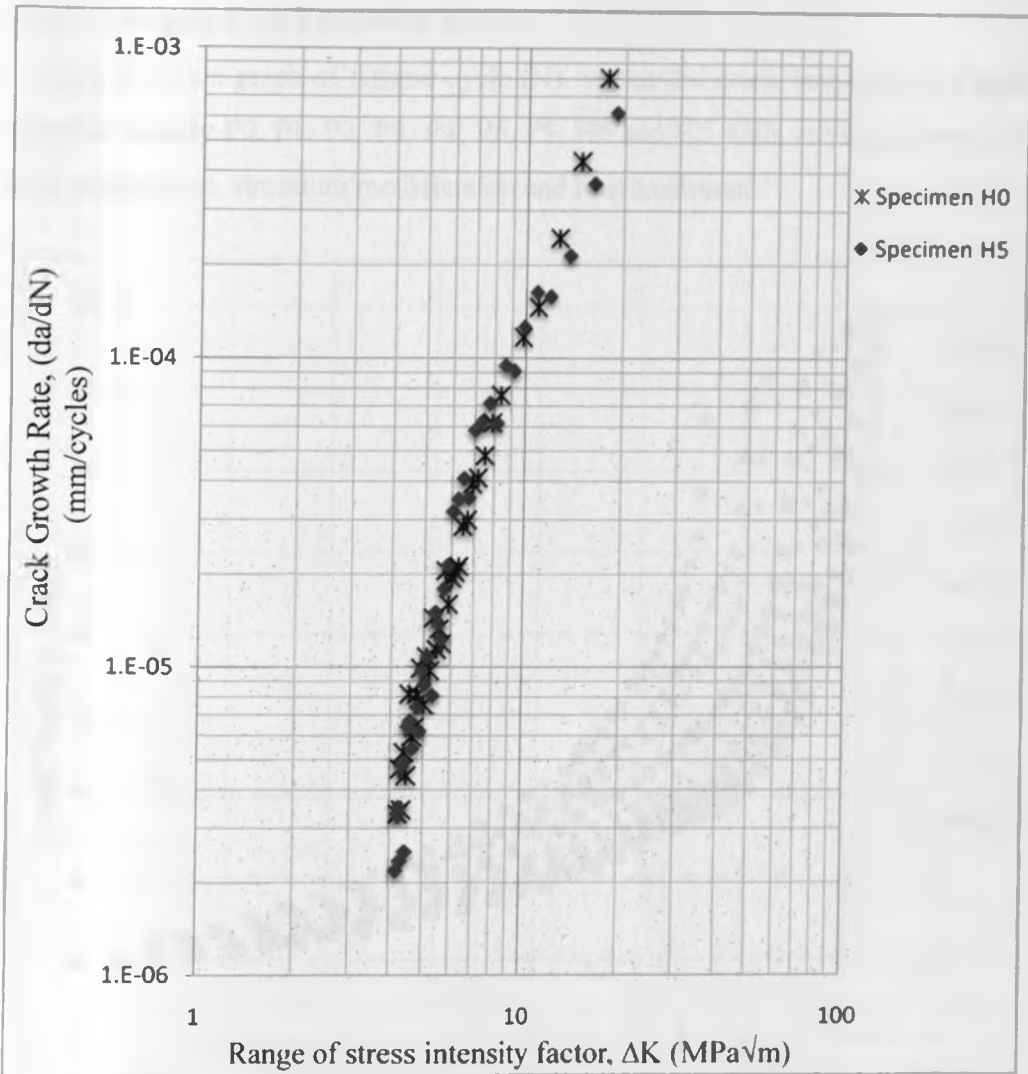


Figure 4.35: — versus ΔK curves for heat-treated alloys H0 and H5

When two points are picked in Fig. 4.35 and substituted to Paris equation 4.2 gives crack growth exponent (m) and coefficient (C) as shown below.

Alloy	m	C
H0	4.147	1.366×10^{-8}
H5	4.152	1.233×10^{-8}

4.6.5 Fatigue Crack Growth Rate

Figure 4.35 is a graph of fatigue cycle (N), versus the crack length (a_n) for nine samples namely P0, P1, P2, P3, P4, P6, P9, H0 and H5 with varying amounts of iron, manganese, strontium modification and heat-treatment.

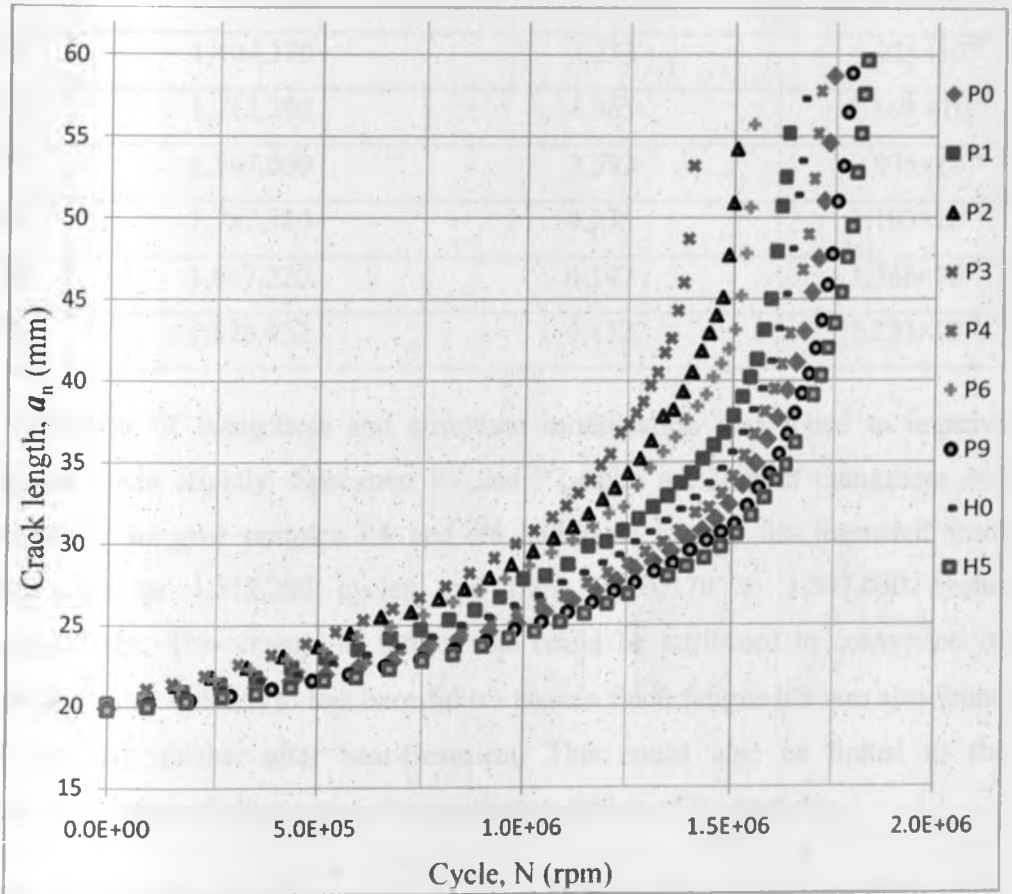


Figure 4.36: Fatigue crack growth of nine alloys with varying elements

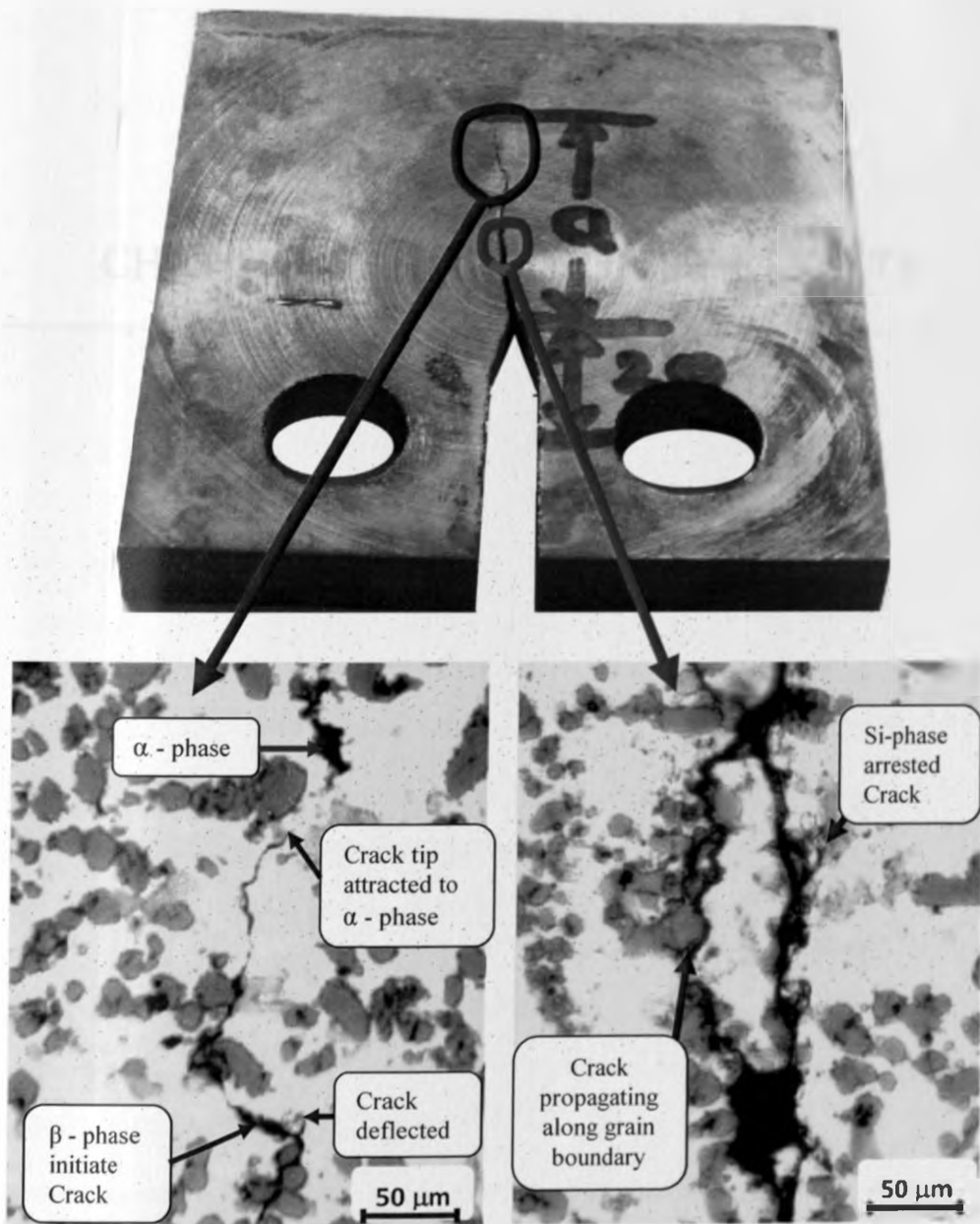
As observed in Figure 4.36, the number of cycles for a specimen to fail reduces with increase in iron content. Sample P0 with iron content of about 0.84% had a life cycle of 1,745,324 while the cycle to failure of specimen P3 with 1.8wt.% iron reduced to about 1,404,370. Table 4.6 shows the life cycle and the corresponding crack length for nine samples with varying amount of iron, manganese, strontium modification and heat-treated samples.

Table 4.6: Values of FCG rates, m , and corresponding fatigue cycle

Sample	Cycles to failure (N)	m	C
P0	1,745,324	3.511	4.454×10^{-8}
P1	1,631,172	3.349	5.331×10^{-8}
P2	1,505,004	3.251	5.629×10^{-8}
P3	1,404,370	3.233	5.225×10^{-8}
P4	1,712,280	4.365	8.169×10^{-9}
P6	1,547,060	3.582	2.935×10^{-8}
P9	1,787,380	4.235	1.103×10^{-8}
H0	1,667,220	4.147	1.366×10^{-8}
H5	1,826,432	4.152	1.233×10^{-8}

Addition of manganese and strontium modification was found to improve fatigue cycle slightly. Specimen P1 and P2 upon addition of manganese and strontium to give samples P4 and P6 had their fatigue life improved from 1,631,172 to 1,712,280 cycles and from 1,404,370 to 1,547,060 cycles respectively. This change in fatigue life could be attributed to conversion of detrimental β - phases to less harmful α - phases. Such fatigue life was also found to improve further after heat-treatment. This could also be linked to the spheroidization of silicon particles and fragmentation of β - particles.

The micrographs of microstructure of a heat-treated alloy observed in Figure 4.37 shows the path in which the crack propagated during fatigue crack test. Such crack is found not to follow a straight line as observed visually without the aid of a microscope.



(4.37a) Crack path (tip)

(4.37b) Branched crack paths

Figure 4.37: Fatigue Crack Path for FCG Test

As observed in Figure 4.37, a crack circumvent the spheroidized silicon phase and instead follows the iron intermetallic phase and where there is no intermetallic phases is attracted along the grain boundary and/or to the pore.

CHAPTER 5: DISCUSSION OF RESULTS

DISCUSSION OF RESULTS

5.1 Introduction

Under this chapter, the results of the previous chapter are discussed on the basis of relating the effects of iron content in aluminium silicon alloys to the cooling rates, microstructure and mechanical properties. The chapter is divided into three sub-sections namely:-

- thermal analysis,
- microstructural analysis and
- analysis of mechanical properties.

The first section of the discussion indicates that altering the chemical composition strongly influences the solidification behavior and types of phases formed. Change in iron and Mn is argued to cause a variation in the reaction temperature while strontium addition tends to lower the nucleation temperature.

Second section of the discussion argues that as iron content increases in a given alloy, more intermetallic particles in the form of β - phases are formed. Such increase in size and number of intermetallic particles are related to increase in volume fraction of intermetallics with addition of iron. The β - particles are mainly needle-like shaped and tend to be changed into Chinese script shape upon addition of manganese while strontium modification and heat-treatment tends to refine and fragment such particles.

In the last section, it is argued that the iron bearing phases, which increase with iron addition as well, increases the alloys hardness at the expense of ductility, strength and fatigue, which decrease with iron addition. The above effects are said to be slightly reversed upon addition of manganese, strontium and heat-treatment of the alloy. Such reversal of harmful effects on ductility and strength are claimed to be as a result of transforming the brittle β - particles from needle-like shape to less detrimental Chinese script and fragmenting them through modifications and/or heat-treatment.

5.2 Thermal Analysis

Thermal analysis were carried out in order to understand the corresponding thermal and solidification conditions of iron, manganese and strontium modified aluminium alloys. Figure 4.1 in chapter four shows the cooling curves obtained for four alloys, (P3, P4, P6 and P9) cast in the preheated permanent cast-iron mold at melt pouring temperature of about 730°C as indicated on the furnace prior to removal of the crucible. Initial temperatures of 710°C, 715°C, 712°C and 708°C respectively registered by the thermocouple for each pouring were somehow lower than the values indicated on the furnace. This temperature difference is attributed to chilling effects due to temperature differences between the molten metal and the cast-iron mold.

Discussion of cooling curves shown in Figure 4.1 will be based on three main precipitation temperatures which took place namely:

- Precipitation of α -Al dendrite network (start of solidification)
- Precipitation of intermetallics and
- Precipitation of Al-Si eutectic.

5.2.1 Precipitation of α - Al Dendrite Network

This region indicated in Figure 4.1 by letter "A" is the temperature at which the primary aluminium phase begins to solidify. The cooling rate prior to this region was between 1.74°C/s and 1.12°C/s before it reached a plateau point due latent heat of fusion released as the aluminium dendrite starts to form. Temperature differences at this point are too minimal compared to the iron content of the four alloys which were chosen for thermal analysis. Precipitation temperature of the primary α -Al dendrite for alloy P3 with 1.8wt.% iron is 596°C which is slightly higher than those of alloys P6 (598°C) and P9 (594°C) modified with strontium but slightly less than that of alloy P4 (602°C) with manganese addition. At this region, iron content and strontium modification seems to have negligible effects on precipitation of α -Al dendrite. On the other hand, alloy P4 with slightly high

precipitation temperature of 602°C, could be linked to precipitation of Chinese script phase as seen in Figure 4.3 which according to Wang et al⁶⁵ may solidify ahead of the α -Al dendrites as large primary particles at low cooling rates.

5.2.2 Precipitation of Intermetallics

Observation of cooling curves in Fig. 4.1 in conjunction with microstructures of Fig. 4.2 through Fig. 4.5 indicates that there are probably four primary intermetallic phases precipitating prior to and/or after the formation of α - Al dendrites. These types of intermetallic phases namely Mg_2Si and $\beta-Al_5FeSi$ in alloys P0 to P3, $\alpha-Al_{15}(Fe,Mn)_3Si_2$ with manganese added alloys P4 and P5 and $\alpha-Al_8Si_2Fe$ on strontium modified and heat-treated samples were identified in chapter four. These are the phases which most likely precipitated in regions "B" and "D" on Figure 4.1.

In Fig. 4.1 (a) for alloy P3, the first precipitation was probably the β -phase which took place at 577°C, while that of alloy P4 shown in Fig. 4.1 (b) which is α -Chinese script precipitates at a high temperature of about 592°C. Those of Fig. 4.1 (c) and (d) modified with strontium precipitated at 587°C. It is observed therefore that the precipitation temperature of intermetallic which lies between the liquidus and eutectic reaction is higher in strontium modified compared to the unmodified alloy. In Sr-modified alloy P6 and P9, the precipitation temperature of intermetallic is raised to 587°C compared to un-modified alloy of P3 which is 577°C most likely because the strontium segregates them into clusters away from the well-modified silicon particles. For alloy P4, the presence of manganese might have pushed the precipitation temperature of Chinese script phase to occur at 592°C.

In Fig. 4.1, the hump occurring at point "D" of the cooling curves are probably due to second precipitation of a phase. These points are identified as post eutectic temperatures of iron intermetallics. The post eutectic reactions for alloys P3, P4, P6 and P9 in Fig. 4.1 occurs at a temperature of 504°C, 535°C, 502°C and 500°C

respectively. Since our base alloy had magnesium content of about 1.21wt.%, the post eutectic reaction most likely involved the precipitation of Mg_2Si in alloy P3 and transformation of $\beta-Al_5FeSi$ phases to Chinese script $\alpha-Al_{15}(Fe,Mn)_3Si_2$ phases in alloy P4 and to $\alpha-Al_8Fe_2Si$ phases in alloy P9.

5.2.3 Precipitation of Al-Si Eutectic

The eutectic temperatures of samples P3 and P4 given in Table 4.1 are 547°C and 549°C respectively. Upon strontium modification, eutectic plateau temperatures of specimens P6 and P9 are lowered to 540°C and 543°C respectively. In binary state where silicon and aluminium are the only elements, the silicon forms a eutectic with aluminium at 11.7wt.%Si and eutectic temperature of 577°C as shown in Figure 5.1 and as reported by Mondolfo¹. Silicon addition at levels other than 11.7wt.% with addition of other small amounts of elements like Mg, Cu, Ni or Sr tend to modify the eutectic phase of Al-Si alloy shifting the eutectic temperature mostly to a lower level. It can be seen therefore in Figure 4.1 that addition of strontium slightly lowers the eutectic temperature for alloys P6 and P9. These results compare very well with those of Samuel et al⁵⁵, who investigated the effects of cooling rate and Sr-modification on porosity and iron-intermetallics formation in Al-6.5%Si-3.5%Cu-Fe alloys and report a decrease in the silicon eutectic temperature.

Though translation of these observations in terms of strontium modification on eutectic temperature is somehow complicated for alloys containing high levels of Cu and Mg, it is believed that suppression of eutectic growth and suppression of eutectic nucleation is the reason for decrease in eutectic nucleation. As observed in Figure 4.2, silicon is seen to have nucleated in the primary $\alpha-Al$ dendrite as flaky silicon but for strontium modified samples depicted in Fig. 4.4, silicon is completely refined. This phenomenon will be discussed further in the next section on microstructural analysis.

Summary of Thermal Analysis

During solidification of molten metal, the melt is transformed to solid state from molten state in a process involving loss of heat. As the temperature of the melt falls, the thermal agitation of the atoms of the liquid reduces, allowing small random aggregations of atoms into crystalline regions. Molten aluminium will then be converted into solid by a process of nucleation which is the aggregation of clusters of atoms representing the first appearance of the new phase followed by growth of other phases where crystals develop by addition of atoms according to the lattice pattern. The presence of other alloys such as Fe, Mg, Mn, Sr, etc. tend to concentrate in ways to trigger the nucleation and growth of second phases or shrinkage pores.

5.3 Microstructural Characteristics

Under this section, microstructural characteristics and phase analysis will be discussed in terms of iron addition, manganese addition, strontium modification and effects of heat-treatment. Under iron addition section, the alloys differ only in iron content, and therefore their microstructures are similar, only differences are the size and fractions of the phases present. This also applies to microstructures modified with strontium, or manganese added or heat-treated where their microstructures are largely similar.

As discussed earlier under thermal analysis, the solidification of the Al-Si alloy begins with the precipitation of α -Al dendrites followed by a residual liquid which, on reaching a critical concentration of silicon, develops a lamellar eutectic alloy. This can be discussed from the thermodynamic point of view whereby on reaching the liquidus temperature, some of the liquid solidifies and crystallizes into the solid α -Al phase. With additional heat removal, higher amounts of α -Al phase forms between the liquidus and solidus temperatures where small quantity of secondary aluminium nucleates and grows on primary silicon which is then followed by the usual flake eutectic growth. The flake eutectic structure of silicon also uniformly grows between the increasingly large proportions of primary

aluminium. This can be illustrated in the phase diagram in Figure 5.1 and microstructures of Figure 4.2 in which the primary silicon crystals are seen to be distributed relatively homogeneously in the aluminium matrix.

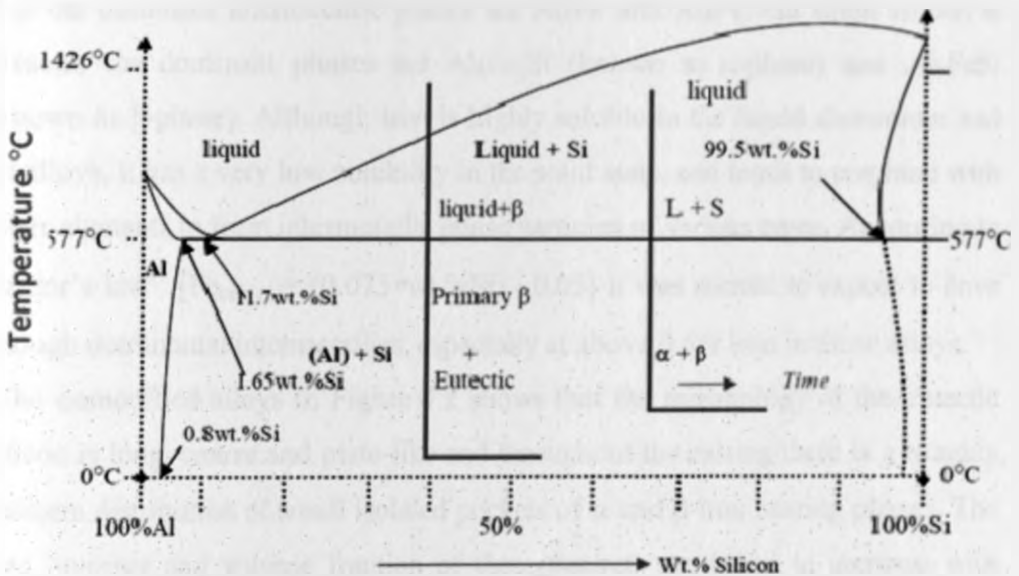


Figure 5.1. Phase Diagram of binary Al-Si alloy¹⁹

5.3.1 Effects of Iron addition on Microstructure

Figure 4.2 shows the microstructures of four unmodified alloys, P0, P1, P2 and P3, with varying amounts of iron ranging from 0.84wt.%, 1.2wt.%, 1.5wt.% to 1.8wt.% Fe respectively. The microstructures of these alloys basically comprised of aluminium dendrites, eutectic silicon and iron-rich intermetallic particles which differ slightly. Apart from α -Al dendrites and primary silicon, there are three types of intermetallics observed in the microstructure of these alloys: β -phase (Al_5FeSi), α -phase ($\text{Al}_{15}\text{Fe}_3\text{Si}_2$) and π -phase (Mg_2Si).

The microstructure of alloys P0, P1, P2 and P3 in Fig. 4.2 shows that as iron content increases from 0.84wt.% to 1.8wt.%, the size of the β - Al_5FeSi needles is also increased. This concurs with Mondolfo¹ who reported that addition of iron to the Al-Si alloy causes a slight increase in the lattice constants enabling more

intermetallics to be formed. This can also be linked to observation of Figure 4.12 and Figure 4.13 where both grain size and volume fraction of intermetallics increased with increase in iron content. In the absence of silicon, it is reported that the dominant intermetallic phases are Al_3Fe and Al_6Fe , but when silicon is present, the dominant phases are $\text{Al}_8\text{Fe}_2\text{Si}$ (known as α -phase) and Al_5FeSi (known as β -phase). Although iron is highly soluble in the liquid aluminium and its alloys, it has a very low solubility in the solid state, and tends to combine with other elements to form intermetallic phase particles of various types. According to Taylor's law¹⁴ [$\text{Fe}_{\text{critical}} = (0.075 \times \text{wt.}\% \text{Si}) - 0.05$] it was normal to expect to have enough detrimental intermetallics, especially at above 0.6% iron in these alloys.

The unmodified alloys in Figure 4.2 shows that the morphology of the eutectic silicon is long, coarse and plate-like and throughout the casting there is a roughly uniform distribution of small isolated pockets of α and β -iron bearing phases. The size, number and volume fraction of these pockets are found to increase with increase in iron content.

5.3.2 Effects of Manganese addition on Microstructure

It is observed in Figure 4.3 that the appearance of the microstructures of alloys to which iron and manganese were added P4 and P5 are slightly different from those of Figure 4.2 which are manganese free. Inspecting Figure 4.3 carefully, it may be revealed that both phases have a script-like morphology. As discussed earlier under thermal analysis section, addition of manganese to molten Al-Fe-Si alloy reported by Wang et al⁶⁵ may precipitates as large Chinese script particles of $\alpha\text{-Al}_{15}(\text{Fe}, \text{Mn})_3\text{Si}_2$ ahead of α -Al dendrites.

The explanation is that, intermetallic particles formed prior to the solidification of the α -Al dendritic grain network (i.e. growing freely within the liquid) or those formed at the same time as the dendritic network (but within the remaining liquid) tend to grow much larger than those formed later, during or after the period of Al-Si eutectic solidification, due to a less liquid space available for growth to occur

during these later stages. In general, the larger the particle, the greater its detrimental on mechanical properties. Increasing the concentration of iron and manganese tends to result in earlier formation of intermetallic phase particles and hence more unconstrained growth is able to occur as seen in Fig. 4.3(c). A slower cooling rate could also increase the risk of forming large particles because the time available for growth is increased. However, under casting conditions applied in this work, the grain size of these intermetallics grows more typically in the size range of $7.05 \pm 0.52 \mu\text{m}$ Figure 4.12.

Comparison of microstructure in Fig. 4.3 to grain size and volume fraction in Fig. 4.12 and Fig. 4.13 shows that increase in the volume percentage of intermetallics is related to grain size number and volume fraction of particles formed in a unit volume. It may be assumed that when more iron was added to the alloy, more driving force is produced; resulting in a decrease of the total surface energy of solid silicon, which can be accomplished by lowering the surface area per unit volume of present phases.

5.3.3 Effects of Strontium Modification on Microstructure

Figure 4.4 shows microstructures of three alloys modified with strontium. Unlike unmodified alloys in Fig. 4.2 where the microstructure of the alloys consists of large number of $\beta\text{-Al}_5\text{FeSi}$ and long flaky silicon, the microstructure of modified alloys exhibits refined silicon crystals and fragmented intermetallic particles. This silicon phase is rich in strontium and appears in the form of thin, branched pale needles in the microstructure. Strontium modified alloys are also seen to have coarse and/or reduced number of β -platelets. In these strontium-modified alloys, very little α -iron can be seen and the β -plates are reduced and much larger than those found in the equivalent unmodified alloys as seen in Figure 5.2.

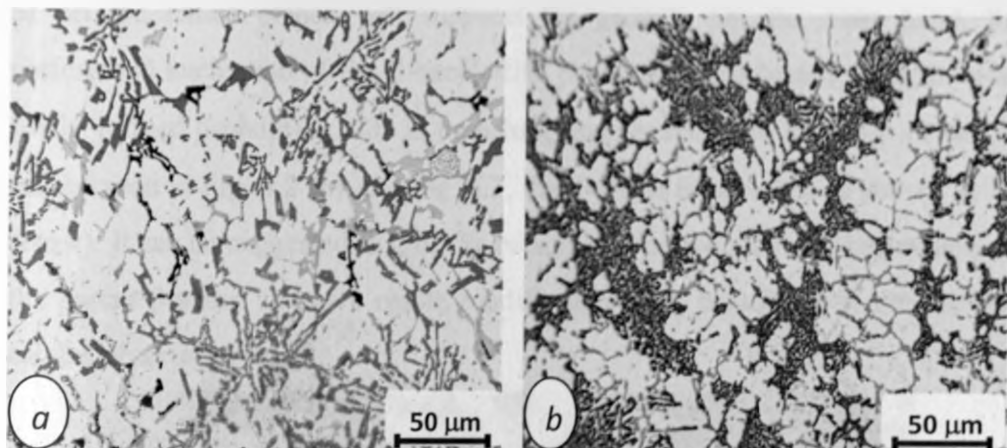


Figure 5.2: Microstructural comparison of alloy with 0.84wt.%Fe exhibiting (a) unmodified and (b) strontium modified morphologies

The mechanisms of the modification of the β -phase by Sr can be explained with regards to: (a) nucleation and (b) growth of the β -phase.

Since the number of the β -phase particles per unit area is reported to correlate with the nucleation mechanism, then the increase in the number of the β -particles per unit area upon modification is an indication that Sr addition influenced the nucleation process of the β -crystals. A change in the interfacial surface energy by addition of an impurity (*e.g.* Sr) may affect the nucleation process. It can be suggested that Sr may reduce the interfacial surface energy between the α -Al and β -phases, influencing the nucleation process of the β -phase. The same effect has been reported to occur for nucleation of eutectic Si by Mondolfo¹. Other factors which possibly influence the nucleation behavior are the nucleation sites and the under-cooling for the formation of β and the eutectic phases during solidification.

The length of the β -particles is known to correlate with the growth mechanism. Therefore, the decreased length and volume fraction of the β -phase in the Sr modified alloys indicate that the growth of these particles is greatly suppressed by Sr addition. This is particularly likely in the view of well-known effect of Sr in modifying the growth of the eutectic silicon in Al-Si alloys³¹. Growth is known to take place in certain crystallographic planes of β and Si phases and adsorption of

Sr on the lattice planes will suppress the growth. On the other hand, the preferential nucleation of the β -needle-like phase from the "parent β -phase" (the firstly formed β -phase) results in branching and formation of a large β -phase (as can be seen in Fig. 4.2 (h) and Fig. 5.3, the β -phase is branched as shown by an arrow). It can be suggested that the Sr poisons the preferential nucleation sites on the parent β -phase and as a result, modification (less branching) of the β -phase can be expected.

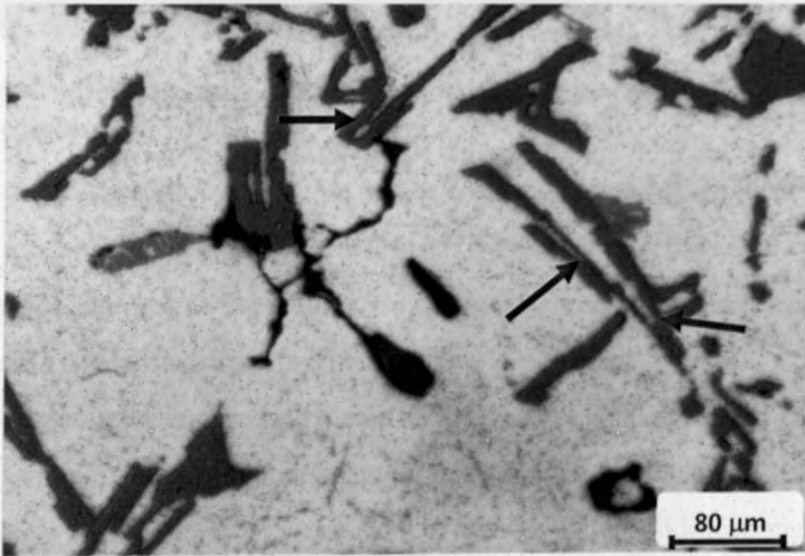


Figure 5.3: Microstructure of unmodified alloy P3 showing branched structure

5.3.4 Effects of Strontium and Mn Combined on Microstructure

The influence of manganese and strontium combined on the crystallization of intermetallics was investigated for alloy P9 and its microstructure is presented in Figure 4.5. The flake-like eutectic silicon and the branched structure of the β -phase, as shown in Figure 4.3 for the strontium free alloy (only Mn addition), is converted into a refined eutectic silicon and a modified and less-branched β -phase structure, Figure 4.5, by manganese and strontium modification. Figure 5.4 shows a comparison of strontium and manganese combined microstructure with that of manganese addition only.

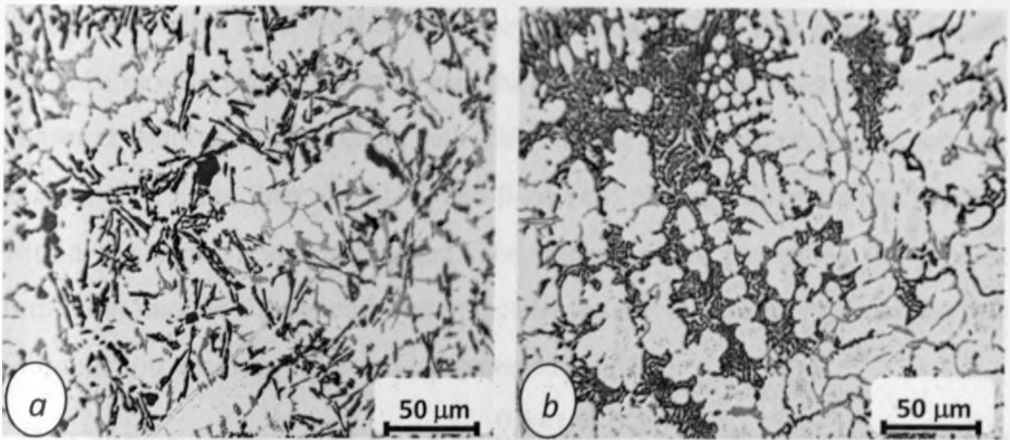


Figure 5.4: Microstructure of (a) Mn added alloy compared to that of (b) Mn and Sr combined

As can be observed in Fig. 5.4, Mn and Sr combined is one of the most effective way to inhibit the formation of plate-like β -phase and refinement of silicon particles. Mechanisms of the modification of the β -phase by Sr and Mn combined addition can be clarified from two points of view, including:

- Changing the nucleation process and preventing growth of the β -phase,
- Promotion of the Chinese script formation instead of the β -phase.

For better understanding this mechanism of modification, solidification sequence of these alloys must be taken into account as follows. Since aluminium forms eutectic with iron and silicon at 1.7wt.% Fe and 11.7wt.% Si respectively (Figure 5.1), then a solidification routes depicted on the aluminium-rich corner of the Al-Si-Fe-Mn equilibrium phase diagram with 0.6wt.% Mn can be constructed as shown in Fig. 5.5.

The composition of sample P9 with addition of Mn and Sr combined was 0.84wt.% Fe and 8.53wt.% Si as indicated in Figure 5.5. The solidification process starts by the formation of Al - dendrites and the interdendritic liquid becomes enriched in Fe and Si according to path (1). The solidification line penetrates the $Al_{15}(Mn,Fe)_3Si_2$ surface and starts the second reaction by which the latter phase crystallizes along path (2a). Some Mn is consumed, and the

solidification line soon reaches the valley between the two iron bearing phases, $\text{Al}_{15}(\text{Mn,Fe})_3\text{Si}_2$ and $\beta\text{-Al}_5\text{FeSi}$, and during the following reaction, these two phases crystallize together along path (2b) until the eutectic composition, point (3) is reached³¹. From there on Al, Si and $\beta\text{-Al}_5\text{FeSi}$ phases will crystallize together within the ternary eutectic reaction. The mechanism of preventing the β -phase formation may be suggested to take place by the effect of Sr to suppress the path (2b) reaction resulting to less and fragmented β -phases.

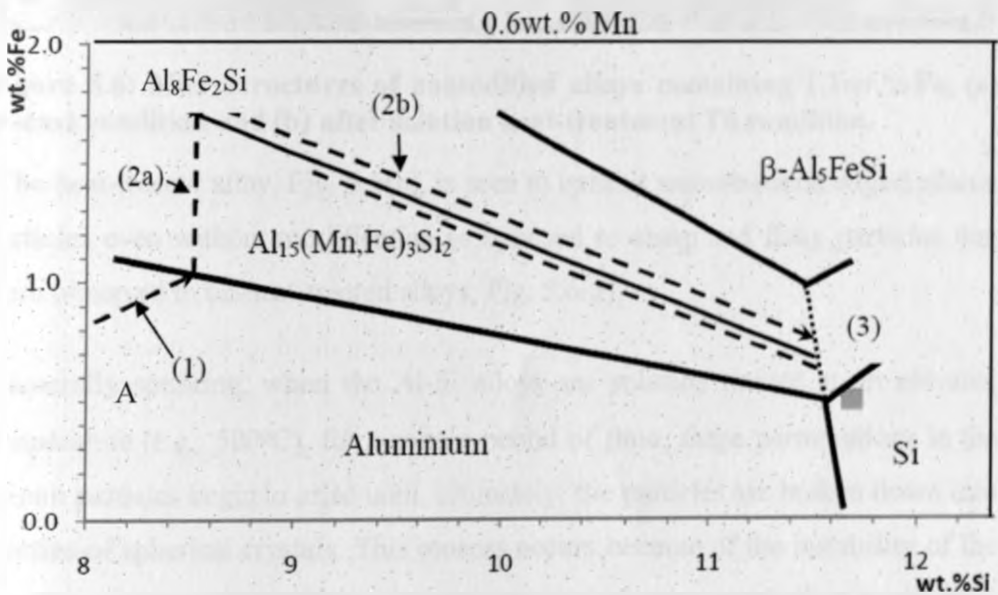


Figure 5.5: Solidification routes in the Al-Si-Fe-Mn equilibrium phase diagram³¹. The composition of samples is indicated by point 'A'.

5.3.5 Effects of Heat-Treatment on Microstructure

Unlike as-cast samples whose microstructures were observed in Figure 4.2 through Figure 4.5, the microstructure of fully heat-treated T6 condition consists of aluminium cells bounded by irregularly shaped silicon particles and some fragmented iron-bearing compounds. Figure 4.6 to Figure 4.8 shows the morphologies and distributions of these acicular and Chinese-script intermetallic phases after heat-treatment was carried out. A microstructural comparison of two specimens with same amount of iron (1.2wt.% Fe) before and after solution heat-treatment is shown in Figure 5.6.

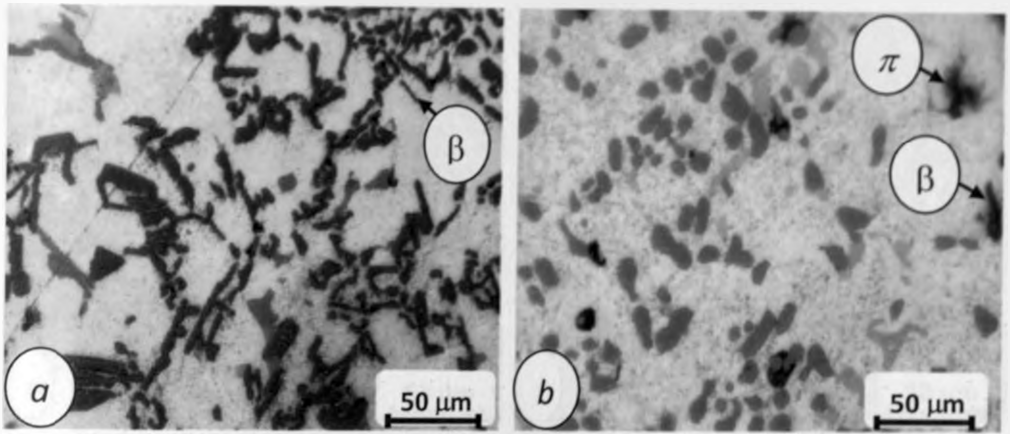


Figure 5.6: Microstructures of unmodified alloys containing 1.2wt.%Fe, (a) as-cast condition and (b) after solution heat-treatment T6 condition.

The heat-treated alloy, Fig. 5.6(b), is seen to exhibit smooth-round edged silicon particles even without modification as opposed to sharp and flaky particles that were observed in un-heat-treated alloys, Fig. 5.6(a).

Generally speaking, when the Al-Si alloys are solution treated at an elevated temperature (e.g., 500°C), for a certain period of time, shape perturbations in the silicon particles begin to arise until, ultimately, the particles are broken down into a series of spherical crystals. This process occurs because of the instability of the interfaces between two different phases and is driven by a reduction in the total interfacial energy. This stage is called the fragmentation or spheroidization stage. Subsequently, the silicon particle size begins to increase as a result of particle coarsening if its size is greater than the critical volume, whereas smaller particles dissolve according to Ostwald ripening,⁵⁸ a stage termed the coarsening stage.

The micrographs in Figure 5.7 (a combination of Fig. 4.4 (b) as-cast and Fig. 4.8 (b) heat-treated alloys both Sr modified) illustrates the combined effect of Sr modification and solution treatment on an alloy with 1.5wt.% of iron. The fine strontium modified (fibrous) Al-Si eutectic cells in the as-cast structure Fig. 5.7(a) are altered substantially by solution treatment, with the eutectic silicon component being transformed into coarsened, individual and rounded particles Fig. 5.7(b).

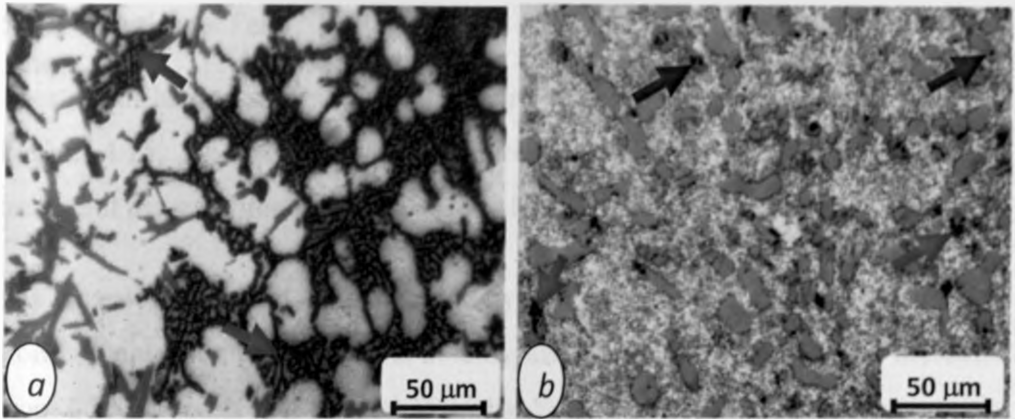


Figure 5.7: Microstructures of Sr modified alloys containing 1.5wt.% Fe: (a) as-cast condition and (b) after solution heat-treatment T6 condition.

In Fig. 5.7, the fine Chinese-script Mg_2Si phase present in the interdendritic and intergranular regions of the as-cast alloy (Fig. 5.7(a) shown by red arrows) partially dissolves into globularised particles in heat-treated alloys Fig. 5.7(b). In strontium modified and heat-treated alloys, Fig. 5.7(b), small voids are observed (shown by black arrows) in the microstructure which can easily be mistaken for spheroidized Mg_2Si particles. However, with careful observation, Mg_2Si phases can be distinguished from voids due to its unique colour (dark blue to brown) and displayed structure (characteristic script-like morphology). The needle β -phases are seen in Fig. 5.6 and Figure 5.7 to have partially transformed upon heat-treatment into a plate-like phases.

5.4 Mechanical Properties

The mechanical properties of aluminium castings are reported to be affected appreciably by the type and morphology of the silicon in the eutectic as well as those of intermetallic compounds formed. In this study, effects of iron, strontium, manganese additions and heat-treatment on hardness, ductility, tensile strength and fatigue was carried out and results analyzed as shown in the previous chapter under results.

5.4.1 Hardness Test

Results of hardness tests with varying iron content are shown in Figure 4.14. In Figure 4.15, the hardness test with varied chemical composition and heat-treatment are superimposed so as to simplify the discussion.

As revealed in Figure 4.15 indicated by line 2, it is established that increase in iron content leads to an increase in alloy hardness. Values of hardness increased from 85 VHN with iron content of 0.84wt.% to 97 VHN as iron content is raised to 1.8wt.% Fe. As discussed earlier under microstructure, the number and size of iron intermetallic phases especially the brittle β - Al_5FeSi increases with iron addition and in turn increases the hardness. On heat-treated alloys (H0 and H1), the effects of iron on hardness is slightly suppressed as shown in line 3 where the hardness is reduced from 88 VHN to 86 VHN. Reduction of hardness upon heat-treatment is owed to microstructural changes such as spheroidization of the eutectic silicon, dissolution and fragmentation of the β - Al_5FeSi platelets. Since all other parameters that could affect the hardness were kept constant, it can be concluded that increase of this hardness is related to presence of such iron-intermetallic phases.

The maximum hardness at each iron level is found in manganese added alloy as indicated by line 1 in Fig, 4.15. For instance, at iron level of 1.2wt.% Fe, the hardness number increased from 88 HVN to 89 HVN upon addition of 0.6wt.% Mn. The same increase of hardness is observed in alloy P5 with iron content of 1.8wt.% upon Mn addition. As reported by Flores et al³⁷ who studied the kinetics of nucleation and growth of the $\text{Al}_{15}(\text{Fe},\text{Mn})_3\text{Si}_2$ phase in aluminium scrap, iron and manganese at levels exceeding 0.6wt.%Fe, 0.5wt.%/Mn and 8wt.%Si led to the formation of very hard inclusions. These inclusions which were identified as α - $\text{Al}_{15}(\text{Fe},\text{Mn})_3\text{Si}_2$ with a Chinese script in our study is linked to the increase of hardness with manganese addition. From the findings of our results, it can be concluded that addition of manganese to Al-Si alloys at certain levels of Fe, Mn

and Si (for our study 0.8wt.%, 0.6wt.% and 8wt.% respectively) increases the alloy's hardness. However, for heat-treated and strontium modified alloys, the hardness is slightly reduced even with addition of manganese. This reversal of manganese effects on hardness could be linked to softening and spheroidization of silicon particles and further fragmentation of β -phases by strontium and heat-treatment.

Strontium addition as shown in line 5 is found to reduce the hardness number. Apart from coarsening of silicon particles and fragmentation of β -phases as discussed earlier, strontium is found to increase porosity and this could also have reduced the hardness.

5.4.2 Tensile Properties

Figure 4.16 through Fig. 4.23 shows the variation in tensile properties (tensile strength and ductility) of the un-modified, modified, Mn added, heat-treated and non-heat-treated alloys as a function of iron content.

As seen in Fig. 4.16, the average tensile strength for iron contents of 0.84, 1.2, 1.5 and 1.8wt.% Fe were 207, 195, 185 and 168 MPa, respectively. On the other hand, the average ductility shown in Fig. 4.21 for the same iron content were 2.5, 2.2, 1.9 and 1.5% respectively as percentage elongation and 3.6, 3.3, 2.9 and 2.2% respectively as percentage area reduction. From these results, it can be seen that the tensile strength and ductility decreases rapidly with iron addition. Generally, the ductility of material increases as strength decreased and vice versa but this does not apply to the present situation.

As discussed earlier, the iron addition to Al-Si alloys tends to increase the number and size of intermetallic phases as shown in Figure 4.2, Figure 4.12 and Figure 4.13. Such intermetallics mainly the β -phase forms very weak bond with Al-matrix thus the poor bonding strength between the two phases would cause decohesion and brittle rupture to occur acting as a stress concentration point.

These intermetallic compounds mainly the needle iron-rich β -phase which is less bounded to the Al-matrix, in addition to the coarsened eutectic silicon are the main cause of tensile strength and ductility reduction especially with increased iron content.

Although the microstructures did not show signs of increased pores with increased iron content, raising iron content in aluminium alloys is reported by Wang et al⁶³ to increase porosities which results in decrease of tensile ductility and tensile strength. Presence of porosity tends to reduce effective load bearing area and thus earlier failure in the materials. Porosity in a stressed material results in a strain concentration and thus micro cracking around the pores.

In Figure 4.17 and Figure 4.22, addition of manganese is seen to improve the tensile strength and ductility. With addition of 0.6wt.% Mn to an alloy of 1.2wt.% Fe, tensile strength improved from 195 to 200MN/m² while ductility is raised to 2.3 from 2.2% on elongation and 3.5 from 3.3% on area reduction. This improved tensile properties were also observed on specimen P5 with iron content of 1.8wt.% upon addition of 0.9wt.% of manganese. Manganese addition tend to reverse detrimental effects of iron by favouring the formation of $Al_{15}(Fe,Mn)_3Si_2$ in the shape of Chinese script which minimizes the size and amount of the embrittling needle shaped β - Al_5FeSi thus improved tensile properties.

Strontium modification as shown in Figure 4.18 and Figure 4.22 is seen to improve tensile properties. As revealed in Fig. 4.22, addition of Sr improves the ductility more than does Mn. The ductility with iron content of 1.8wt.% was improved to 1.6% on elongation and to 2.4% on area reduction upon addition of 0.9wt.% Mn and further to 1.8% on elongation and to 2.6% area reduction after Sr modification. In other words, the ductility depends more on the morphology and size of the silicon and less on the morphology of the iron-rich phase especially with high silicon aluminium alloys. These can be observed in the microstructures

of modified and heat-treated samples where the silicon is completely refined than the β -phases. As reported earlier, Sr restrains the sites available for nucleation of iron intermetallic phases, thus reduced number of β -phases improving tensile properties. With a combination of Sr and Mn as observed in Fig. 4.19 and Fig. 4.22, tensile properties are further improved because β -phase are dealt with by both Mn and Sr greatly reducing both the sizes and amount as well as refining silicon particles by Sr as discussed earlier.

The results of tensile properties on heat-treated samples shows some improvement as seen in Fig. 4.20 and Fig. 4.23 for tensile strength and ductility respectively compared to un-heat-treated samples. This can be explained in terms of the mechanism of transformation of the Si particle morphology from acicular or fibrous form to globular form through spheroidization and coarsening processes occurring during solution treatment, as discussed earlier.

With a combination of modification and heat-treatment, tensile properties are seen to have been improved further. This is due to dissolution and fragmentation of the few remaining β -phase platelets into smaller segments and spheroidization of the irregular silicon particles.

5.4.3 Fatigue Results Analysis

Figure 4.24 through Figure 4.35 shows a range of fatigue crack growth rates $\frac{da}{dN}$ established over the three regions as a function of stress intensity factor range ΔK , obtained for various iron levels with or without addition of manganese, strontium and/or heat-treatment. The region II rates, according to Paris Erdogan, are of great practical interest since the behavior at this region is often characterized by a linear relationship between $\log \frac{da}{dN}$ and $\log \Delta K$. From the Paris relationship given by $\frac{da}{dN} = C(\Delta K)^m$, fatigue crack growth rate exponent (m) and crack growth rate coefficients (C) were calculated as presented in Figure 5.8. Since the slope of FCG curve represents the steady fatigue crack growth rate, then fatigue growth rate given by values of ' m ' were found to reduce from 3.511 to 3.233 as iron content increases from 0.84wt.% to 1.8wt.% Fe.

For strontium modified, manganese addition and heat-treated alloys, the fatigue crack growth rate given by ' m ' was found to increase to values of between 3.582 and 4.365. Examining Fig. 4.36 and Table 4.6, it is seen that increasing iron content from 0.84wt.% to 1.8wt.% decreases fatigue life from about 1.745×10^6 cycles to about 1.404×10^6 cycles at an applied constant load of 650 pounds (2894N), while strontium modification, manganese addition and heat-treatment slightly improves the fatigue life.

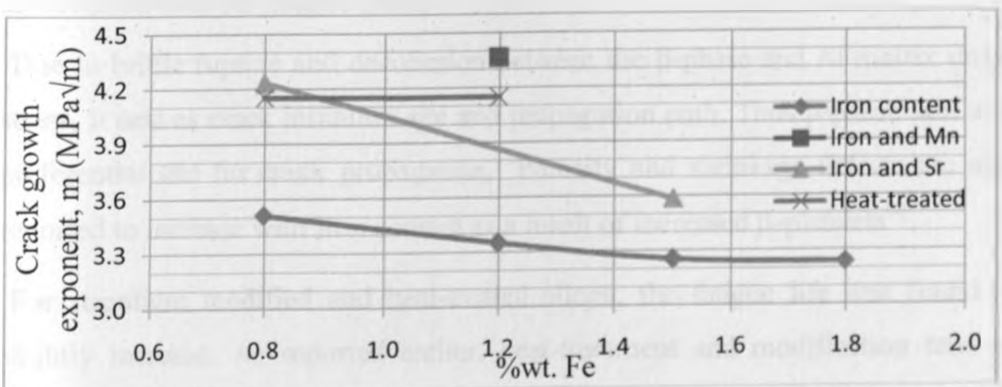


Figure 5.8: Graph of fatigue crack growth exponent, m (MPa \sqrt{m})

As reported by Wang et al⁶⁵, three major microstructural parameters namely: (a) DAS, (b) porosity/shrinkage defects and (c) fraction, size and crystallographic orientation of intermetallic particles has significant effects on the fatigue properties of a wide range of aluminium alloys. The above mentioned parameters are also a function of iron content. As found in the previous section, volume fraction, size and amount of intermetallic increases with iron content. Thus decrease in fatigue life (cycle) with increased iron content as shown in Fig. 4.36 can be associated to increase in volume fraction and grain size number with iron content reported in Table 4.3 and Table 4.4.

An optical micrograph of an etched surface showing the interdendritic fatigue crack growth crack path for FCG test conducted on heat-treated material is shown in Fig. 5.9. The micrograph shows the main fatigue crack (lower red arrows) and a secondary fatigue crack (upper blue arrows) that propagated along or near grain boundaries of silicon particle. The micrograph shows the fatigue crack tip region (marked by arrows) and definitively shows that the fatigue propagated either along the grain boundaries, porosity site, intermetallic phase and/or Si particle.

As seen in Figure 5.9, intermetallic particle is indicated by letter 'B' and 'D' while 'C' as porosity. Initial crack path as shown by letter 'A' was deflected to the intermetallic particle 'B'. Therefore, it is plausible that apart from initiating crack, iron is influencing porosity through the formation of β -phases which acts as initiation sites for fatigue crack.

Due to brittle rupture and decohesion between the β -phase and Al-matrix under stress, it acts as crack initiation site and propagation path. Thus β -phase acts as a preferential site for crack propagation. Porosity and shrinkage defects are also reported to increase with iron content as a result of increased β -platelets⁶⁴.

For strontium modified and heat-treated alloys, the fatigue life was found to slightly increase. As reported earlier, heat-treatment and modification tend to dissolve, fragment and spheroidize iron-rich intermetallics and silicon particles thus reducing fatigue crack initiation sites.

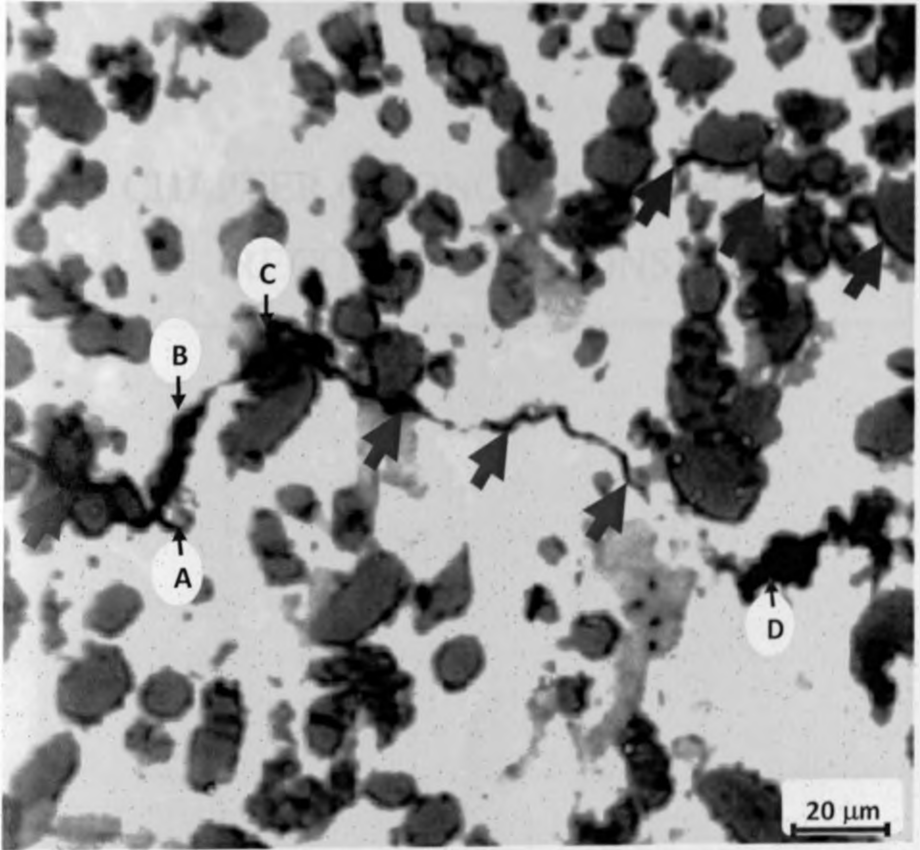


Figure 5.9: Micrograph of an etched surface showing the intergranular fatigue crack growth crack path for FCG test conducted on heat-treated material.

CHAPTER 6: CONCLUSIONS AND RECOMMENDATIONS

CONCLUSIONS AND RECOMENDATIONS

6.1 Conclusions

A number of experiments were carried out to ascertain the effects of iron on solidification, microstructure and mechanical properties of aluminium silicon alloys and the following conclusions can be drawn from the results of the investigation:-

- During solidification of aluminium silicon alloys, presence of iron, manganese and strontium tend to concentrate in ways to influence the solidification behavior and also tend to trigger the nucleation and growth of second phases. Solidification temperature of α -Al dendrite was found to increase from 596°C to 606°C with addition of 0.6wt.% Mn.
- The results show that even slight changes in the concentration of these elements can cause a variation in the reaction temperature and resultant microstructure.
- The results also show that strontium modification tends to raise the precipitation temperature of intermetallics from 577°C to 587°C but it lowers the eutectic temperature of aluminium silicon from 547°C to 540°C.
- Observation of the microstructure revealed a number of intermetallic phases formed as iron content increases. Iron addition in combination with other elements results in the formations of needle β -phases (Al_5FeSi), α -phase ($\text{Al}_{15}(\text{Fe,Mn})_3\text{Si}_2$) and α - $\text{Al}_8\text{Fe}_2\text{Si}$ phase whose grain size and volume fraction increases with iron concentration.
- Both grain size and volume fraction of intermetallic phases were found to increase from 5.35 μm to 7.25 μm and from 4.2% to 8.6% respectively as the iron content increases from 0.84wt.% to 1.8wt.%.
- Strontium modification at levels of 0.02wt.% tends to reduce the size of intermetallic phases and also refines eutectic silicon.

- Addition of 0.02wt.% Sr and 0.6wt.% Mn combined is found to be more effective in modifying the needle-like β -phase to shorter, more separated ones and changing the morphology to the Chinese script type and more refined silicon particles than addition of Mn or Sr alone.
- A T6 heat treatment cycle tends to fragment the intermetallic phases and spheroidize the silicon phases.
- A combination of strontium modification at a level of 0.02% and heat-treatment at 500°C results in a more coarsened and rounded silicon with further reduction of intermetallic phases.
- Hardness of Al-Si alloy increases as iron content is increased to 1.8wt.% with further increase with addition of 0.9wt.% manganese due to the formation of a hard α -Al₁₅(Fe,Mn)₃Si₂ script.
- However, strontium modification at levels 0.02wt.% and heat-treatment tend to reduce the effects of iron resulting to decrease in hardness.
- The present experimental result reveals that iron addition decreases fatigue, tensile strength and ductility of Al-Si alloys. This detrimental effect of iron on mechanical properties is due to the size and number of iron-containing intermetallics (particularly the brittle β -phase) that increases with iron content. Since these participate directly in the fracture mechanism, the more intermetallics there are, the lower the ductility and the less the number of cycles for the fatigue failure.
- Addition of 0.02wt.% strontium leads to slight improvement of ductility, tensile strength and fatigue due to fragmentation and dissolution of β -platelets.
- Strontium and manganese combined is more effective in reducing the size and number of β -platelets in addition to spheroidization of silicon resulting in improved ductility, tensile strength and fatigue.
- Heat-treatment in our study is also found to slightly reduce the intensity of the negative effects of iron with improved mechanical properties.

6.2 Recommendations

- It was not clear how iron influences the reaction temperatures during solidification and thus a proper design of our mold to accommodate a number of thermocouples would be useful in ascertaining the role of iron in influencing change in reaction temperatures.
- Observation of figure 4.3 shows that increasing manganese does not necessarily result in the alpha phase formation. As evident in figure 4.3(c), some iron constituents still appear as needles. This means that a Mn:Fe ratio of 1:2 given by Gowri et al¹³ is insufficient to prevent the β - plates forming, thus at these slow cooling rates, a ratio closer to 1:1 may be necessary but caution must be taken to avoid sludge formation. However, presence of magnesium seems to influence the formation of various intermetallic phases such as π -phase ($\text{Al}_8\text{FeMg}_3\text{Si}_2$) and further studies on effects of magnesium on aluminium alloys would be of useful.
- Generally, iron is found to have detrimental effects both on microstructure and in mechanical properties of Al-Si alloys and any process that can be employed to raise its permissible concentrations should unequivocally deal with possible reduction in mechanical properties especially fatigue, ductility and tensile strength. This is so because, although strontium and manganese is recommended in reducing detrimental effects of iron, they tend to cause porosities and hard intermetallics in form of sludge respectively at certain levels. Hence alloy development should focus on neutralizer strategies which seem to offer great potential in reducing harmful effects of all concentrations of iron despite their drawbacks.
- As stated earlier, aluminium has found wide application especially in automotive and aerospace industry due to its light weight hence improved fuel efficiency. This research needs to be carried out at high temperatures so as to come up with aluminium engine blocks and cylinder heads with high strength especially during combustion stage since they are normally subjected to temperatures of up to 440°C.

REFERENCES

1. E. Merzbacher, *Schottky effect, Structure and Properties*, (1972), London: Butterworths.
2. Z. Ma, M. Sauer, H. G. Meyer, and G. B. Fisher, "Effect of temperature and carrier rate on the Schottky effect in GaAs and InSb semiconductors," *Phys. Rev. B*, **31**, 1000 (1985).
3. J. Pappert, "Metal-semiconductor junctions in semiconducting alloys", (1985), *Cont. Metals*, **4**, 229-237.
4. J. H. Guillet and B. M. Choudhury, *The Dynamics of Fluids in Semiconducting Alloys*, (1979), Academic Press, London, Vol. 194.
5. J. R. Dwyer, *Transport in Semiconducting Alloys*, (1979), John Wiley, Oxford, Taylor & Francis, London.

Received 1985-10-15; revised 1986-01-15; accepted 1986-02-15.

Correspondence should be addressed to Dr. G. B. Fisher, School of Physics, University of Exeter, Exeter, Devon, EX4 4PL, England.

© 1986 Scripta Technica, Inc. This article is a U.S. Government work and, as such, is in the public domain in the United States of America.

ISSN 0013-788X/86/0013-0000\$01.00/0

Scripta Technica, Inc. is a not-for-profit corporation organized under the laws of the State of New York. Its purpose is to publish technical information in the field of applied science and technology.

Scripta Technica, Inc. is a member of the International Association of Scientific, Technical and Engineering Publishers (IASET).

Scripta Technica, Inc. is a member of the International Association of Technical Publishers (IATP).

REFERENCES

1. L. F. Mondolfo: *"Aluminum alloys; Structure and Properties"*, (1976), London, Butterworths.
2. Z. Ma, M. Samuel, H. Doty and S. Valtierra: *"Effect of Fe content and cooling rate on the impact toughness of cast 319 and 356 aluminum alloys"*, (2003), AFS Trans, 255-265.
3. J. Taylor: *"Metal-related castability effects in aluminum foundry alloys"*, (1995), Cast Metals, **8**, 225-252.
4. J. E. Gruzleski and B. M. Closset: *"The Treatment of Liquid Aluminum-Silicon Alloys"*, (1990), American Foundrymen Society Inc, 59-65.
5. J. R. Brown: *"Foseco non-ferrous Foundry man's Handbook"*, 11th edition, (1999), Oxford, Butterworth-Heinemann.
6. G. A. Pagonis: *"The Light Metals Handbook"*. (1975), New York, Macmillan.
7. B. Closset and S. Timminco: *"Effect of alloying elements and strontium modification on mechanical properties of A357 alloys"*, (2005), Shell Cast Foundries Inc, 137-154.
8. T. Mbuya, B. Odera and S. Ng'ang'a: *"Influence of iron on castability and properties of aluminum silicon alloys: Literature review"*, (2003), Cast Metal Research, **16**, 451-465.
9. M. Samuel, A. Pennors, C. Villeneuve, F. Samuel, H. Doty and S. Valtierra: *"Effect of cooling rate and Sr-modification on porosity and Fe-intermetallics formation in Al-6.5%Si-3.5%Cu-Fe alloys"*, (2000), Cast Metals Research, **13**, 231-253.
10. G. Shabestari, M. Mahmudi, M. Emamy and J. Campbell: *"Effect of Mn and Sr on intermetallics in Fe-rich eutectic Al-Si alloy"*, (2002), Cast Metals Research, **15**, 17-24
11. M. Moustafa, F. Samuel and H. Doty: *"Effect of solution heat treatment and additives on the microstructure of Al-Si (A413.1) automotive alloy"*, (2003), Journal of Materials Science, **38**, 4507-4522.

12. X. Cao and J. Campbell: "*The nucleation of Fe-Rich phases on oxide films in Al-11.5Si-0.4Mg cast alloys*", (2003), Metallurgical and Materials Transactions, **34A**, 1409-1420.
13. S. Gowri and F. Samuel: "*Effect of alloying elements on the solidification characteristics and microstructure of Al-Si-Fe 380 alloy*", (1994), Metallurgical and Materials Trans, **25A**, 437-448
14. G. Sigworth, D. Apelian and S. Shivkumar: "*The influence of molten metal processing on mechanical properties of cast Al-Si-Mg alloys*", (1989), AFS Transactions, **97**, 811-824.
15. G. Shabestari and J. Gruzleski: "*Gravity segregation of complex intermetallic compounds in liquid aluminum-silicon alloys*", (1995), Metallurgical and Materials Science, **26A**, 999-1006.
16. J. Taylor, G. Schaffer and D. StJohn: "*The role of iron in the formation of porosity in Al-Si-Cu based casting alloys*", (1999), Metallurgical and Materials Science, **30A**, 1643-1650.
17. G. Gustafsson, T. Thorvaldsson and L. Dunlop: "*The influence of Fe and Cr on the microstructure of cast Al-Si-Mg alloys*", (1986), Metallurgical Transactions, **17A**, 45-52.
18. A. Couture: "*Iron in aluminum casting alloy – A literature survey*", (2003), AFS International Journal of Cast Metals, **6**, 9-17.
19. P. N. Crepeau: "*Effect of iron in Al-Si casting alloys: A critical review*", (1995), AFS Transactions, **103**, 361-366.
20. M. Qian, J. Taylor, J. Yao, M. Couper and D. StJohn: "*A practical method for identifying intermetallic phase particles in aluminum alloys by electron probe microanalysis*", (2001), Journal of Light Metals, **1**, 187-193.
21. S. Murali, K. Raman and K. Murthy: "*The formation of β -FeSiAl₃ and Be-Fe phases in Al-7Si-0.3Mg alloy containing Be*", (1995), Material Science and Engineering, **190**, 165-172.
22. L. Wang, D. Apelian and M. Makhlof: "*Iron-bearing compounds in Al-Si diecasting alloys: Morphology and conditions under which they form*", (2005), AFS Transactions, 231-238.

23. S. Murali, S. Raman and K. Murthy: "*Morphology studies on β -FeSiAl₃ phase in Al-7Si-0.3Mg alloy with trace additions of Be, Mn, Cr and Co*", (1994), *Materials Characterization*, **33**, 99-112.
24. C. Triveno, R. Caram, C. Bolfarini, W. Botta and C. Kiminami: "*Intermetallic compounds in the Al-Si-Cu system*", (2003), *Acta*, **12**, 77-81.
25. C. Niels, C. Kijpers, J. Vermolen, K. Vuik and S. Zwaag: "*A model of the β -FeSiAl₃ to α -Al(FeMn)Si transformation in Al-Mg-Si alloys*", (2003), *Materials Transactions*, **44**, 1448-1456.
26. H. Jeong and E. Yoon: "*Elimination of Fe element in A380 aluminum alloy scrap by electromagnetic force*", (2000), *Materials Science*, **19**, 253-255.
27. S. Piyada, K. Usanee, D. Ittipon and T. Umeda: "*Influence of copper and iron on solidification characteristics of 356 and 380-type aluminum alloy*", (2003), *Materials Trans.*, **44**, 845-852.
28. J. Barresi, M. Kerr, H. Wang and J. Couper: "*Effect of magnesium, iron and cooling rate on mechanical properties of Al-7Si-Mg foundry alloy*", (2000), *AFS Transactions*, 563-570.
29. C. Tseng, S. Lee, W. Ten-Fu and J. Lin: "*Effects of Fe content on microstructure and mechanical properties of A206 alloy*", (2000), *Materials Transactions*, **41**, 708-713.
30. K. Wen, W. Hu and G. Gottstein: "*Intermetallic compounds in thixoformed aluminum alloy A356*", (2003), *Materials Science and Technology*, **19**, 762-768.
31. P. Ashtari, H. Tezuka and T. Sato: "*Influence of Sr and Mn additions on intermetallic compound morphologies in Al-Si-Cu-Fe cast alloys*", (2003), *Materials Transactions*, **44**, 2611-2616.
32. K. Kashyap, S. Murali, S. Raman and K. Murthy: "*Casting and heat treatment variables of Al-7Si-Mg alloy*", (1993), *Materials Science and Technology*, **9**, 189-203.
33. Q. Wang, H. Caceres and J. Griffiths: "*Cracking of Fe-rich intermetallics and eutectic Si particles in an Al-7Si-0.7Mg casting alloy*", (1999), *AFS Transactions*, **106**, 131-136.

34. N. Kuijpers, W. Kool, P. Koenis, K. Nilsen and I. Todd: "*Assessment of different techniques for quantification of α -Al(FeMn)Si and α -AlFeSi intermetallics in AA 6xxx alloys*", (2003), *Materials Character.* **49**, 409-420.
35. N. Anantha, G. Shabestari and J. Gruzleski: "*Microstructure control of iron intermetallics in Al-Si casting alloys*", (1995), *International Journal of Cast Metals*, **86**, 457-464.
36. J. Taylor, D. StJohn, H. Zheng, G. Edwards, J. Barresi and M. Couper: "*Solution treatment effects in Al-Si-Mg alloys: Intermetallic phases*". (2000), *Aluminum Transactions*, **4**, 95-110
37. A. Flores, M. Sukiennik, H. Castillejos and J. Escobedo: "*A kinetic study on the nucleation and growth of the $Al_8FeMnSi_2$ intermetallic compound for aluminum scrap purification*", (1998), *Intermetallics*, **6**, 217-227.
38. M. Massazza, G. Riontino, C. Riontino, A. Triggiani and E. Cara: "*Effect of Be on phase transformations in an A357 – AlSiMg alloy*", (2002), *Materials Science Forum*, **396-402**, 965-970.
39. X. Cao and J. Campbell: "*Precipitation of primary intermetallic compounds in liquid Al-11.5Si-0.4Mg alloy*", (2000), *International Journal of Metals Res.*, **13**, 175-184.
40. X. Cao and J. Campbell: "*Effect of Precipitation of primary intermetallic compounds on tensile properties of cast Al-11.5Si-0.4Mg alloy*", (2004), *AFS Transactions*, **108**, 391-400.
41. X. Cao and J. Campbell: "*Effect of Precipitation and sedimentation of primary α -Fe phase on liquid metal quality of cast Al-11.1Si-0.4Mg alloy*", (2004), *Cast Metals Research*, **17**, 1-11.
42. S. Murali, K. Raman and S. Murthy: "*Effect of magnesium, iron (impurity) and solidification rates on the fracture toughness of Al-7Si-0.3Mg alloy*", (1992), *Materials Science and Engineering*, **151**, 1-10
43. Q. Wang, P. Jones and M. Osborne: "*Effect of iron on the microstructure and mechanical properties of an Al-7%Si-0.4%Mg casting alloy*", (2003), *SAE Technical Paper*, **1**, 823.

44. P. Wang, S. Lee, J. Lin and M. Jahn: "*Effects of solution temperature on mechanical properties of 319 aluminum casting alloys containing trace of Be*", (2000), *Material Science*, **15**, 2027-2035
45. T. Morinaga, T. Tsuneo and T. Saga: "*Influence of iron on die-casting alloys of the Al-Si-Cu system*", (1965), *Materials Trans.*, **6**, 72-77.
46. Q. Wang and J. Griffith: "*Microstructural effects on the fatigue properties of aluminum castings*", (2001), *Materials Solutions Conference '98 on Aluminum Casting Technology at Rosemont*, 217-223.
47. S. Murali, K. Raman and S. Murthy: "*Al-7Si-0.3Mg cast alloy: Formation and crystal structure of β -FeSiAl5 and (Be-Fe)-BeSiFe₂Al₃ phases*", (1996), *Aluminium Alloys*, **217**, 207-212.
48. M. Ravi, U. Pillai, C. Pal, A. Damodaran and E. Dwarakadasa: "*The effect of mischmetal addition on the structure and mechanical properties of a cast Al-7Si-0.3Mg alloy containing excess iron up to 0.6%*", (2002), *Metallurgical and Materials Trans.*, **33A**, 391-400.
49. B. Kulunk, G. Shabestari, J. Gruzleski and D. Zuliani: "*Beneficial effects of strontium on 380 alloy*", (2001), *AFS Transactions*, **96**, 1189-1193.
50. P. Wang, Y. Liauh, S. Lee and J. Lin: "*Effects of Be addition on microstructures and mechanical properties of B319.0 alloys*", (1998), *Materials Chemistry and Physics*, **53**, 195-202
51. H. Kim, T. Kobayashi and T. Ito: "*Effects of Fe and Ca on usual and impact fatigue characteristics of AC2B – T6 aluminum casting alloy*", (1996), *Materials Science Forum*, **222**, 1395-1400.
52. C. Styles and P. Reed: "*Fatigue of an Al-Si gravity die casting alloy*", (2000), *Materials Science Forum*, **331-337**, 1457-1462.
53. A. Wickberg, G. Gustafsson and L. Larsson: "*Microstructural effects on the fatigue properties of a cast Al-7Si-Mg alloy*", (1985), *Society of Automotive Engineers, Inc.* 1.728-1.735.
54. Xu Zhenming, Li Tianxiao and Zhou Yaohe: "*Elimination of Fe in Al-Si cast alloy scrap by electromagnetic filtration*", (2003), *Materials Science*, **38**, 4557- 4565.

55. A. Samuel, W. Doty and S. Valtierra: *"Effect of superheat, cooling rate and impurities on the formation of iron intermetallics in Al-Si die casting alloys"*, (2001), AFS Trans, **109**, 679-696.
56. X. Cao and J. Campbell: *"Effect of melt superheating on convection free precipitation and sedimentation of primary α -Fe phase in liquid Al-11.5Si-0.4Mg alloy"*, (2003), International Journal Cast Metals Res., **15**, 595-608.
57. J. Petrik, S. Peter and V. Spet'uch: *"The application of Ni for improvement of Al-Si-Fe alloys"*, (2009), Materials Engineering, **16**, 29-33.
58. M. Moustafa, H. Samuel and W. Doty: *"Effect of solution heat treatment and additives on the hardness, tensile properties and fracture behavior of Al-Si (A413.1) automotive alloy"* (2003), Materials Science, **38**, 4523-4534
59. D. Apelin, S. Shivkumar and G. Sigworth: *"Fundamental aspects of heat treatment of cast Al-Si-Mg alloys"*, (1990), AFS Transactions, **97**, 727-742.
60. X. Cao and J. Campbell: *"Effect of Sr on primary α -Fe phase in liquid Al-11.5Si-0.4Mg cast alloy"*, (2004), Materials Science and Technology, **20**, 514-520.
61. H. Caceres, J. Davidson, R. Griffiths, Hogan and Q. Wang: *"Hypoeutectic Al-Si-Mg foundry alloys"*, (1995), Materials Forum, **19**, 27-43.
62. K. Gall, N. Yang, M. Horstemeyer, D. McDowell and J. Fan: *"The influence of modified intermetallics and Si particles on fatigue crack paths in a cast A356 Al alloy"*, (2000), Fatigue and Fracture of Materials Structures, **23**, 159-172.
63. J. Wang, S. He, B. Sun, K. Li, D. Shu and Y. Zhou: *"Effects of melt thermal treatment on Hypoeutectic Al-Si alloys"*, (2002), Materials Science and Engineering, **338**, 101-107.
64. L. Wang, D. Apelian and M. Makhlof: *"Fatigue properties of Al diecasting alloys"*, (1998), AFS Transactions, 155-162.
65. L. Wang, M. Makhlof and D. Apelian: *"Aluminum die casting alloys: alloy composition microstructure and properties - performance relationships"*, (1995), International Materials Review, **40**, 221-238.

APPENDICES

APPENDIX A

COOLING RATES ANALYSIS

Apart from alloy composition, cooling rate determines the shape, size and distribution of intermetallic compounds and therefore the solidification time for the cast samples inside the cast iron mold, figure 3.1, were recorded using a data logger.

Cooling rates are affected by thickness of a sample, size and material used to make a mold. Cooling is slower in thicker samples compared to thinner ones as heat from the metal has to be dissipated over a thicker sample section compared to thinner regions.

Cooling rate of a cast sample is normally regulated in order to determine the following:-

- The size and distribution of microstructural features as well as defects, e.g. porosity,
- The size and shape of grains,
- The size of secondary dendrite arm spacing (SDAS),
- The distribution of solute elements in the casting matrix.

In aluminum alloy, high cooling rate is normally preferred but the rate should not be too high since it is likely to increase the internal stresses owing to severe thermal gradients. This increases the likelihood for shape distortion.

During casting of samples used in this study, cooling rates of the following alloys were recorded as tabulated in Table A1.

Table A1: Results of time - temperature data for four alloys

Time (s)	Specimen P3 Temp (°C)	Specimen P4 Temp (°C)	Specimen P6 Temp (°C)	Specimen P9 Temp (°C)
0	710	715	712	708
10	698	700	685	695
20	684	688	670	685
30	670	675	655	670
40	650	662	634	660
50	633	650	620	644
60	605	640	600	630
70	592	626	598	610
80	588	618	597	592
90	587	612	596	591
100	586	606	595	590
120	585	604	594	589
140	584	602	593	588
160	583	597	592	587
180	580	595	590	586
200	577	59	587	583
220	573	586	585	580
240	572	584	580	575
260	567	580	575	570
280	562	575	570	566
300	557	570	565	562
310	554	566	563	560
320	550	564	560	557
330	548	561	558	554
340	547	558	555	550
350	548	555	550	548
360	546	550	548	546
370	544	549	546	545
380	542	548	544	544
390	540	549	542	543
400	539	548	541	543
410	538	547	540	542
420	536	546	541	542
430	535	545	540	542
440	534	544	540	542
450	533	543	539	541
470	533	542	537	540
490	532	540	536	538
510	533	539	534	537
530	532	538	532	534
550	532	537	530	532
570	531	535	527	528

Table A1 (continuation)

Time(s)	Specimen P3	Specimen P4	Specimen P6	Specimen P9
610	529°C	532°C	520°C	521°C
630	526	530	517	514
650	524	525	511	509
660	522	520	508	506
670	520	516	506	504
680	518	512	502	503
690	512	508	500	501
700	508	505	498	500
710	504	502	497	498
730	502	499	495	495
750	499	493	492	490
770	495	486	488	483
790	484	479	483	473
810	472	470	477	460
830	459	454	468	450
850	446	437	450	439
870	433	422	435	427
890	420	408	423	416
900	413	406	418	409



Figure A1: Locomotive engine (aluminium) pistons used in this research

APPENDIX B

HARDNESS TESTING

In Chapter 4 of this thesis, the hardness data is presented graphically using the average values of Vickers hardness number of each alloy for six tests carried on each sample. The complete data set of hardness test and standard deviation for all the alloys is presented in Table B1.

Table B1: Vickers Hardness Number (HVN) for all cast samples

<i>Samples</i>	<i>HVN</i>						<i>Average</i>	<i>Standard deviation</i>
	<i>1st</i>	<i>2nd</i>	<i>3rd</i>	<i>4th</i>	<i>5th</i>	<i>6th</i>		
P0	88.8	85.9	85.4	83.0	84.4	84.8	85	<i>1.946</i>
P1	89.6	86.7	85.8	90.1	87.5	88.1	88	<i>1.659</i>
P2	90.5	93.8	89.5	92.8	91.7	89.1	91	<i>1.863</i>
P3	97.5	93.9	98.0	94.9	99.3	96.3	97	<i>2.016</i>
P4	89.7	86.1	87.8	88.3	89.0	90.5	89	<i>1.546</i>
P5	102.1	98.6	99.0	96.2	101.3	100.6	100	<i>2.147</i>
P6	88.8	89.6	91.0	90.3	88.2	87.8	89	<i>1.240</i>
P7	94.6	95.8	93.8	90.5	92.6	91.8	93	<i>1.933</i>
P8	81.6	84.6	83.9	82.2	81.7	83.1	83	<i>1.228</i>
P9	85.4	84.1	82.1	82.7	85.6	82.2	84	<i>1.579</i>
H0	83.4	88.5	87.7	85.6	87.1	84.3	86	<i>2.005</i>
H1	94.0	95.1	92.3	95.6	91.8	96.9	94	<i>1.971</i>
H2	88.4	89.3	83.9	87.5	86.3	86.8	87	<i>1.878</i>
H3	90.1	87.4	86.9	89.6	88.9	89.7	89	<i>1.320</i>
H4	91.8	94.5	90.4	92.7	92.9	89.7	92	<i>1.757</i>
H5	82.1	80.9	81.9	83.0	79.7	81.6	82	<i>1.129</i>

Sample P5 with iron and manganese content of about 1.8wt.% and 0.9wt.% respectively has the highest standard deviation of 2.147. Such variation could be attributed to non-uniform distribution of intermetallics in the specimens.

APPENDIX C

TENSILE TESTING

Table C1 gives the results of the tensile tests done on all the specimens whereby five specimens were tested for each sample.

Table C1: Results of tensile tests

Sample	Specimen No	D_n (mm)	D_f (mm)	L_o (mm)	L_f (mm)	F_{max} (N)
P0	9	6.30	6.19	25.00	25.64	6350
	27	6.31	6.20	25.00	25.63	6300
	52	6.22	6.10	24.60	25.30	6600
	56	6.28	6.16	24.55	25.10	6550
	68	6.35	6.24	24.36	24.94	6400
P1	20	6.29	6.18	24.90	25.48	5750
	25	6.39	6.28	24.80	25.30	6100
	43	6.10	6.00	24.72	25.22	5900
	66	6.24	6.14	24.58	25.12	6000
	73	6.16	6.06	24.36	24.90	6050
P2	29	6.40	6.30	24.62	25.10	5850
	33	6.13	6.04	25.00	25.44	5400
	35	6.30	6.21	24.72	25.20	5800
	40	6.20	6.11	24.62	25.09	5750
	49	6.25	6.16	24.65	25.10	5670
P3	23	6.32	6.24	24.72	25.14	5450
	26	6.30	6.24	24.70	25.08	5000
	28	6.30	6.23	24.50	24.84	5150
	41	6.20	6.13	25.00	25.40	5250
	45	6.16	6.10	25.00	25.34	4900
P4	47	6.30	6.19	24.61	25.16	6300
	54	6.38	6.27	24.34	24.90	6000
	62	6.26	6.15	25.12	25.70	6500
	64	6.31	6.20	24.63	25.20	6200
	65	6.38	6.27	24.60	25.12	6450
P5	7	6.32	6.24	25.02	25.44	5380
	32	6.27	6.19	25.00	25.40	5150
	53	6.05	5.98	25.20	25.61	5300
	60	6.21	6.13	25.00	25.42	5480
	78	6.18	6.12	24.64	25.04	5200

Table C1: Results of tensile tests (continuation)

Sample	Specimen No	D_o (mm)	D_f (mm)	L_o (mm)	L_f (mm)	F_{max} (N)
P6	13	6.35	6.25	24.60	25.10	5900
	22	6.36	6.25	25.00	25.52	6050
	39	6.22	6.13	24.50	24.96	5700
	48	6.15	6.05	25.30	25.80	5950
	67	6.18	6.10	25.10	25.54	5500
P7	8	6.30	6.20	25.10	25.60	5800
	18	6.30	6.24	24.60	25.04	5500
	61	6.30	6.21	24.85	25.30	5650
	63	6.20	6.12	24.70	25.12	5000
	79	6.20	6.12	25.00	25.42	5480
P8	1	6.30	6.18	25.00	25.60	6400
	44	6.07	5.96	24.50	25.12	6380
	69	6.32	6.20	24.40	25.00	6430
	71	6.18	6.08	24.78	25.54	6460
	75	6.34	6.22	24.70	25.32	6450
P9	12	6.31	6.19	25.00	25.68	6550
	31	6.35	6.23	24.50	25.14	6500
	55	6.25	6.14	24.50	25.08	6250
	72	6.12	6.00	24.86	25.60	6750
	76	6.26	6.14	24.64	25.28	6520
H0	11	6.38	6.27	24.78	25.32	6240
	34	6.27	6.17	24.90	25.51	5850
	42	6.25	6.14	24.80	25.34	6180
	46	6.33	6.22	24.70	25.23	6100
	57	6.31	6.20	24.90	25.42	6480
H1	15	6.26	6.20	25.00	25.38	5050
	16	6.38	6.31	25.10	25.50	5200
	19	6.26	6.19	25.00	25.42	5350
	74	6.28	6.20	25.00	25.42	5450
	77	6.27	6.20	24.96	25.36	5240
H2	4	6.29	6.18	25.00	25.60	6050
	10	6.30	6.18	25.05	25.70	6500
	17	6.27	6.16	25.00	25.62	6300
	24	6.30	6.19	24.95	25.56	6100
	51	6.01	5.90	25.20	25.78	6400

Table C1: Results of tensile tests (continuation)

Sample	Specimen No	D _o (mm)	D _f (mm)	L _o (mm)	L _f (mm)	F _{max} (N)
H3	2	6.20	6.10	24.80	25.30	5750
	3	6.30	6.19	24.70	25.21	6050
	36	6.25	6.15	24.80	25.30	5950
	37	6.31	6.21	24.70	25.21	5800
	80	6.10	6.00	24.90	25.38	5900
H4	5	6.35	6.26	24.70	25.14	5600
	6	6.15	6.07	24.50	24.96	5550
	50	6.32	6.23	25.00	25.46	5660
	58	6.25	6.16	24.50	24.93	5700
	70	6.20	6.12	24.62	25.10	5460
H5	14	6.28	6.15	24.50	25.22	6850
	21	6.26	6.14	24.90	25.60	6600
	30	6.35	6.23	25.50	26.20	6560
	38	6.32	6.21	24.66	25.32	6390
	59	6.16	6.04	24.70	25.40	6660

Load-deformation data obtained from tensile tests do not give a direct indication of the material behavior because they depend on the specimen geometry.

However, using the relationships shown in equation C1 through equation C3, deformations and loads were converted to strains (percentage elongation and area reduction) and UTS stresses as tabulated in Table C2 through Table C4.

• Ductility Determination

Given the initial and final diameters and length measurements as specified in Table C1, percentage elongation and percentage area reduction were determined for all specimens using equation C1 and C2 respectively.

$$\epsilon_e (\%) = \frac{\delta}{L_o} \times 100 \text{ ----- [C1]}$$

$$\epsilon_a (\%) = \frac{\delta A}{A_o} \times 100 \text{ ----- [C2]}$$

- Ultimate Tensile Strength Determination

The ultimate tensile strength is the highest stress achieved by the specimen before the necking processes occurs. Once the ultimate tensile strength has occurred, necking will begin and the specimen will load until it fractures. The ultimate tensile strength was determined by taking the highest value of force for the aluminum test specimens.

Using equation C3 and values of maximum force and the corresponding diameters (D_o) in Table C1, the values of ultimate tensile strength were calculated and presented in Table C4.

$$\sigma_{UTS} = \frac{F}{A_o} \text{-----} [C3]$$

Where;

σ = normal stress applied on the specimen (N/m^2)

F = applied load (N), where the maximum load (F_{max}) was used

A_o = original cross sectional area (m^2)

δA = change in cross sectional area (m^2)

ϵ_e = normal strain in the longitudinal direction

ϵ_a = reduction in area

δ = change in the specimen's gage length given by ($L_f - L_o$)

L_o, D_o = original gage length and diameter

L_f, D_f = final gage length and diameter

Table C2: Percentage elongation for specimens

<i>Samples</i>	<i>Percentage elongation (%)</i>						<i>Standard deviation</i>
	<i>1st</i>	<i>2nd</i>	<i>3rd</i>	<i>4th</i>	<i>5th</i>	<i>Average</i>	
P0	2.846	2.240	2.381	2.520	2.560	2.5	0.226
P1	2.329	2.217	2.016	2.197	2.023	2.2	0.135
P2	1.826	1.942	1.760	1.950	1.909	1.9	0.082
P3	1.699	1.538	1.388	1.600	1.360	1.5	0.143
P4	2.235	2.301	2.314	2.114	2.309	2.3	0.085
P5	1.680	1.627	1.623	1.680	1.600	1.6	0.036
P6	2.033	1.878	2.080	1.976	1.753	1.9	0.131
P7	1.700	1.680	1.811	1.992	1.789	1.8	0.124
P8	2.531	2.400	2.459	2.510	3.067	2.6	0.270
P9	2.612	2.367	2.597	2.720	2.977	2.7	0.221
H0	2.088	2.146	2.179	2.450	2.177	2.2	0.140
H1	1.594	1.680	1.520	1.603	1.680	1.6	0.067
H2	2.400	2.595	2.302	2.445	2.480	2.4	0.107
H3	2.016	2.065	1.928	2.020	2.060	2.0	0.055
H4	1.781	1.950	1.878	1.755	1.840	1.8	0.078
H5	2.811	2.834	2.676	2.745	2.939	2.8	0.099

Variation in standard deviation as observed in Table C2, Table C3 and Table C4 could be attributed to uneven distribution of intermetallic particles in the aluminum matrix.

Table C3: Percentage area-reduction for varying samples

Samples	Percentage area reduction (%)						Standard deviation
	1 st	2 nd	3 rd	4 th	5 th	Average	
P0	3.456	3.462	3.785	3.821	3.435	3.6	0.193
P1	3.467	3.220	3.413	3.179	3.252	3.3	0.126
P2	2.859	3.101	2.915	2.837	2.882	2.9	0.106
P3	2.516	1.896	2.21	2.245	1.939	2.2	0.252
P4	3.462	3.419	3.456	3.419	3.483	3.5	0.028
P5	2.536	1.932	2.301	2.56	2.516	2.4	0.265
P6	3.125	2.873	3.429	3.226	2.572	3.1	0.332
P7	2.564	2.564	2.837	3.149	1.896	2.6	0.463
P8	3.592	3.773	3.761	3.750	3.210	3.6	0.239
P9	3.744	3.489	3.797	3.767	3.883	3.7	0.148
H0	3.456	3.445	3.419	3.164	3.489	3.4	0.131
H1	1.908	2.182	2.532	2.220	2.224	2.2	0.221
H2	3.467	3.673	3.462	3.627	3.478	3.5	0.137
H3	3.174	3.144	3.252	3.20	3.462	3.2	0.127
H4	2.815	2.564	2.859	2.585	2.828	2.7	0.143
H5	3.797	3.858	3.451	3.744	4.097	3.8	0.232

Table C4: Ultimate Tensile Stress for varying samples

Samples	UTS (MNm ⁻²)						Standard deviation
	1 st	2 nd	3 rd	4 th	5 th	Average	
P0	203.7	201.5	217.2	211.5	202.1	207	6.878
P1	185.0	190.2	201.9	196.2	203.0	195	7.677
P2	181.8	183.0	186.1	190.5	184.8	185	3.371
P3	173.7	160.4	165.2	173.9	164.4	168	6.015
P4	202.1	187.7	211.2	198.3	201.8	200	8.471
P5	171.5	166.8	184.4	180.9	173.4	175	7.149
P6	186.3	190.4	187.6	200.3	183.4	190	6.490
P7	186.1	176.4	181.2	165.6	181.5	178	7.815
P8	205.3	220.5	205.0	215.4	204.3	210	7.398
P9	209.5	205.2	203.7	229.5	211.8	212	10.340
H0	195.2	189.5	201.4	193.8	207.2	197	6.933
H1	164.1	162.7	173.8	175.9	169.7	169	5.800
H2	194.7	208.5	204.0	195.7	225.6	206	12.527
H3	190.5	194.1	193.9	185.5	201.9	193	5.991
H4	176.8	186.8	180.4	185.8	180.9	182	4.129
H5	221.1	214.4	207.1	203.7	223.5	214	8.581

APPENDIX D

FATIGUE TESTING

Fatigue tests were carried out and the results were as shown in Table D1.

Table D1: Number of cycles versus crack length

Specimen P0		
Time (Min)	N Cycles	crack a mm
0	0	19.9
61	91622	20.2
120	180240	20.5
179	268858	20.8
236	354472	21.2
293	440086	21.6
348	522696	22.0
402	603804	22.4
456	684912	22.8
508	763016	23.5
559	839618	24.1
608	913216	24.6
656	985312	25.1
701	1052902	25.8
744	1117488	26.5
783	1176066	27.1
816	1225632	27.7
847	1272194	28.4
877	1317254	28.9
904	1357808	29.5
929	1395358	30.3
952	1429904	30.8
973	1461446	31.5
994	1492988	32.4
1016	1526032	33.6
1036	1556072	34.9
1054	1583108	36.4
1071	1608642	37.7
1087	1632674	39.4
1102	1655204	41.1
1115	1674730	43.0
1127	1692754	45.4
1138	1709276	47.5
1147	1722794	51.0

Specimen P1		
Time (Min)	N Cycles	crack a mm
0	0	20.2
59	88618	20.5
116	174232	20.9
176	264352	21.4
235	352970	21.8
293	440086	22.4
348	522696	23.0
401	602302	23.5
452	678904	24.2
498	747996	24.7
543	815586	25.3
585	878670	25.9
626	940252	26.7
665	998830	27.8
702	1054404	28.0
737	1106974	28.7
769	1155038	29.8
799	1200098	30.1
826	1240652	30.8
852	1279704	31.5
876	1315752	32.2
898	1348796	32.9
918	1378836	33.7
936	1405872	34.3
952	1429904	35.2
969	1455438	36.0
985	1479470	36.8
1000	1502000	37.8
1014	1523028	39.0
1026	1541052	40.2
1037	1557574	41.3
1048	1574096	43.1
1058	1589116	45.0
1067	1602634	47.9

Specimen P2		
Time (Min)	N Cycles	crack a mm
0	0	20.2
61	91622	20.8
105	157710	21.3
161	241822	21.8
219	328938	22.4
278	417556	23.1
333	500166	23.7
387	581274	24.5
436	654872	25.5
482	723964	25.8
526	790052	26.6
567	851634	27.2
607	911714	27.9
644	967288	28.7
680	1021360	29.5
713	1070926	30.3
743	1115986	31.0
768	1153536	31.8
791	1188082	32.7
812	1219624	33.4
833	1251166	34.3
853	1281206	35.2
871	1308242	36.3
889	1335278	37.8
905	1359310	38.2
920	1381840	39.3
934	1402868	40.5
948	1423896	41.8
960	1441920	42.9
971	1458442	44.0
981	1473462	45.1
990	1486980	47.7
997	1497494	50.9
1002	1505004	54.2

1155	1734810	54.6
1162	1745324	58.7

1075	1614650	50.7
1081	1623662	52.5
1086	1631172	55.2

Table D1: Number of cycles versus crack length (continuation)

Specimen P3		
Time (Min)	N Cycles	crack a mm
0	0	20.3
60	90120	21.1
100	150200	21.4
150	225300	21.9
205	307910	22.6
260	390520	23.2
314	471628	23.9
363	545226	24.6
409	614318	25.3
455	683410	26.0
496	744992	26.7
537	806574	27.4
576	865152	28.2
615	923730	29.1
651	977802	30.0
682	1024364	30.8
711	1067922	31.6
733	1100966	32.3
752	1129504	33.1
771	1158042	33.9
788	1183576	34.8
804	1207608	35.5
820	1231640	36.8
834	1252668	37.3
847	1272194	38.0
858	1288716	38.7
870	1306740	39.7
881	1323262	40.5
892	1339784	41.7
902	1354804	42.6
912	1369824	44.3
921	1383342	46.0
928	1393856	48.7
935	1404370	53.2

Specimen P4		
Time (Min)	N Cycles	crack a mm
0	0	20.1
59	88618	20.3
115	172730	20.6
180	270360	21.1
244	366488	21.5
303	455106	22.0
359	539218	22.8
414	621828	22.9
466	699932	23.5
517	776534	24.0
565	848630	24.6
611	917722	25.2
654	982308	25.8
694	1042388	26.3
732	1099464	26.8
768	1153536	27.6
802	1204604	28.2
834	1252668	28.8
864	1297728	29.5
891	1338282	30.1
917	1377334	30.8
941	1413382	31.9
962	1444924	32.2
982	1474964	33.1
1000	1502000	34.1
1018	1529036	35.4
1034	1553068	36.7
1050	1577100	38.1
1064	1598128	39.5
1077	1617654	41.0
1090	1637180	42.9
1111	1668722	46.8
1120	1682240	49.0
1129	1695758	52.4
1135	1704770	55.2
1140	1712280	57.8

Specimen P6		
Time (Min)	N Cycles	crack a mm
0	0	20.2
58	87116	20.7
110	165220	21.2
166	249332	21.7
225	337950	22.3
285	428070	22.9
343	515186	23.5
400	600800	24.3
453	680406	24.9
503	755506	25.6
550	826100	26.4
593	890686	27.1
635	953770	27.8
675	1013850	28.6
711	1067922	29.4
745	1118990	30.2
776	1165552	31.0
803	1206106	31.8
828	1243656	32.2
850	1276700	33.5
871	1308242	34.6
891	1338282	35.6
910	1366820	36.5
927	1392354	37.6
943	1416386	38.4
957	1437414	39.1
968	1453936	40.2
980	1471960	41.0
992	1489984	41.9
1002	1505004	43.1
1011	1518522	45.2
1019	1530538	47.8
1025	1539550	50.6
1030	1547060	55.7

Table D1: Number of cycles versus crack length (continuation)

Specimen P9			Specimen H0			Specimen H5		
Time (Min)	N Cycles	crack a mm	Time (Min)	N Cycles	crack a mm	Time (Min)	N Cycles	crack a mm
0	0	19.9	0	0	20.1	0	0	19.8
62	93124	20.2	60	90120	20.4	61	91622	20.0
126	189252	20.4	117	175734	20.8	121	181742	20.3
192	288384	20.7	175	262850	21.1	178	267356	20.6
260	390520	21.1	238	357476	21.6	235	352970	20.8
324	486648	21.6	298	447596	22.0	291	437082	21.2
385	578270	22.0	355	533210	22.7	345	518190	21.6
443	665386	22.5	411	617322	23.2	398	597796	21.8
498	747996	22.9	463	695426	23.7	450	675900	22.3
551	827602	23.5	512	769024	24.3	500	751000	22.8
602	904204	24.0	559	839618	25.0	549	824598	23.2
650	976300	24.7	603	905706	25.5	596	895192	23.7
695	1043890	25.2	646	970292	26.2	641	962782	24.2
736	1105472	25.8	687	1031874	26.8	684	1027368	24.6
775	1164050	26.4	724	1087448	27.6	725	1088950	25.2
812	1219624	27.1	759	1140018	28.2	763	1146026	25.7
846	1270692	27.6	789	1185078	28.8	800	1201600	26.3
878	1318756	28.3	817	1227134	29.3	835	1254170	26.9
906	1360812	28.8	843	1266186	30.1	899	1350298	28.0
933	1401366	29.6	868	1303736	30.7	928	1393856	28.6
958	1438916	30.2	892	1339784	31.4	955	1434410	29.1
981	1473462	30.7	915	1374330	32.1	981	1473462	29.8
1002	1505004	31.2	937	1407374	32.8	1006	1511012	30.6
1022	1535044	32.3	958	1438916	33.7	1029	1545558	31.7
1040	1562080	33.4	978	1468956	34.6	1050	1577100	32.8
1057	1587614	34.3	995	1494490	35.6	1068	1604136	33.9
1072	1610144	35.5	1012	1520024	36.8	1085	1629670	34.8
1086	1631172	36.7	1028	1544056	38.2	1101	1653702	36.2
1099	1650698	38.0	1042	1565084	39.5	1130	1697260	39.1
1111	1668722	39.2	1056	1586112	41.2	1143	1716786	40.3
1122	1685244	40.4	1068	1604136	43.2	1155	1734810	42.0
1133	1701766	42.0	1080	1622160	45.3	1166	1751332	43.5
1143	1716786	43.7	1090	1637180	48.1	1176	1766352	45.4
1152	1730304	45.9	1099	1650698	51.4	1185	1779870	47.6
1160	1742320	47.8	1105	1659710	53.5	1193	1791886	49.5
1169	1755838	51.0	1110	1667220	57.3	1200	1802400	52.8
1177	1767854	53.2				1206	1811412	55.2
1184	1778368	56.5				1211	1818922	57.6
1190	1787380	58.9				1216	1826432	59.7

• **Determination of crack growth rate (da/dN) and stress intensity factor (ΔK)**

Results of fatigue tests for nine alloys with varying iron, Mn, strontium and heat-treatment performed using a fatigue crack-growth test rig at a speed of 1502 rpm are presented in Table D1. The present study devotes to an understanding of the fatigue behavior of Al-Si permanent mold cast alloys at varying iron, manganese and strontium levels with or without heat-treatment. It is known that any metal subjected to cyclic or fluctuating stress will fail at a stress level much lower than the yield stress, and failures occurring under cyclic stress termed fatigue failures.

Using measured values of crack length, a_n mm, and corresponding number of cycles, N presented in Table D1, the fatigue crack growth rate, $\frac{da}{dN}$, and stress intensity factor range, ΔK , were determined using equation D1 through equation D4 according to ASTM E-647 specifications.

$$\Delta K = \frac{\Delta P}{B\sqrt{W}} \left(\frac{2+\alpha}{(1-\alpha)^{3/2}} \right) \times f(\alpha) \text{ ----- [D1]}$$

Where;

$$f(\alpha) = 0.886 + 4.64\alpha - 13.32\alpha^2 + 14.72\alpha^3 - 5.6\alpha^4 \text{ ----- [D2]}$$

$$\text{and, } \alpha = \frac{\tilde{a}}{W} \text{ ----- [D3]}$$

$$\tilde{a} = \frac{a_{i+1} + a_i}{2} \text{ (mean crack length)}$$

$W = \text{effective width of specimen} = 80 \text{ mm}$

$B = \text{thickness of specimen} = 12 \text{ mm}$

$\Delta P = \text{load range applied} = 650 \text{ lbs} = 295 \text{ kgs} = 2894 \text{ Newton's}$

Crack growth rate was determined using equation D4 as follows:-

$$\frac{da}{dN} = \frac{a_{i+1} - a_i}{N_{j+1} - N_j} \text{ ----- [D4]}$$

Where;

$a_i = \text{crack length measured in millimeters (mm)}$

$N = \text{number of cycles}$

Values of crack growth rate, $\frac{da}{dN}$ (mm/cycles), and stress intensity factor range, ΔK (MPa√m), presented in Table D2 were determined by substituting the results tabulated in Table D1 into equation D1 through equation D4.

Table D2: Crack growth rate, $\frac{da}{dN}$, versus stress intensity factor range, ΔK

Specimen P0		Specimen P1		Specimen P2	
ΔK (MPa√m)	$\frac{da}{dN}$ (mm/cycle)	ΔK (MPa√m)	$\frac{da}{dN}$ (mm/cycle)	ΔK (MPa√m)	$\frac{da}{dN}$ (mm/cycle)
4.208	3.27E-06	4.251	3.39E-06	4.272	6.55E-06
4.251	3.39E-06	4.301	4.67E-06	4.352	7.57E-06
4.294	3.39E-06	4.367	5.55E-06	4.425	5.94E-06
4.345	4.67E-06	4.432	4.51E-06	4.506	6.89E-06
4.403	4.67E-06	4.506	6.89E-06	4.604	7.90E-06
4.462	4.84E-06	4.596	7.26E-06	4.702	7.26E-06
4.521	4.93E-06	4.679	6.28E-06	4.810	9.86E-06
4.581	4.93E-06	4.771	9.14E-06	4.952	1.36E-05
4.664	8.96E-06	4.865	7.24E-06	5.056	4.34E-06
4.764	7.83E-06	4.952	8.88E-06	5.146	1.21E-05
4.849	6.79E-06	5.048	9.51E-06	5.263	9.74E-06
4.928	6.94E-06	5.163	1.30E-05	5.374	1.17E-05
5.024	1.04E-05	5.323	1.08E-05	5.505	1.44E-05
5.138	1.08E-05	5.435	3.60E-06	5.649	1.48E-05
5.246	1.02E-05	5.514	1.33E-05	5.797	1.61E-05
5.348	1.21E-05	5.676	2.29E-05	5.940	1.55E-05
5.461	1.50E-05	5.806	6.66E-06	6.087	2.13E-05
5.567	1.11E-05	5.901	1.73E-05	6.260	2.61E-05
5.667	1.48E-05	6.038	1.79E-05	6.429	2.22E-05
5.797	2.13E-05	6.178	1.94E-05	6.605	2.85E-05
5.921	1.45E-05	6.323	2.12E-05	6.811	3.00E-05
6.038	2.22E-05	6.484	2.66E-05	7.052	4.07E-05
6.199	2.85E-05	6.639	2.22E-05	7.384	5.55E-05
6.419	3.63E-05	6.811	3.75E-05	7.643	1.66E-05
6.696	4.33E-05	7.015	3.13E-05	7.858	4.88E-05
7.027	3.55E-05	7.215	3.33E-05	8.208	5.71E-05
7.384	5.09E-05	7.451	4.44E-05	8.618	6.18E-05
7.802	4.07E-05	7.757	5.71E-05	9.045	6.10E-05
8.319	7.55E-05	8.114	6.66E-05	9.469	6.66E-05
8.935	9.73E-05	8.483	4.66E-05	9.928	7.32E-05
9.778	1.33E-04	8.989	7.20E-05	10.79	1.92E-04
10.82	1.27E-04	9.715	1.26E-04	12.43	3.04E-04
11.39	2.39E-04	10.82	2.15E-04	14.84	4.39E-04
13.06	4.00E-04	12.43	2.33E-04		
14.21	6.90E-04	13.06	3.50E-04		
		15.24	6.50E-04		

Table D2: Crack growth rate versus stress intensity factor range (continuation)

Specimen P3		Specimen P4		Specimen P6	
ΔK (MPa \sqrt{m})	$\frac{da}{dN}$ (mm/cycle)	ΔK (MPa \sqrt{m})	$\frac{da}{dN}$ (mm/cycle)	ΔK (MPa \sqrt{m})	$\frac{da}{dN}$ (mm/cycle)
4.301	8.88E-06	4.229	2.26E-06	4.265	5.74E-06
4.381	4.99E-06	4.265	3.57E-06	4.337	6.40E-06
4.440	6.66E-06	4.323	5.12E-06	4.410	5.94E-06
4.529	8.47E-06	4.388	4.16E-06	4.491	6.77E-06
4.626	7.26E-06	4.455	5.64E-06	4.581	6.66E-06
4.725	8.63E-06	4.551	9.51E-06	4.672	6.89E-06
4.834	9.51E-06	4.619	1.21E-06	4.779	9.34E-06
4.944	1.01E-05	4.672	7.68E-06	4.888	7.54E-06
5.056	1.01E-05	4.756	6.53E-06	4.992	9.32E-06
5.171	1.14E-05	4.841	8.32E-06	5.114	1.13E-05
5.289	1.14E-05	4.936	8.68E-06	5.238	1.08E-05
5.417	1.37E-05	5.032	9.29E-06	5.357	1.11E-05
5.567	1.54E-05	5.122	8.32E-06	5.487	1.33E-05
5.731	1.66E-05	5.205	8.76E-06	5.631	1.48E-05
5.892	1.72E-05	5.314	1.48E-05	5.778	1.57E-05
6.047	1.84E-05	5.435	1.17E-05	5.930	1.72E-05
6.199	2.12E-05	5.541	1.25E-05	6.087	1.97E-05
6.355	2.80E-05	5.658	1.55E-05	6.209	1.07E-05
6.527	2.80E-05	5.778	1.48E-05	6.387	3.93E-05
6.718	3.52E-05	5.901	1.79E-05	6.650	3.49E-05
6.906	2.91E-05	6.077	2.55E-05	6.894	3.33E-05
7.151	5.41E-05	6.219	9.51E-06	7.126	3.15E-05
7.384	2.38E-05	6.344	3.00E-05	7.384	4.31E-05
7.546	3.58E-05	6.549	3.70E-05	7.643	3.33E-05
7.742	4.24E-05	6.811	4.81E-05	7.858	3.33E-05
7.992	5.55E-05	7.126	5.41E-05	8.129	6.66E-05
8.271	4.84E-05	7.478	5.83E-05	8.433	4.44E-05
8.601	7.26E-05	7.873	6.66E-05	8.721	4.99E-05
8.971	5.99E-05	8.319	7.68E-05	9.101	7.99E-05
9.469	1.13E-04	8.899	9.73E-05	9.757	1.55E-04
10.19	1.26E-04	9.571	9.68E-05	10.84	2.16E-04
11.29	2.57E-04	10.04	1.53E-04	12.37	3.11E-04
13.56	4.28E-04	11.15	2.63E-04	15.37	6.79E-04
		12.38	3.52E-04		
		13.98	5.11E-04		
		15.01	7.46E-04		

Table D2: Crack growth rate versus stress intensity factor range (continuation)

Specimen P9		Specimen H0		Specimen H5	
ΔK (MPa \sqrt{m})	$\frac{da}{dN}$ (mm/cycle)	ΔK (MPa \sqrt{m})	$\frac{da}{dN}$ (mm/cycle)	ΔK (MPa \sqrt{m})	$\frac{da}{dN}$ (mm/cycle)
4.208	3.22E-06	4.236	3.33E-06	4.186	2.18E-06
4.244	2.08E-06	4.287	4.67E-06	4.222	3.33E-06
4.280	3.03E-06	4.337	3.44E-06	4.265	3.50E-06
4.330	3.92E-06	4.396	5.28E-06	4.301	2.34E-06
4.396	5.20E-06	4.462	4.44E-06	4.345	4.76E-06
4.462	4.37E-06	4.544	8.18E-06	4.403	4.93E-06
4.529	5.74E-06	4.634	5.94E-06	4.447	2.51E-06
4.596	4.84E-06	4.710	6.40E-06	4.499	6.40E-06
4.672	7.54E-06	4.795	8.15E-06	4.573	6.66E-06
4.756	6.53E-06	4.896	9.92E-06	4.641	5.43E-06
4.849	9.71E-06	4.992	7.57E-06	4.787	7.40E-06
4.944	7.40E-06	5.089	1.08E-05	4.857	6.19E-06
5.032	9.74E-06	5.196	9.74E-06	4.936	9.74E-06
5.130	1.02E-05	5.314	1.44E-05	5.024	8.76E-06
5.340	9.79E-06	5.435	1.14E-05	5.114	1.08E-05
5.444	1.46E-05	5.541	1.33E-05	5.297	8.07E-06
5.550	1.19E-05	5.640	1.19E-05	5.391	1.50E-05
5.667	1.97E-05	5.759	2.05E-05	5.505	1.38E-05
5.797	1.60E-05	5.892	1.60E-05	5.603	1.23E-05
5.901	1.45E-05	6.018	1.94E-05	5.713	1.79E-05
5.998	1.59E-05	6.158	2.03E-05	5.853	2.13E-05
6.158	2.66E-05	6.302	2.12E-05	6.038	3.18E-05
6.387	4.07E-05	6.473	2.85E-05	6.260	3.49E-05
6.605	3.52E-05	6.673	3.00E-05	6.495	4.07E-05
6.846	4.33E-05	6.894	3.92E-05	6.718	3.52E-05
7.139	5.71E-05	7.164	4.70E-05	6.990	5.83E-05
7.464	6.66E-05	7.505	5.83E-05	7.345	6.21E-05
7.814	6.66E-05	7.888	6.18E-05	7.742	7.13E-05
8.176	7.26E-05	8.351	8.08E-05	8.145	6.15E-05
8.635	9.68E-05	8.989	8.11E-03	8.618	9.43E-05
9.233	1.13E-04	9.799	1.17E-04	9.195	9.08E-05
9.741	1.63E-04	10.94	1.46E-04	9.885	1.26E-04
11.02	1.58E-04	12.72	2.44E-04	10.84	1.63E-04
12.50	2.37E-04	14.75	4.33E-04	11.97	1.58E-04
14.46	2.83E-04	17.67	8.06E-04	13.71	2.14E-04
15.06	4.14E-04			16.18	3.66E-04
16.68	7.66E-04			18.88	6.20E-04